1-1-2008

Solid-Liquid Mixing In Agitated Tanks : Experimental And CFD Analysis

Seyed. Hosseini
Ryerson University

SOLID-LIQUID MIXING IN AGITATED TANKS: EXPERIMENTAL AND CFD ANALYSIS

by

Seyed Hosseini

M. Sc. Chemical Engineering, Mazandran University, Iran, 1999

B. Sc. Polymer Engineering and Design, Petroleum University, Iran, 1996

A Thesis

presented to Ryerson University in Partial Fulfillment of the Requirements for the Degree of Master of Applied Science in the Program of Chemical Engineering

Toronto, Ontario, Canada, 2008

AUTHOR'S DECLARATION

I hereby declare that I am the sole author of this thesis.

I authorize Ryerson University to lend this thesis to other institutions or individuals for the purpose of scholarly research.

Seyed Hosseini

I further authorize Ryerson University to reproduce this thesis by photocopying or by other means, in total or parts, at the request of other institutions or individuals for the purpose of scholarly research.

Seyed Hosseini

BORROWER'S PAGE

Ryerson University requires the signatures of all persons using or photocopying this thesis. Please sign below, and give address and date.

SOLID-LIQUID MIXING IN AGITATED TANKS: EXPERIMENTAL AND CFD ANALYSIS

Abstract

Seyed Hosseini

MASc, Chemical Engineering, Ryerson University, Toronto, 2009

Solid-liquid mixing plays a significant role in crystallization, suspension polymerization, leaching, solid-catalyzed reaction and adsorption. In this study, a computational fluid dynamic (CFD) model was developed for solid-liquid mixing in a cylindrical tank equipped with a top-entering impeller. The multiple reference frame (MRF) technique, k-ε model and Eulerian-Eulerian approach were employed to simulate the impeller rotation, turbulent flow and multiphase flow, respectively.

The effects of impeller speed, solid concentration, particle size, solid density and impeller clearance on the mixing performance of four different impellers (A310, marine propeller, pitched blade turbine and A320) were investigated.

The CFD results were in good agreement with experimental data measured using electrical resistance tomography (ERT). In order to investigate the mixing quality in this study, the impeller speed required for maximum homogeneity, clouding height, and just-suspended impeller speed were investigated

Acknowledgements

I would like to express my sincere gratitude to my supervisors Dr.Farhad Ein-Mozaffari and Dr. Mehrab Mehrvar for their valuable guidance and consistent support in accomplishing this study. I would like to thank all friends, colleagues and the Engineering specialists in Chemical Engineering Department at Ryerson University for their assistance throughout my research. The financial support from NSERC is appreciated.

Table of Contents

List of Figures

List of Tables

1 Introduction

Since the dawn of brick houses and homemade bread, people have become increasingly familiar with solid-liquid mixing. Solid-liquid mixing is virtually involved in most fundamental technologies such as those utilized by ceramics, plastics, and food industries in our modern world. As a result, mixing tanks are of interest of many industries due to the simplicity of the application (Peker & Helvaci, 2008).

Mixing in agitated tanks which is widely being used in chemical, petrochemical and biochemical industries has been a favorite discussion topic for many researchers since 1950's. A wide variety of unit operations such as dispersion of solids, dissolution, leaching, crystallization, precipitation, adsorption, desorption, ion exchange, solid-catalyzed reaction, and suspension polymerization utilize solid-liquid mixing. Polymeric reactions in which a solid must be suspended in a medium such as polymer composites, production of high solid content polymers for coating, and space fuels are some examples of the crucial role played by mixing. In most cases, solid-liquid mixing is required to enhance the rate of mass transfer between solid and liquid phases. This requires a thorough understanding of parameters affecting the mixing process in order to eliminate obstacles in achieving the mixing goal. This can be extremely complicated because of the number of variables affecting the mixing process (Tatterson, 1991).

A vital part of the process is the fluid hydrodynamics of an agitated tank from which the movement of solid particles could be tracked. Understanding the interactions between the solid-liquid is crucial to be able to optimize the effects of parameters on mixing for a quality production. The process of solid-liquid mixing includes both the settling and floating of solids in un-gassed or gassed suspensions. In order to narrow down the field, this study is only dedicated to solid-liquid mixing of the settling solid in the absence of gas. Thus, the goal was to investigate parameters which have the most effects on solid-liquid wherever there is a need due to the lack of information in the open literature. In this regard, the chapters are formatted as follows:

- Chapter two provides literature review of the relevant works that have been done to date and how the objectives of this study were determined.

- Chapter three is founded on the experimental setup and methodology. It also presents the fundamentals of electrical resistance tomography in flow visualization.

- Chapter four reviews mathematical tools and approaches to modeling and simulation for this study. It also includes some information about the solution methodology and post-processing calculations.

- Chapter five presents the results of the study and elaborates upon them.

- Chapter six provides the most important outcomes of the study, reviews the conclusions and offers some recommendation for future study.

2 Literature review

2.1 Definition perfect mixing

Perfect mixing is defined, ideally, as a level of equilibrium at which all elements are distributed homogeneously with regards to concentration gradient throughout the media (Tatterson, 1991). Mixing is no longer believed to be a unit operation. In other words, mixing has become such an integral function of chemical plant processes in which a vast area of all forms of Newtonian and non-Newtonian liquids may be combined. Mixing consumes a considerable amount of time in the processes of a plant and there is no justification for losing profit because of over-mixing, time-wasting, under-mixing, or low quality mixing. In the present marketplace, processing material has become so important that there is always a compromise between the plant capacity and the product quality in which mixing is a vital criterion (Tatterson, 1991).

2.2 Applications of mixing

Mixing applications covers a vast area of liquid-liquid, gas-liquid, solid-liquid and solid-solid mixing. Paul et al. (2004) identify the following industries in which mixing plays a key role:

1. Fine chemicals, agrichemicals, and pharmaceuticals
2. Petrochemicals
3. Polymer processing
4. Paints and automotive finishes
5. Cosmetics and consumer products
6. Food
7. Drinking water and wastewater treatment
8. Pulp and paper
9. Mineral Processing

Operations involving dispersion of solids, dissolution, leaching, crystallization, precipitation, adsorption, desorption, ion exchange, solid-catalyzed reaction, and suspension polymerization are examples in which solid-liquid mixing is critical and affects the final product quality or conversion directly (Paul et al., 2004).

2.3 Design consideration

The degree of mixing is highly dependent upon the design parameters of both the vessel and the stirrers as well as the particle characteristics such as size distribution, density and the shape and liquid properties such as density, viscosity, surface tension and those which affect the rheological behavior, if applicable. One of the most popular methods of mixing is engaging a vessel with an agitator. It is essential to characterize parameters affecting the batch mixing vessel, in which mixing is usually conducted, as well as being an ideal reference for continuous processes.

2.4 Geometry consideration in mixing

The impact of the tank geometry is critical in the rate of mixing and power consumption. In fact, without proper tank geometry adequate mixing is not achievable in the prescribed amount of time. Optimal mixing requires the utilization of the variables listed below (Oldshue, 1983):

1. Vessel: The shape of the vessel such as rectangular, square, cylindrical and the bottom contour of the tank such as flat, dished or conical affect the hydrodynamics of the flow drastically and, as a consequence, the mixing yield (Paul et al., 2004). Generally, dish bottomed cylindrical vessels are preferred. A flat bottom, for instance, requires 10 to 20% more power than a dished bottom to achieve perfect mixing (Bittorf & Kresta, 2003). Tanks with a ratio of liquid height to tank diameter equal to one ($Z/T = 1$) are ideal for top entry with a single impeller. If the liquid height to tank diameter is more than one ($Z/T > 1$) the number of impellers must be greater than one to achieve perfect mixing. Nonstandard vessels with varying levels of liquid heights and different numbers of impellers can be used with buoyant solids to optimize mixing (Siddiqui, 1993).

2. Shaft: The shaft may be installed depending upon the process used from the top, side or the bottom of the tank. Entries from the top do not require sealing to prevent leakage, while entries from the side may avoid vortices and do not require baffles. Side entries perform well for solids with low settling velocities (Tatterson, 1994).
3. Impeller: There are a variety of impellers in industry and it is difficult to find an impeller which meets all the requirements of a process. Impellers are typically classified according to their mixing regime; laminar or turbulent. To generate laminar flow for poor momentum transport liquids impeller diameters must approach tank diameter. Helical ribbons, screws, and anchor impellers are examples of creeping flow producers. Baffles in laminar flow are not necessary since the flow is too slow to generate a vortex. Despite the previously mentioned impellers, turbulent regime flow makers are one-fourth to one-half of the tank diameter. They are either classified as axial flow makers (Figure 2.1) or radial flow makers (Figure 2.2) (Tatterson, 1991). Impeller geometry is an indication of the type of impeller required, although the impeller diameter ratio to the tank diameter has a significant effect on mixing parameters. For instance, some propellers draw less power than other impellers with the same diameter or the clearance of the impeller has drastic effect on the flow and usually suggested to be T/4 to T/3 from the bottom of the tank for axial impellers (Bittorf & Kresta, 2003; Oldshue 1983).

Figure 2.1 Axial flow impellers, left to right: Propeller (A100), pitched blade turbine, Pfaudler retreat curve, Ekato MIG, Ekato INTERMIG (Paul et al., 2004)

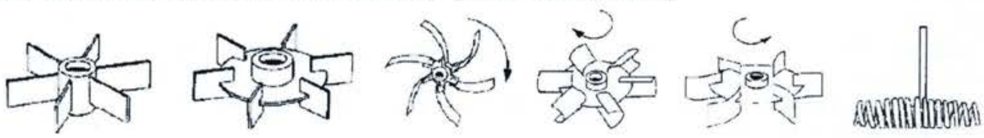

Figure 2.2 Radial flow impellers, left to right: Open flat blade, disk style Rushton, back swept open, Scaba SRGT, Chemineer CD 6 Smith, back swept with disk, spring impeller (Paul et al., 2004)

Hydrofoil impellers (Figure 2.3) such as Lightnin A310 or A315 are desired where axial flow is important with low shear rate. However, A310 is for low solidity and A315 is for high solidity mixtures.

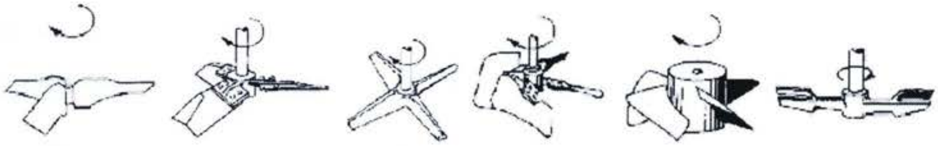

Figure 2.3 Hydrofoil impellers, left to right: Lightnin A310, Chemineer HE3, EMI Rotofoil, Lightnin A315, Prochem Maxflo, Ekato Interprop (Paul et al., 2004)

4. Baffles: Are essentially designed to avoid vortices. Flat blade baffles are suggested to be engaged for solid suspension with a width of T/12 to T/10 and a wall clearance of at least T/72 to avoid dead zones behind the baffles (Lu et al., 1997; Paul et al., 2004).

5. Others: The vessel itself is a remarkable portion of the cost of the process and a variable frequency drive is recommended to control the rpm and maintaining a speed above the just suspended speed (N_{js}).

The effect of varying impeller geometrical parameters including impeller type, number of impeller blades, blade angle and thickness of pitched blade impellers in turbulent flow have been studied in solid-liquid suspension (Wu et al., 2001).

2.5 Flow regime

Mixing in stirred vessels may be accomplished in batches to ensure high quality results by minimizing the cost resulting in a high yield and, therefore, enhanced profitability. Understanding the flow regime is crucial to minimize the operation cost. Mixing process in agitated tanks occurs under either laminar or turbulent flow conditions. The flow regime is characterized by the impeller Reynolds number which is defined as:

$$\mathrm{Re} = \frac{\rho \mathrm{N} D^2}{\mu} \tag{2.1}$$

where ρ is the density (kg/m^3) of the fluid and N is the impeller speed in revolution per second (*rps*) and D is the impeller diameter (m) and μ is the fluid viscosity (Pa.s). For Reynolds numbers less than 10, the flow regime is called laminar flow. Turbulent flow conditions are fully achieved if Re is greater than 10^4, and between them is transitional flow. The Reynolds number can provide an indication of flow instability (Tatterson, 1994; Galletti et al., 2004).

2.6 Power consumption in agitated vessels

Power is energy per unit of time which has to be transferred from the impeller to the liquid to keep it in motion. Consequently, it generates a torque which is related to power as follows (Oldshue, 1983):

$$P = 2\pi NM \tag{2.2}$$

where N is impeller revolution (*rps*), M is torque (*N.m*) and P is power (*W*).

2.6.1 Power consumption with regards to flow type

Power consumption in Newtonian fluids is proportional to N^3 and D^5 , but in general it can be a function of the following parameters (Uhl & Gray, 1966; Dickey & Fenic, 1976):

$$f\left[\left(\frac{\rho.D^2.N}{\mu}\right),\left(\frac{D.N^2}{g}\right),\left(\frac{P}{\rho.D^5.N^3}\right),\left(\frac{D}{T}\right),\left(\frac{D}{Z}\right),\left(\frac{D}{C}\right),\left(\frac{D}{p}\right),\left(\frac{D}{w}\right),\left(\frac{D}{l}\right),\left(\frac{b_2}{b_1}\right)\right]=0 \tag{2.3}$$

where $D, T, Z, C, w, p, b, l, \rho, \mu, P, N$, g are the impeller diameter, tank diameter, liquid depth, clearance off the vessel bottom, blade width, pitch of blades, number of blades, blade length, fluid density, fluid viscosity, power, impeller rotational speed and gravitational acceleration, dimensionless numbers an indication of inertial forces to viscous forces (Re Number or $\mathrm{Re} = \dfrac{\rho \mathrm{N} D^2}{\mu}$), inertial to gravitational forces (Froude Number or $Fr = \dfrac{DN^2}{g}$) and Power consumption respectively. Equation (2.3) can be simplified to:

$$P_o = c(Re)^a (N_{Fr})^b \tag{2.4}$$

where *a, b* and *c* are constants and P_o is power number. In fully baffled tank and in the absence of vortices, *b* is zero and power number is just a function of Reynolds number (McDonough, 1992).

Pumping and power can be used to characterize impellers, especially axial impellers. Power (P) is proportional to pumping capacity, Q_p (the ability of the agitator to pump and circulate the fluid) and head, H. The power number (P_o) then is defined as the constant of this proportionality in Equation (2.6). Flow number (Fl) is the proportionality constant of the pumping capacity with respect to impeller speed and diameter (King et al., 1988).

$$P \propto Q_p H = \left(\rho N D^3\right)\left(N^2 D^2\right) \tag{2.5}$$

$$Q_p \propto (N)\left(D^3\right) \tag{2.6}$$

$$P_o = \frac{P}{\rho D^5 N^3} \tag{2.7}$$

$$Fl = \frac{Q_p}{N D^3} \tag{2.8}$$

where ρ is the fluid density (kg/m^3), N is impeller speed (revolution per second), D is impeller diameter (m).

Power number decreases in the laminar flow as the *Re* number increases and during the transition it would be fluctuating whereas, in the turbulent regime is more stable and almost constant. For Reynolds numbers between 100 to 1000, fluctuations of power number has the same profile for both baffled and un-baffled tanks. At *Re* 1000 the power number of un-baffled vessels starts to decrease slightly (Tatterson, 1991).

2.6.2 Power consumption with respect to concentration

Power consumption in single phase flow is mostly dependent upon the agitation rate and the liquid viscosity. If the *Re* number is less than 10, it adversely affects the power. In the higher range of Re numbers, the power number is constant and the effect of the fluid viscosity is negligible.

For slurries, the power number increases up to a certain concentration and then it will drastically increase. The increase in the apparent viscosity of the mixture is determined by the fineness of the particles (Oldshue, 1983). Further studies are discussed in two phase flow.

2.7 Two phase flow

A sound of understanding physics and hydrodynamics of two phase flow is important because many processes in various mixing industries involve more than one phase. Knowledge of the fundamental aspects of the hydrodynamics of single phase flow is a prerequisite for two phase flow because they have the same basic principles. Similarly, multi-phase flow follows the same rules as in two phase flow. Solid-liquid mixing is a part of industrial processes and is a practical example of two-phase flow.

2.7.1 Solid-liquid mixing

Suspension of solids in a liquid requires a mechanical energy through agitation of the liquid and consequently turbulent flow and drag forces to lift the solids to suspension. Essentially, the physical properties of both liquid and solid such as its density, viscosity or particle size as well as geometry and operating condition will affect the mixing.

In a stirred tank there are four forces acting on a particle: gravitational forces due to particle weight and buoyancy effect, inertial forces due to rotational motion, viscous forces due to the drag of liquid on the particle surfaces, and frictional forces due to collision between particles. The majority of solids suspension applications are concerned with completely suspending particles where the settling velocity of the particles is between 2.5 mm/s to 0.1 m/s (Yamazaki et al., 1991). Activated sludge and biological treatment are examples of mediums containing particles with a very low settling velocity (less than 2.5 mm/s) and are very easily homogenized. Systems in which the density of the solid is lower than the fluid, particles try to float and draw down forces were studied by some researchers (Siddiqui, 1993; Ozcan-Taskin & Wei, 2003).

The solids which are often involved in the processes have a density more than twice as the fluid and consequently the homogeneity is not easy to achieve. There have been several studies conducted in this area which all confirm the complexity of the hydrodynamics (Guiraud et al., 1997; Pettersson & Rasmuson, 1998).

2.7.2 Effect of solid physical properties on mixing

Solid density (Oldshue, 1983), particle size (Baldi et al., 1978), particle shape and sphericity (Becker & Can, 1959; Chapman et al., 1983) and solid concentration (Maude, 1958) have different effects which are going to be discussed below on both solid suspension and mixture hydrodynamics which affect settling velocity.

2.7.3 Settling velocity

Processes involving sinking solids are usually revolve around settling velocity, velocity after acceleration from zero to steady state velocity, at which the drag force balances the buoyancy and gravitational forces without interaction between solid particles. The settling velocity in an agitated tank with turbulent flow is hard to find, but it is a function of free settling velocity (Guiraud et al., 1997). The impact of settling velocity can be divided into the following regims: easy (V_s = 0.1-0.6 ft/min), moderate (V_s = 4-8 ft/min), or hard to suspend (V_s = 16-60 ft/min) (Oldshue, 1983).

The free settling velocity for spherical particle is estimated using the following equation (Perry & Green, 1984):

$$V_t = \left(\frac{4g_c d_p(\rho_s - \rho_l)}{3C_D\rho_l} \right)^{1/2} \quad (2.9)$$

g_c is the gravitational constant, 32.17 ft/sec^2 or 9.81 m/s^2, d_p is the particle diameter (m), ρ_s is the particle density (kg/m^3), ρ_l is the liquid density (kg/m^3) and C_D is the drag coefficient, a function of particle Reynolds number:

$$\mathrm{Re}_p = \frac{\rho_l V_t d_p}{\mu} \quad (2.10)$$

Drag coefficient decreases linearly ($C_D = 24/Re_p$) with Reynolds increase in laminar regim while in the turbulent regime , it stays constant ($C_D = 0.445$). For the Newtonian turbulent regime, $Re_p > 1000$ the expression to calculate terminal velocity V_t will change to:

$$V_t = 1.73\left(\frac{g_c d_p(\rho_s - \rho_l)}{\rho_l} \right)^{1/2} \quad (2.11)$$

2.7.4 Solid particle size effect

Since in the mixing industries there is always a size distribution for particles, a mean particle size d_p would be effective to characterize the system (Baldi et al., 1978):

$$d_{p(ave)} = \frac{\sum_{i=1}^{N} n_i d_i^{\,4}}{\sum_{i=1}^{N} n_i d_i^{\,3}} \quad (2.12)$$

where $d_{p(ave)}$ is the average particle diameter and n_i is number or mass fraction of the particle with d_i size. The particle size distribution and power consumption were experimentally measured for different size diameter from 0.2-0.9 mm (Angst & Kraume, 2006).

2.8 Particle shape effect

Particle shape affects the homogeneity of the mixture and, therefore, the rates of the desired outcomes (i.e. crystallization, mass transfer, etc.). Particle shape is usually quantified by Ψ which is the ratio of the surface area of a spherical particle of the same volume to that of non-spherical particle. If Ψ is between 0.7-1, Equation (2.9) is still applicable (Chapman et al., 1983).

2.9 Solid concentration effect

Once the concentration of solid particles increases, the settling velocity changes to hindered settling velocity due to the particle-particle interaction. The upward flow of the fluid created by the settling particles and the increase in apparent viscosity affect particles terminal velocity. An empirical correlation for this case is derived as (Maude, 1958):

$$V_{ts} = V_t\left(1-x\right)^n \tag{2.13}$$

where V_{ts} the hindered settling velocity (m/s or ft/s) for mono dispersed solid and V_t is the free settling velocity (m/s or ft/s) and x is the volume fraction of solids in the slurry and $n = 4.64$ for $\mathrm{Re}_p \le 0.3$, $n = 4.375\,\mathrm{Re}_p^{-0.0875}$ for $0.3 < \mathrm{Re}_p \le 1000$ and $n = 2.33$ for $\mathrm{Re}_p > 1000$.

2.10 Off-bottom suspension and degree of uniformity

2.10.1 Just suspended impeller speed approach

There is an important impeller speed in solid suspension at which solid particles start to move and there is no particle left idle at the bottom more than one second. In other words, at any other speed less than the speed noted above there is no mixing happening. This speed is known as "just suspended speed" N_{js}. Degree of uniformity comes into picture at any speed greater than N_{js} which shows how uniform the solid concentration and particle size distribution are throughout the whole vessel. For instance, if the solid concentration variation is about 0.05, the uniformity is considered adequate for most of processes. A 100% degree of uniformity is impractical because there is always a few inches at the surface which has less concentration as a consequence of less axial lift velocity (Paul et al., 2004).

The first successful study on solid-liquid mixing refers to the Zwietering (1958) model which can predict the just suspended speed of solids with a concentration of less than 20 wt%:

$$N_{js} = S.\left(\frac{g.\Delta\rho}{\rho_L}\right)^{0.45}\left(\frac{X^{0.13}d_p^{\ 0.2}\upsilon^{0.1}}{D^{0.85}}\right) \tag{2.14}$$

where S is Zwietering N_{js} constant and can be calculated for a system with specified geometry, g is the gravity, $\Delta\rho = \rho_p - \rho_l$, ρ_p (kg/m^3)is the particle density, ρ_l is the liquid density (kg/m^3), υ is the kinematic viscosity (m^2/s), d_p is the particle diameter (m), X is the solid weight fraction, and D is the impeller diameter (m). This equation is believed to be valid for a particle size range of 0.2-1mm ((Paul et al., 2004).

Later Baldi et al., (1978) derived a similar expression for N_{js} but considering turbulent arguments such as eddy in deriving the empirical equation. Numerous experimental studies have been conducted to determine the effect of different geometry parameters on the hydrodynamic of the system. The results have been compared with Zwietering model as well and some modifications were presented.

The effect of baffle design on liquid mixing and consequently the hydrodynamics of the medium for a Rushton turbine impeller have been investigated numerically and the effect of parameters in fully fixed conditions were compared with experimental results by Lu et al. (1997). Axial concentration profile was firstly illustrated by Baldi et al. (1981) and followed in more details by Barresi & Baldi (1987). The axial and radial concentrations were measured through sampling from different locations. Later Yamazaki et al. (1991) tried to find out a relationship between power consumption and solid concentration.

2.10.2 Mixing time approach

Mixing time was employed to characterize the mixing hydrodynamics by other researchers (Bujalski et el., 1999; Katsuhide and Takahashi, 2005). It is very practical in single phase or homogeneous mixtures. However, mixing time cannot locally describe the mixing quality.

2.10.3 Homogeneity approach

2.10.3.1 Clouding height

Mixing homogeneity is an essential parameter to investigate in order to understand mixing hydrodynamics. Homogeneity is desired in virtually all solid-liquid mixing flows. Some researchers encountered clouding height as an indication of mixing homogeneity and tried to correlate them (Bittorf & Kresta., 2003; Einenkel, 1980; Hicks et al., 1997). Clouding height is the height of the suspended solid particles in the tank at a given impeller speed. Einekel (1980) presumed homogenous state as of 90% of the liquid height while Bittorf and Kresta (2003) assumed full clouding height up to liquid level as homogeneous state and derived an equation to estimate the clouding height:

$$C_H = \frac{N}{N_{js}}\left(0.84 - 1.05\left(\frac{C}{T}\right) + 0.7\frac{\left(\frac{D}{T}\right)^2}{1-\left(\frac{D}{T}\right)^2}\right) \tag{2.15}$$

where C_H is the clouding height (m), C (m), D (m) and T (m) are the impeller clearance, impeller diameter and tank diameter respectively.

The effect of stirrer type, angle and shape of blades, rotation direction, and number of impeller, baffle height and power input on clouding height are investigated by Biswas et al. (1998) through photography and visual observation.

2.10.3.2 Concentration Profile

Concentration profiles may be adopted to study the system homogeneity. Different methods such as the light attenuation technique (Godfrey and Zhu, 1994), laser beam (Montante et al., 2001; Shamlou and koutsakos, 1989), conductivity probe (Myers et al., 1995; Spilda et al., 2005), electrical resistance tomography (Ricard et al., 2005) and sampling (Einenkel, 1980; Wang et al., 2006) have been employed to predict the concentration profiles. Most of these methods are either not applicable to opaque systems or are limited to a small local area. Light attenuation technique and laser beam demand translucent systems and they are not efficient in opaque systems. Sampling and conductivity probe are subjected to local space and human error. Both methods are invasive to flow hydrodynamic. In contrast tomography is a non-intrusive method to study local concentration thoroughly.

2.11 Tomography

Flow visualization has been recently become a powerful technique to study the flow behavior of a system. Different techniques may be employed upon the system limitations to overcome the challenges in flow visualization (Mavros, 2001). Mavros (2001) has also mentioned pros and cons of each method in detail. One of the most recently popular techniques in visualizing multi phase flow is tomography. Tomography has technically a Greek root and means slice imaging. Tomography includes categorizations such as Positron Emission Tomography (PET) (West et al., 1999), Nuclear Magnetic Resonance (NMR)(Gladden,1994), Ultra Sound Tomography (Hagenson & Doraiswamy, 1998) and Electrical Tomography (Reinecke et al., 1998).

Having no moving parts in the sensors and consequently a short switching time between sensors has given electrical tomographic techniques high temporal resolution, which is considered essential for visualizing multi-phase flows (Reinecke et al., 1998). Tomographic machines perform an integral measurement on a specific property of an object. Based on this measurement and with the assistance of a mathematical description, series expansions or inversions, the object or the property in favor is reconstructed. This mathematical description will allow the user to predict the spatial property within the allotted time frame.

Electrical resistance tomography (ERT), fairly new in chemical engineering and processing, has different applications specifically in the mixing field such as miscible liquids (Holden et al., 1998), solid-liquid (Ricard et al. 2005; Stanley et. al, 2002,2006,2008) ,non-newtonian opaque fluid (Pakzad et al. 2008). A brief literature review of the most recent application of ERT is tabulated in Table 2.1.

Table 2.1 Applications of ERT in mixing

References	Tomography Method/System under observation	Objective	Findings/Comments
McKee et al., 1995	ERT,PET/Solid-liquid in vessel	To determine N_{js} and effect of impeller speed on concentration profile	Good agreement with Zweitering's correlation
Williams et al., 1996	ERT/Solid-liquid in vessel	To study the effect of impeller type, particle size	Concentration profile determined with four planes to some extent but needed more data
Mann et al., 1997	ERT/Gas-liquid, solid-liquid in vessel	To develop a model to predict the conductivity in three dimensional	Successful in calculating the conductivity spatially/ Useful for post-processing
Williams et al., 1998	ERT,ECT/Gas-liquid, solid-liquid in vessel	To test the ability of tomography system for monitoring the mixing behavior on line	Successful monitoring in both aqueous and organic media
Holden et al., 1998	ERT/Miscible liquids in vessel	To evaluate two impeller performance in plant scale	Optimized the impeller position by employing mixing time
Holden et al, 1999	ERT/ Gas-liquid in vessel	To generate 3-D data and evaluate the gas sparger position	ERT capability of malfunctioning diagnosis/ good for computational comparison qualitatively

Table 2.1 continued (1)

References	Tomography Method/System under observation	Objective	Findings/Comments
West et al., 1999	ERT,PET/Solid-liquid in vessel	To test the ability of ERT and PET in monitoring the system	PET was unable to pick the changes within the system due to low temporal resolution
Wang et al., 2000	ERT/Gas-liquid in vessel	To measure the gas hold up	Higher viscous fluid hold less gas
Stanley et al., 2002	ERT/Solid-liquid in vessel	To control the precipitation rate	Mixing was far from ideal
White & Doblin, 2003	EIT/Gas-liquid in vessel	To measure gas dispersion	Performance of A310 evaluated, gas flow rate and impeller speed were optimized
Wang et al., 2003	ERT/Solid-liquid, swirl flow in pipe	To quantify the solid concentration in pipe	A critical velocity for the flow was determined above which there is a drastic concentration gradient
Madupu et al., 2005	ERT/Solid-liquid	To measure the solid level in an underground storage tank	Solid height was measured, the solid-liquid interface was clearly detected
Ricard et al., 2005	ERT/Liquid-liquid, solid-liquid in vessel	To mimic mixing process in pharmaceutical production reactor	Major achievement in geometry optimization

Table 2.1 continued (2)

References	Tomography Method/System under observation	Objective	Findings/Comments
Stanley, 2006	ERT/ solid-liquid in vessel	To evaluate the state of precipitation by measuring the solid concentration	Kinetic of precipitation was studied, solid concentration profile and images were made
Grellier et al., 2006	ERT/solid-liquid in vessel	To study the temperature effect on conductivity	A linear relationship found between temperature and conductivity
Giguère et al., 2008	ERT/solid-liquid in pipe	To study the solid concentration profile	Fair noise reduction through different conductivity calculation algorithm to result better concentration contour
Pakzad et al., 2008	ERT/liquid-liquid in vessel	To study the cavern size in non-Newtonian fluid with yield stress	The size of cavern was successfully visualized
Zhao et al., 2008	ERT/liquid-liquid in vessel	To study the effect of UV lamps in photo-reactors on hydrodynamics	The position of four UV lamps were optimized

2.12 Computational fluid dynamics (CFD)

2.12.1 Introduction

Computational fluid dynamics (CFD) is a way of analyzing a system involving fluid flow and other associated phenomena through mathematical modeling and simulation by means of computer based programs. Initially, CFD was used in the aerospace industry in the 1960's and because of the compatibility of CFD with other industrial processes and its ability to predict the flow behavior; it was extended to most other industries such as automobile and aircraft manufacturers.

CFD has recently been engaged to solve the governing equations in agitated tanks and is pronounced to be the most promising tool in predicting flow patterns. The capability of CFD for simulation of different processes made it widely used for predicting the flow behavior and other related parameters although it is highly depended on the accuracy of governing equations and assumptions made toward simplification. The use of CFD in agitated tanks modeling solves the governing equation, the equations of motion and continuity equation simultaneously. Hence, the output would be the velocity profile distributed in the whole system. By having velocity profile, other parameters such as concentration could be determined too.

2.12.2 CFD codes

CFD codes are based on numerical mathematics and where numerical algorithms are engaged to tackle the problem. They consist of three major parts: pre-processor, solver, and post processor. In pre-processor the problem is usually defined. This includes the system geometry, fluid properties, other definitions involving the system, grid generation and grid dependency and boundary condition application. Solvers are constructed based on three numerical solution techniques: finite difference, finite element, and spectral methods. CFX/ANSYS, FLUENT, PHOENICS and STAR-CD softwares use finite volume, a special finite difference formulation and solve the problem through the following steps:

1. Integration of the governing equations over the specified domain for all control volumes,
2. Discretization of the resulting integral equations to algebraic equations,
3. Using an iterative method to solve the system of algebraic equations.

A clear relationship between the numerical algorithm, the physical conservation principles at each cell and the simplicity of the finite volume concept attracted engineers to use it more than finite element and spectral methods (Versteeg & Malalasekera, 2007).

2.12.3 Conservation Laws Applicable to the System

Mass, momentum and energy of a fluid in a system are conserved. The governing equations of flow can be based on any applicable conservation laws of physics. The general format of these laws in a controlled volume is:

$$\left(\text{rate of an entity change}\right)=\left(\text{rate of entity in}\right)-\left(\text{rate of entity out}\right)+\left(\text{rate of entity generation}\right)$$

2.12.4 Single phase flow

Single phase flow fundamentals are incorporated with all mixing processes as they are either one phase or a medium holding the different phases. Therefore, understanding single phase flow is crucial to multiple phase flow.

2.12.4.1 Continuity and momentum equations in single phase flow

Continuity and momentum as a statement of mass and momentum conservation for a Newtonian and incompressible fluid can be written as follows (Bird et al., 2002):

$$\frac{\partial \rho}{\partial t}=-\left(\nabla.\rho\vec{u}\right) \qquad (2.16)$$

in which the left hand side is the rate of increase of mass per unit volume which is equal to the net rate of mass addition per unit volume by convection. Applying the Newton's law of motion to the control volume, the equation of motion is as follows (Bird et al., 2002):

$$\frac{\partial \rho \vec{u}}{\partial t} = -\left(\nabla.\rho\vec{u}\vec{u}\right) - \nabla p - \left(\nabla.\overline{\overline{\tau}}\right) + \rho\vec{g} + \vec{F} \tag{2.17}$$

where ρ is fluid density, $\rho\vec{u}$ is mass velocity vector, $\rho\vec{u}\vec{u}$ is connective momentum tensor, $\overline{\overline{\tau}}$ is stress tensor, g is gravitational acceleration vector, p is the fluid pressure and $\vec{F}$ is any external forces. The left-hand side is an indication of rate of momentum increase which is equal to the sum of the rate of momentum in, momentum out and external forces acting on the fluid.

$$\overline{\overline{\tau}} = \overline{\overline{\tau}}^{v} + \overline{\overline{\tau}}^{t} \tag{2.18}$$

where $\overline{\overline{\tau}}^{v}$ is stress tensor of the viscous flow and $\overline{\overline{\tau}}^{t}$ is the stress tensor of the turbulent flow or Reynolds stress tensor. The viscous stress tensor is defined as (Fluent Inc., 2006):

$$\overline{\overline{\tau}}^{(v)} = \mu\left(\left(\nabla\vec{v} + \nabla\vec{v}^{T}\right) - \frac{2}{3}\nabla.\vec{v}I\right) \tag{2.19}$$

where $\nabla\vec{v}^{T}$ is the transpose of $\nabla\vec{v}$ and by employing the Boussinesq hypothesis ,which was an imply from the Newton's law of viscosity in laminar flow, the turbulent stress tensor is defined as (Fluent Inc., 2006):

$$\overline{\overline{\tau}}^{(t)} = \mu_t\left(\nabla\vec{v} + \nabla\vec{v}^{T}\right) - \frac{2}{3}\left(\rho k + \mu_t\nabla.\vec{v}\right)I \tag{2.20}$$

where μ_t is the turbulent viscosity and k is turbulent kinetic energy. If the medium is incompressible $\nabla.\vec{v} = 0$ and therefore Equation (2.18) changes to (Fluent Inc., 2006):

$$\overline{\overline{\tau}} = \left(\mu + \mu_t\right)\left(\nabla\vec{v} + \nabla\vec{v}^{T}\right) - \frac{2}{3}\rho k\overline{\overline{I}} \tag{2.21}$$

The Boussinesq hypothesis, the turbulent viscosity and kinetic energy will be discussed in detail in the turbulent section.

2.12.5 Two phase flow

CFD approaches solving multi-phase in two different ways which are called Lagrangian-Eulerian and Eulerian-Eulerian methods. In Lagrangian-Eulerian, the medium is considered as the continuum phase and solid, gas or another immiscible liquid as the dispersed. The continuum in a fixed control volume is being calculated based on conservation of mass and momentum and dispersed phase is being tracked in Δt in regards to dispersed velocity. In Eulerian-Eulerian both phases are treated in a fixed control volume but different velocities. In both approaches the phases are coupled by $\sum \varphi = 0$ where φ is the weight fraction of the phases (Kleinstreuer, 2003).

If the continuum is an incompressible Newtonian fluid, the equation of motion is simplified to Navier-Stoks equation.

2.12.6 Settling suspension flow modeling

Settling particle flows are different considerably in three essential concepts with non-settling particle flows: need to be averaged, flow pattern and interface interaction (Peker, 2008). In these types of flows, specific gravity difference causes concentration gradient and segregation and consequently averaging should be applied to Navier-Stokes equation to make it applicable for flow modeling. No matter whatever the flow pattern is, the interfacial interaction exists and should be applied to momentum equation.

2.12.6.1 Eulerian-Lagrangian approach

Eulerian approach as a fixed control volume is usually applied to the continuum while the discrete phase can be treated differently. The discrete phase in Lagrangian frame is tracked and trajectories of these discrete phase entities are computed. Subsequently, the coupling between the phases and its impact on both phases can be included (Fluent, 2006).

In the Lagrangian approach the position of particles is calculated as:

$$\frac{dx_{i_p}}{dt} = \vec{u}_p \tag{2.22}$$

where x_{i_p} is the three coordinates of the particle and the particle velocity vector ($\vec{u}_p$) is found after applying the Newton's law of motion:

$$\sum \overrightarrow{F} = \frac{d}{dt}\left(m_p \vec{u}_p\right) \tag{2.23}$$

Despite Eulerian approach that the mass within the control volume changes, in Lagrangian method the mass within control volume is fixed. Hence Newton's law of motion turns to:

$$\sum \overrightarrow{F} = m_p \frac{d}{dt}\vec{u}_p \tag{2.24}$$

or:

$$m_p \frac{d}{dt}\vec{u}_p = \overrightarrow{F_D} + \overrightarrow{F_g} + \overrightarrow{F_B} + \overrightarrow{F_{vm}} + \overrightarrow{F_l} + \overrightarrow{F_M} + \overrightarrow{F_S} + \overrightarrow{F_{Br}} + \overrightarrow{F_{Int}} \tag{2.25}$$

where m_p, $\vec{u}_p$, $\overrightarrow{F_D}$, $\overrightarrow{F_g}$, $\overrightarrow{F_B}$, $\overrightarrow{F_{vm}}$, $\overrightarrow{F_l}$, $\overrightarrow{F_M}$, $\overrightarrow{F_S}$, $\overrightarrow{F_{Br}}$ and $\overrightarrow{F_{Int}}$ are the particle mass, velocity, drag force, gravity force, buoyancy force, virtual mass force, lift force, Mangus force, stress force, Brownian force, and interaction force between particle-particle including collisions, respectively. Drag force applicable in this case is quite similar to Eulerian approach and will be discussed in details in the Eulerian approach section. The combination of gravity force and Buoyancy force is given by:

$$\overrightarrow{F_g} + \overrightarrow{F_B} = \frac{\pi}{6} d_p^3 \left(\rho_p - \rho_l\right) g \tag{2.26}$$

where d_p, ρ_p and ρ_l are particle diameter, particle density and liquid density respectively.

Virtual mass force (also known as added mass force) which is the force required to accelerate the fluid surrounding the particle can be derived from (Zhang & Ahmadi, 2005):

$$\overrightarrow{F_{vm}} = -\frac{1}{12}\pi d_p^3 \rho_l \frac{d}{dt}\left(\overrightarrow{u_p} - \overrightarrow{u_l}\right) \tag{2.27}$$

where $\vec{u}_p$ and $\vec{u}_l$ are particle velocity and liquid velocity respectively. The lift force or Saffman force, or lift due to shear and rotation of the fluid, is given by (Derksen, 2003, Saffman, 1965):

$$\overrightarrow{F_l} = \frac{\pi}{4} d_p^3 \frac{\rho_l}{2} C_s \left(\left(\overrightarrow{u_l} - \overrightarrow{u_p}\right) \times \omega\right) \tag{2.28}$$

where ω is the angular velocity and for $\mathrm{Re}_p \geq 40$ is $C_s = 0.1524$ where for $\mathrm{Re}_p < 40$ C_s can be found as follows (Derksen, 2003, Saffman, 1965):

$$C_s = \frac{4.1126}{\mathrm{Re}_{SR}^{0.5}}\left[\left(1.0 - 0.234\left(\frac{\mathrm{Re}_{SR}}{\mathrm{Re}_p}\right)^{0.5}\right) e^{-0.1\mathrm{Re}_p} + 0.234\left(\frac{\mathrm{Re}_{SR}}{\mathrm{Re}_p}\right)^{0.5}\right] \tag{2.29}$$

where Re_{SR} is the rotational Reynolds number and can be calculated from the equation (2.30).

$$\mathrm{Re}_{SR} = \frac{|\omega| d_p^2}{\upsilon} \tag{2.30}$$

where υ is the kinematic viscosity of the medium.

If the particle rotation is not equal to fluid rotation beside Saffman lift force another force will come into picture. Mangus force is caused by rotation of the particle in a stream and as a consequence there is a pressure difference between the top and the bottom of the particle. This pressure difference causes a force to the particle and is defined as (Derksen, 2003):

$$\overrightarrow{F_M} = \frac{\pi}{4} d_p^2 \frac{\rho_l}{2} C_M \left|\overrightarrow{u_l} - \overrightarrow{u_p}\right| \left(\frac{(\omega - 2\omega_p) \times \left(\overrightarrow{u_l} - \overrightarrow{u_p}\right)}{|\omega - 2\omega_p|}\right) \tag{2.31}$$

Where ω_p is the angular velocity of the particle and the lift coefficient C_M is found by:

$$C_M = 0.45 + \left(\frac{\mathrm{Re}_{MR}}{\mathrm{Re}_p} - 0.45 \right) e^{-0.05684\,\mathrm{Re}_{MR}^{0.4}\,\mathrm{Re}_p^{0.3}} \tag{2.32}$$

Where Re_{MR} is the particle rotational Reynolds number and is defined as:

$$\mathrm{Re}_{MR} = \left| \frac{1}{2\omega} - \omega_p \right| \frac{d_p^2}{\upsilon} \tag{2.33}$$

Where ω and ω_p are the fluid angular velocity and particle angular velocity (rps) respectively. In order to find the angular velocity of the particle, the following dynamic equation should be solved:

$$\frac{d\omega_p}{dt} = \frac{60}{d_p^2} \frac{\rho_l}{\rho_p} \upsilon \left(\frac{1}{2}\omega - \omega_p \right) \tag{2.34}$$

which is valid for $\mathrm{Re}_{MR} \le 30$ (Dennis et al., 1980). Stress force is given by:

$$\overrightarrow{F_S} = \frac{\pi}{6} d_p^3 \left(-\nabla p + \rho_l \upsilon \nabla^2 \overrightarrow{u_l} \right) \tag{2.35}$$

where d_p is the particle diameter (m), p is the fluid pressure, ρ_l is the fluid density (kg/m^3) and $\overrightarrow{u_l}$ is the liquid velocity vector. The Brownian force is related to sub-micron particles and its components are modeled as a Gaussian white noise process with spectral intensity (Li & Ahmadi, 1992). Once particles are spotted, after velocity field solved and particle coordinates x_{i_p} are calculated, there would be a chance of interaction forces $\overrightarrow{F_{Int}}$ such as collision between particle and impeller blade or particle-particle collision. At the event of particle-blade collision, the particle velocity is modified by:

$$\overline{u_{p,\theta,out}} = -\overline{u_{p,\theta,in}} + 2r_p\Omega \tag{2.36}$$

where $\overrightarrow{u_{p,\theta,out}}$, $\overrightarrow{u_{p,\theta,in}}$ and $r_p\Omega$ are particle tangential velocity after collision, particle tangential velocity before collision and local velocity of the blade surface. Ω is the tip velocity and is given by:

$$\Omega = 2\pi N \tag{2.37}$$

where N (rps) is the impeller speed. Particle-particle collisions are anticipated and different collision algorithms offered in the open literature can be employed to approach the matter depending on the computational expenses affordability (Chen et al., 1998a, b; Peker, 2008; Sommerfeld, 2001). Hard sphere collision is assumed by Hoomans et al. (1996) to simplify collision algorithm derivation. Sliding and sticking condition were two main criteria in their transport phenomena calculation.

2.12.6.2 Eulerian-Eulerian approach

This approach considers the dispersed phase as a continuous phase, interpenetrating and interacting with medium phase. Local equations for the instantaneous changes are developed together. Equations resulted from conservation of laws must be averaged either in time, space or as an ensemble which is the statistical average of micro-systems properties representing macroscopic properties with respect to time and space (Peker, 2008). The constitutive equations are required to mimic the particle-particle interactions which are mostly empirical. In this study, time averaged Navier-Stokes and Gidaspow empirical drag coefficient correlation for solid-liquid interaction were used to model the problem. For simplicity, one single particle size was considered since multi particle size multiplies the number of equations which have to be coupled for solution.

Continiuty equation (Fluent Inc., 2006):

$$\frac{\partial(a_k \rho_k)}{\partial t} + \nabla.\left(a_k \rho_k \overrightarrow{u_k}\right) = 0 \tag{2.38}$$

and the momentum equation is as follows (Fluent Inc., 2006):

$$\frac{\partial}{\partial t}\left(a_k \rho_k \overrightarrow{u_k}\right)+\nabla.\left(a_k \rho_k \overrightarrow{u_k}\,\overrightarrow{u_k}\right)= \\ -a_k \nabla p+\nabla.\left(\overline{\overline{\tau_k}}\right)+a_k \rho_k g+(\vec{F}_D+\vec{F}_{Bk}+\vec{F}_{Lk}+\vec{F}_{vmk}) \tag{2.39}$$

where $\overline{\overline{\tau_k}}$ is the k[th] phase stress-strain tensor:

$$\overline{\overline{\tau_k}}=\alpha_k\left(\mu_k+\mu_{kt}\right)\left(\nabla \overrightarrow{u_k}+\nabla \overrightarrow{u_k}^{T}\right)-\frac{2}{3} \alpha_k \rho_k k_k \overline{\overline{I}} \tag{2.40}$$

here subscript k symbolizes phase k, and μ_k, μ_{kt}, K_k $\vec{F}_D$, $\vec{F}_{Bk}$, $\vec{F}_{Lk}$, and $\vec{F}_{vmk}$ are the shear viscosity, turbulent viscosity, turbulent kinetic energy, drag force, Buoyancy force, lift force, and virtual mass force respectively.

$$\vec{F}_D=\sum K_{lk}(\overrightarrow{u_l}-\overrightarrow{u_k}) \tag{2.41}$$

Where K_{lk} is the exchange coefficient between liquid and the phase k th. $\vec{F}_{Bk}$, $\vec{F}_{Lk}$ and $\vec{F}_{vmk}$ are considerably small compared to the dominant drag force and interaction forces between two phases, if the particles density ratio to liquid is more than 2 (Tatterson, 1991).

2.12.6.2.1 Solid-liquid exchange coefficient

The exchange coefficient of phase k, K_{lk} for solid phase is K_{lp} which is equal to K_{pl}. Solid-liquid exchange coefficient, K_{pl} is defined as (Fluent, 2006):

$$K_{pl}=\frac{\alpha_p \rho_p f}{\tau_p} K_{lp} \tag{2.42}$$

where α_p is the solid volume fraction, ρ_p is the particle density and τ_p, the particulate relaxation time is

$$\tau_p = \frac{\rho_p d_p^{\ 2}}{18\mu_l} \tag{2.43}$$

and f is described as (Syamlal & O'Brien, 1989):

$$f = \frac{C_D \operatorname{Re}_r \alpha_l}{24 u_{tp}^{\ 2}} \tag{2.44}$$

where u_{tp} is the terminal velocity of the particles and Re_r, C_D are relative Reynolds number, drag coefficient, respectively, and defined as (Dalla, 1948):

$$C_D = \left(0.63 + \frac{4.8}{\sqrt{\operatorname{Re}_r / u_{tp}}}\right)^2 \tag{2.45}$$

and $\operatorname{Re}_r^{\bullet}$ is:

$$\operatorname{Re}_r = \frac{\rho_l d_p \left|\overrightarrow{u_p} - \overrightarrow{u_l}\right|}{\mu_l} \tag{2.46}$$

where subscripts l and p stand for liquid and solid phase, respectively. Solid-liquid exchange coefficient will finally change to:

$$K_{pl} = \frac{3\alpha_p \alpha_l \rho_l}{4u_{tp} 2d_p} C_D \left(\frac{\operatorname{Re}_r}{u_{tp}}\right) \left|\overrightarrow{u_p} - \overrightarrow{u_l}\right| \tag{2.47}$$

The terminal velocity of solid particle is given by (Garside & Al-Dibouni, 1977):

$$u_{tp} = 0.5(A - 0.06\,\mathrm{Re}_r + \sqrt{(0.06\,\mathrm{Re}_r)^2 + 0.12\,\mathrm{Re}_r(2B - A) + A^2}) \tag{2.48}$$

where:

$$A = \alpha_l^{4.14} \tag{2.49}$$

$$B = 0.8\alpha_l^{1.28} \text{ if } \alpha_l \le 0.85 \tag{2.50}$$

and

$$B = \alpha_l^{2.65} \text{ if } \alpha_l > 0.85 \tag{2.51}$$

The inter drag coefficient is defined (Wen & Yu, 1966) as:

$$K_{pl} = \frac{3\alpha_p \alpha_l \rho_l}{4d_p} C_D \left|\overrightarrow{u_p} - \overrightarrow{u_l}\right| \alpha_l^{-2.65} \quad \text{if } \alpha_l > 0.8 \tag{2.52}$$

and

$$K_{pl} = 150\frac{\alpha_p (1-\alpha_l)\mu_l}{\alpha_p {d_p}^2} + 1.75\left|\overrightarrow{u_p} - \overrightarrow{u_l}\right| \frac{\rho_l \alpha_p}{d_p} \quad \text{if } \alpha_l \le 0.8 \tag{2.53}$$

where an empirical C_D is expressed by Gidaspow et al. (1992) model as follows:

$$C_D = \frac{24}{\alpha_l\,\mathrm{Re}_r}\left[1 + 0.15\left(\alpha_l\,\mathrm{Re}_r\right)^{0.687}\right] \text{ if } \mathrm{Re}_r \le 1000 \tag{2.54}$$

$$C_D = 0.44 \quad \text{if } \mathrm{Re}_r > 1000 \tag{2.55}$$

This is proposed for dense fluidized beds.

2.12.7 Turbulent model

Turbulence includes a vast majority of industrial flows and the complexities of turbulence made turbulence modeling a very challenging and never-ending task. Settling solid suspension in agitated tanks is one of the examples of turbulent flow. Although turbulence requires higher energy to overcome the extra drag but desirable for enhanced mixing and dispersion (Kleinstreuer, 2003). Fully baffled tank with water in the continuum phase has to be in the turbulent regime to be able to suspend the heavy solid. $Re > 10^4$ indicates of turbulent regime in agitated tanks. Re is defined as in Equation (2.1). In the turbulent regime the velocities will fluctuate and consequently, the momentum equation, not the continuity equation, will have an extra term which describes the fluctuations to the mean velocities.

Since these fluctuations can be of small scale and high frequency, they are too computationally expensive to simulate directly in practical engineering calculations. Instead, the instantaneous (exact) governing equations can be time-averaged, ensemble-averaged, or otherwise manipulated to remove the small scales, resulting in a modified set of equations that are computationally less expensive to solve. However, the modified equations contain additional unknown variables, and turbulence models are needed to determine these variables in terms of known quantities (Fluent Inc., 2006).

In Reynolds averaging technique, the solution variables in the instantaneous (exact) Navier-Stokes equations are decomposed into the mean and fluctuating components. For the velocity components:

$$u_i = \bar{u}_i + u_i' \tag{2.56}$$

where $\bar{u}_i$ and u_i' are the mean and fluctuating velocity components. Similar expressions can be written for scalar quantities like pressure. Substituting expressions of this form for the flow variables into the instantaneous continuity and momentum equations and taking a time average (and dropping the overbar on the mean velocity and mean pressure) yields the time-averaged momentum equations. They can be written in Cartesian tensor form as:

$$\frac{\partial \rho}{\partial t}+\frac{\partial}{\partial x_i}(\rho u_i)=0 \tag{2.57}$$

$$\frac{\partial}{\partial t}(\rho u_i)+\frac{\partial}{\partial x_j}(\rho u_i u_j)=-\frac{\partial p}{\partial x_i}+\frac{\partial}{\partial x_j}\left[\mu\left(\frac{\partial u_i}{\partial x_j}+\frac{\partial u_j}{\partial x_i}-\frac{2}{3}\delta_{ij}\frac{\partial u_l}{\partial x_l}\right)\right]+\frac{\partial}{\partial x_j}\left(-\rho\overline{u_i' u_j'}\right) \tag{2.58}$$

The momentum equation can be rewritten in vector-tensor from as:

$$\frac{\partial}{\partial t}\rho\vec{v}+\left[\nabla.\rho\vec{v}\vec{v}\right]=-\nabla p+\left[\nabla.\left(\overline{\overline{\tau}}^{(v)}+\overline{\overline{\tau}}^{(t)}\right)\right] \tag{2.59}$$

In which viscous stress tensor is defined as:

$$\overline{\overline{\tau}}^{(v)}=\mu\left(\nabla\vec{v}+\nabla\vec{v}^{T}-\frac{2}{3}\mu\nabla.\vec{v}I\right) \tag{2.60}$$

and turbulent stress tensor:

$$\overline{\overline{\tau}}^{(t)}=-\rho\overline{u_i' u_j'} \tag{2.61}$$

The above equations are called Reynolds-averaged Navier-Stokes equations. They have the same general form as the instantaneous Navier-Stokes equations, with the velocities and other solution variables now representing time-averaged values. Additional term now appear that represent the effects of turbulence. These Reynolds stresses $\overline{\overline{\tau}}^{(t)}$ must be modeled in order to close momentum equation. A common method employs the Boussinesq hypothesis to relate the Reynolds stresses to the mean velocity gradients:

$$\overline{\overline{\tau}}^{(t)}=\mu_t\left(\nabla\vec{v}+\nabla\vec{v}^{T}\right)-\frac{2}{3}\left(\rho k+\mu_t\nabla.\vec{v}\right)I=\mu_t\left(\frac{\partial u_i}{\partial x_j}+\frac{\partial u_j}{\partial x_i}\right)-\frac{2}{3}\left(\rho k+\mu_t\frac{\partial u_k}{\partial x_k}\right)\delta_{ij} \tag{2.62}$$

For incompressible flows $\nabla.\vec{v}=0$ and when flow is highly turbulent the turbulent eddy is considerably bigger than laminar viscosity and consequently the viscous term of the stress tensor is negligible compared to turbulent stress tensor. Using $k-\varepsilon$ model, two additional transport equations (for the turbulence kinetic energy, k and the turbulent dissipation rate, ε are solved to compute the turbulent viscosity, μ_t .K-ε model is the simplest model empirically derived and describes these fluctuations (Launder & Spalding, 1972). Kinetic energy equation is as follows:

$$\frac{\partial}{\partial t}(\rho k)+\frac{\partial}{\partial x_i}\left(\rho k\vec{u_i}\right)=\frac{\partial}{\partial x_j}\left(\left(\mu+\frac{\mu_t}{\sigma_k}\right)\frac{\partial k}{\partial x_j}\right)+G_k+G_b-\rho\varepsilon-Y_M+S_k \tag{2.63}$$

and dissipation transport equation is:

$$\frac{\partial}{\partial t}(\rho\varepsilon)+\frac{\partial}{\partial x_i}\left(\rho\varepsilon\vec{u_i}\right)=\frac{\partial}{\partial x_j}\left(\left(\mu+\frac{\mu_t}{\sigma_k}\right)\frac{\partial\varepsilon}{\partial x_j}\right)+C_{1\varepsilon}\frac{\varepsilon}{k}(G_k+C_{3\varepsilon}G_b)-C_{2\varepsilon}\rho\varepsilon\frac{\varepsilon^2}{k}-Y_M+S_\varepsilon \tag{2.64}$$

where G_k, G_b and Y_M are the generation of turbulence kinetic energy due to the mean velocity gradients, buoyancy and the contribution of the fluctuating dilatation in compressible turbulence to the overall dissipation rate. $C_{1\varepsilon}$, $C_{2\varepsilon}$ and $C_{3\varepsilon}$ are constants and have the following values:

Table 2.2 The standard *k-ε* constants (Fluent Inc., 2006)

$C_{1\varepsilon}$	$C_{2\varepsilon}$	$C_{3\varepsilon}$	C_μ	σ_k	σ_ε
1.44	1.92	$\tanh\left\|\frac{v}{u}\right\|$	0.09	1.0	1.3

where v is the component of the flow velocity parallel to the gravitational vector and u is the component of the flow velocity perpendicular to the gravitational vector. σ_k and σ_ε indicate the k and ε turbulent Prandtl numbers. User-defined source of k and ε may be added as S_k and S_ε. μ_t, the turbulent (or eddy) viscosity, is defined as:

$$\mu_t = \rho C_\mu \frac{k^2}{\varepsilon} \tag{2.65}$$

where C_μ is constant. G_k is defined as:

$$G_k = -\rho \overline{u'_i u'_j} \frac{\partial u_j}{\partial x_i} \tag{2.66}$$

The Standard *k-ε, RNG k-ε*, Realizable *k-ε*, Reynolds Stress Model (RSM), and Large Eddy Simulation (LES) turbulence models are some of the models which they predict the Reynolds stresses. Each model has specific advantages and disadvantages which must be taken into consideration when trying to determine which one suits the best. There will have to be a compromise between central processing unit (CPU) time and accuracy. The most commonly used model is the standard *k-ε* which offers the user a quickly achieved convergence with consistent results. However, the user should be aware that this model assumes an isotropic pressure in fully turbulent flow. For this reason it is not recommended that the standard *k-ε* model be used under this condition. Either the Re-Normalisation Group *(RNG) k-ε* or the realizable *k-ε* would be appropriate for swirling flow situations. Unlike the *RNG k-ε*, the Realizable *k-ε* may also be used in round jets. Should the user be able to manage increased calculation time the Reynolds stress model (RSM) model offers greater benefits in terms the broad flow type compared to the standard *k-ε*. Large eddy simulation (LES) would be the superior choice should the user be interested in sub-computational cell data. Convergence of this model requires a finer mesh than the other models previously mentioned, and consequently it is more time consuming (Paul et al., 2004; Aubin et al., 2004).

2.12.8 CFD modeling of mixing tanks literature

One of the best alternatives to obtain information about the flow behavior beside the experiment is computational fluid dynamics (CFD). It is less costly in terms of materials and time to apply CFD in cases which have good agreement with reality. CFD in regards to mixing tank give detailed insight of the velocity profiles and consequently other parameters in favor such as concentration. There are two major approaches in developing the governing equation. In one method, the control volume is fixed (Eulerian) whereas in the other one the control volume is moving while being tracked (lagrangian).

Eulerian approach is applicable in two phase flow wherever the particle size is small enough to move with fluid flow (Gidaspow, 1994). In this approach all the phases are treated moving with the medium phase, but the interaction between them results in different composition in the control volume. In other words, Newton's second law of motion will be applied to both phases according to their fraction. This assumption may cause discrepancy in concentration prediction. Špidla et al. (2005a) tried to revise the CFD model to minimize the concentration profile discrepancy with experimental data. He studied the effect of different drag coefficient empirical model on concentration prediction and ended up with the best compatibility of a turbulent drag coefficient model for a specific case study. In contrast to Eulerian, Lagrangian model tracks particles within flow domain individually while the interaction among the particles and medium is taken into consideration. This method was applied to two phase flow modeling, virtually all dilute concentration, by different researchers (Sommerfeld & Decker, 2004). In contrast simulated results by Eulerian approach is applicable to higher concentrations which is closer to industrial solid-liquid mixing and consequently less costly in terms of CPU time compared with Lagrangian approach. A summary of the most recent studies for solid-liquid by means of CFD simulation is shown in Table 2.3.

Table 2.3 Using CFD to model mixing processes in solid-liquid literature review

References	CFD Code	Approach Model	Impeller/Experimental	Objective	Findings/Comments
Decker & Sommerfeld 1996	------	Black box Lagrangian	Rushton Turbine and Pitched Blade.	Simulate the flow fields in a tank with respect to velocity	CFD gave satisfactory agreement with experimental data Minor effect of particle size
Kim et al. 1996	-----	Eulerian	-----	Modifying the Navier-Stockes equation in Laminar	New model for Re<5000 with a better fit proposed
Chen & Pereira 2000	------	Lagrangian	Flow in pipes	Simulate the flow fields in a pipe with respect to velocity	Good agreement with experimental with anisotropic turbulent model
Micale et al. 2000	CFX4.2 Simpelec	MRF & k-ε Eulerian	Pitched Blade/SVM,MFM	Concentration profile is overestimated	Both model achieved good agreement with experimental
Altway et al. 2001	Fluent 5.1 ASM	Black box Eulerian	SRJ radial jet	Effect of particle size	No tangible effect seen, d_p =10-87 μm, validated with 87 μm
Barrue et al. 2001	Fluent 5	Black box Eulerian/k-ε	Robin Industries Propellers,2 & 4 blades/LDA	To obtain concentration profiles	Remarkable CFD results/the error analysis was not done hence there is no number for remarkable results
Montante et al. 2001	CFX4.3	SM Eulerian k-ε	PBT/Non-intrusive optical technique, Laser diode and silicon photo diode	Particle size and rpm effect on concentration profile	K-ε has good in fully turbulent RNG is good for transient
Ljungqvist & Rasmuson 2001	CFX4	MRF & k-ε Eulerian	Pitched blade/Phase-doppler anemometry	Study the effect of different drag force	Large deviation between model and exp.for low density or small particle. little different between drag models

Table 2.3 Continued (1)

References	CFD Code	Approach Model	Impeller/Experimental	Objective	Findings/Comments
Sha et al. 2001	CFX4.2	MRF & k-ε Eulerian	PBT 6 blades/literature, He-Ne laser transmitter	To investigate the particle size distribution effect	Good agreement with experimental/No comparison between a uni-size particle made
Ranade et al. 2002	Fluent Quick	Black box & k-ε Eulerian	6PBT/P image Velocimetry	Velocity profile near and far from impeller	Both spots showed good agreement with experimental
Oshinowo & Bakker 2002	Fluent4.52 EGM	MRF & k-ε Eulerian	3 blade Hydrofoil/LDV	Study the effect of Solid loading and cloud height at N_{js}	Very good agreement, scale up criteria had discrepancies with literature
Kaufmann et al. 2002	------	---- Both Eulerian & Lagrangian	------	Effect of Gravity	Eulerian and lagrangian compared and showed an alternative for two phase model
Kee & Tan 2002	Fluent	MRF & k-ε Eulerian	A310,R100/Compared to empirical	To find out N_{js} numerically and the cloud height	N_{js} underestimated by comparing to available empirical model
Derksen 2003	-------	Black box & k-ε Lagrangian	Rushton turbine/ literature	To study the effect of collision and all other forces	Good agreement qualitatively
Wang et al. 2003	Simple	Black box k-ε Eulerian	RT	Concentration profile (axially and radially)	Good agreement with 20% solid w/w
Sommerfeld & Decker 2004	CFX DNS LES	MRF & k-ε RAN Lagrangian	RT	Study the concentration and velocity profile	Due to high computational time DNS failed for Re>8000, LES good agreement up 5%w/w

Table 2.3 Continued (2)

References	CFD Code	Approach Model	Impeller/Experimental	Objective	Findings/Comments
Gentric et al. 2004	---	SM,MRF Eulerian	RT/LDV,PIV	Velocity and concentration profile	SM and MRF for gas-liquid-solid used and velocity profile agrees with experimental
Micale et al. 2004	CFX4.4	SM & k-ε Eulerian	PBT/SVM in literature	To find N_{js} and axial velocity profile	Good agreement from 1 to 10 % w/w with literature
Hao 2005	Fluent 6.0 SIMPELEC	Black box & k-ε Eulerian	PBT/High speed CCD Camera	Velocity profile and concentration profile, effect of density & Particle size	Cloud height good agreement, no big difference in mixture size, segregation is increased by increasing density
Spilda et al. 2005	Fluent6.2	MRF & k-ε Eulerian	PBT/probe conductivity	Study the concentration profile at N_{js}	Particle up to 5%w/w , Higher values of CD recommended, no agreement between e dissipation, Radial concentration profile is more gradient than experimental
Ochieng & Lewis 2005	CFX5.6/5.7	MRF initially and then SM Eulerian	Hydrofoil propeller Mixtec HA735/LDV	Velocity and concentration profile with N_{js}, clearance, solid loading up to 20%, particle size effect	0.15 T clearance adopted as the best option, mesh more than 300 micron has more deviation regarding the experimental than empirical, cloud height measurement failed both in Exp. and CFD for less than 2.5%, visual method advised, N_{js} has 50% error for less than6% w/w loading, off-bottom and unsteady state is suggested, best for developing empirical if low concentration<6% and d_p<150 micron

Table 2.3 Continued (3)

References	CFD Code	Approach Model	Impeller/Experimental	Objective	Findings/Comments
Ricard et al. 2005	Fluent 6 SIMPELEC -QUICK	MRF & k-ε Eulerian	CRT,15 and 45degree/ERT	To find axial Concentration profile at N_{js} and above	Good agreement from 1 to 10 % w/w with literature and ERT. CFD underestimated the concentration up to 20%
Zhang & Ahmadi 2005	-----	Lagrangian	----/Literature	To study the dispersion of different phases	Good agreement with experiment/most of the interaction between the phases are included
Wang et al. 2006	--- SIMPLE	Black box & k-ε Eulerian	6RT/Sampling tubes	Velocity profile and concentration profile, for all three phases at N_{js} and above	good agreement Further improvement needed for CFD model
Khopkar et al. 2006	Fluent6.2	MRF & k-ε Eulerian	RT& PBT/Literature	Study the concentration profile at N_{js} and effect of particle size, drag force	Drag force coefficient should be reduced by 10 times so the CFD is applicable to predict objectives for d_p less than 655 μm and 16%w/w
Tyagi et al. 2006	---------	Immersed boundary method & LES Lagrangian	Multi-impeller, Rushton turbine/Literature	To study the best velocity profile within the tank	Reasonable agreement achieved/ computationally very expensive
Fradette et al. 2007	--- SIMM	k-ε Eulerian	Propeller and helical ribbon/Literature	Velocity profile and concentration profile, Clearance, Particle size	The model is able to predict behavior of suspension
Prat & Ducoste 2007	QMOM Simple	MRF & k-ε Lagrangian & Eulerian	A310 & RT/Literature	Study the concentration profile at Njs and effect of particle size, Impeller	Eulerian prediction was better and more stable than lagrangian

2.13 Research Objectives

Literature review of two phase flow shows a gap in understanding of mixing hydrodynamic specifically when it comes to settling suspensions. In regards to modeling and simulation, recent development in computer made it possible to incorporate more variable and consequently more precision in modeling. Having taken the significance of mixing in agitated tank into consideration and the above mentioned literature review, the objectives of this study lie in the area of solid-liquid mixing and the effect of the following parameters by means of both experimental and computational wherever applicable:

- Geometry related parameters
    - Effect of impeller type
    - Effect of impeller speed
    - Effect of impeller clearance

- Phase physical property related parameters
    - Particle size effect
    - Particle specific gravity effect
    - Particle concentration

3 Experimental setup and procedure

3.1 Experimental setup

A flat-bottomed, cylindrical tank of 40 cm diameter (T) was chosen as the mixing vessel equipped with four baffles. Baffles had a width (B) of 3.4 cm and a clearance of 8 mm to the tank wall to avoid dead zones ($B = T/12$ and clearance of $T/50$ to the tank wall). There were eight planes at which the measurement were taken. The bottom plane was spaced 4.25 from the bottom of the tank and the rest of planes were vertically spaced by 4.25 cm accordingly. The bottom plane was named plane one and subsequent planes were named accordingly. Each plane consisted of 16 electrodes installed on the tank periphery. Electrodes were all identical and made of stainless steel with the size of 20 × 30 × 1 mm. There was a single ground electrode, located between planes four and five, based on which the reference was taken. The setup was also equipped with a spiral spring torque meter (Staiger Mohilo, Germany), a data acquisition system (DAS) (Industrial Tomography Systems 2000, UK) and a computer (Pentium IV, CPU 2 GH, 512 MB RAM) as shown in Figure 3.1. The schematic diagram of the setup is illustrated in Figure 3.2.

3.1.1 Impeller Specifications

In this study, four axial flow impellers, each with a 17.8 cm diameter, were employed. A310, a hydrofoil impeller, was used as the main impeller and the A200 (equivalent to pitched blade turbin), A100 (equivalent to a marine propeller) and A320 Lightning impellers were also employed (Table 3.1). Clearance between impeller and tank bottom was selected upon the test condition between T/5 to T/2.

Table 3.1 Impeller specifications (Paul et al., 2004)

Impeller type	Number of blades/Blade degree/diameter	Specifications
A310/Hydrofoil	3/45° and twisted/17.8 *cm*	The blades are tapered more on width from impeller hub to blades tip. Blade tip in these impellers eliminate any tendency for the flow to re-circulate around the tips, producing a uniform velocity across the entire discharge area. While A310 is recommended for low-viscosity flow-controlled applications
A200 or pitched blade turbine	4/45°/17.8 *cm*	Pitched blade turbine produce an axial flow pattern with a balance between shear and pumping. Standard A200 impellers consist of four blades welded on a central hub at a 45° pitch. A200 impellers are recommended for low- to medium-viscosity, flow-controlled applications
A100 or marine propeller	3/45°rounded and twisted/17.8 *cm*	A100 produce a downward axial flow towards the bottom of the tank, and are most effective in low viscosity applications requiring moderate pumping (McDonough, 1992). A100 impellers are characterized by high discharge capacity with low head. The twisted skewness of the blades creates a constant blade pitch. A100 impeller used in this experimental work has a square pitch
A320/Hydrofoil	3/45° and twisted/17.8 *cm*	A320 is considered as a high efficient impeller such as A310 but is advised for higher-viscosity applications requiring high flow

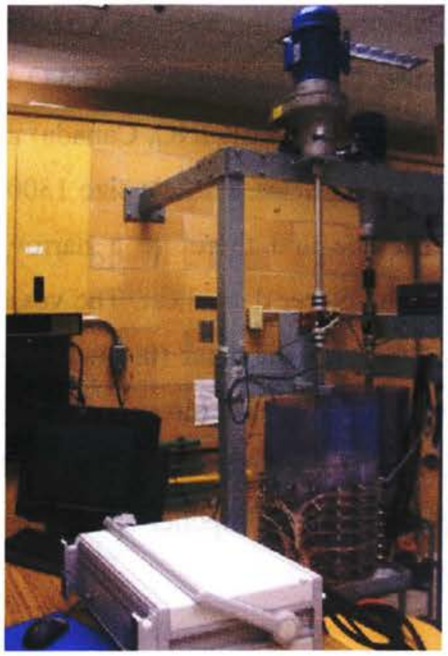

Figure 3.1 Experimental setup picture (left to right: computer, DAS, Vessel)

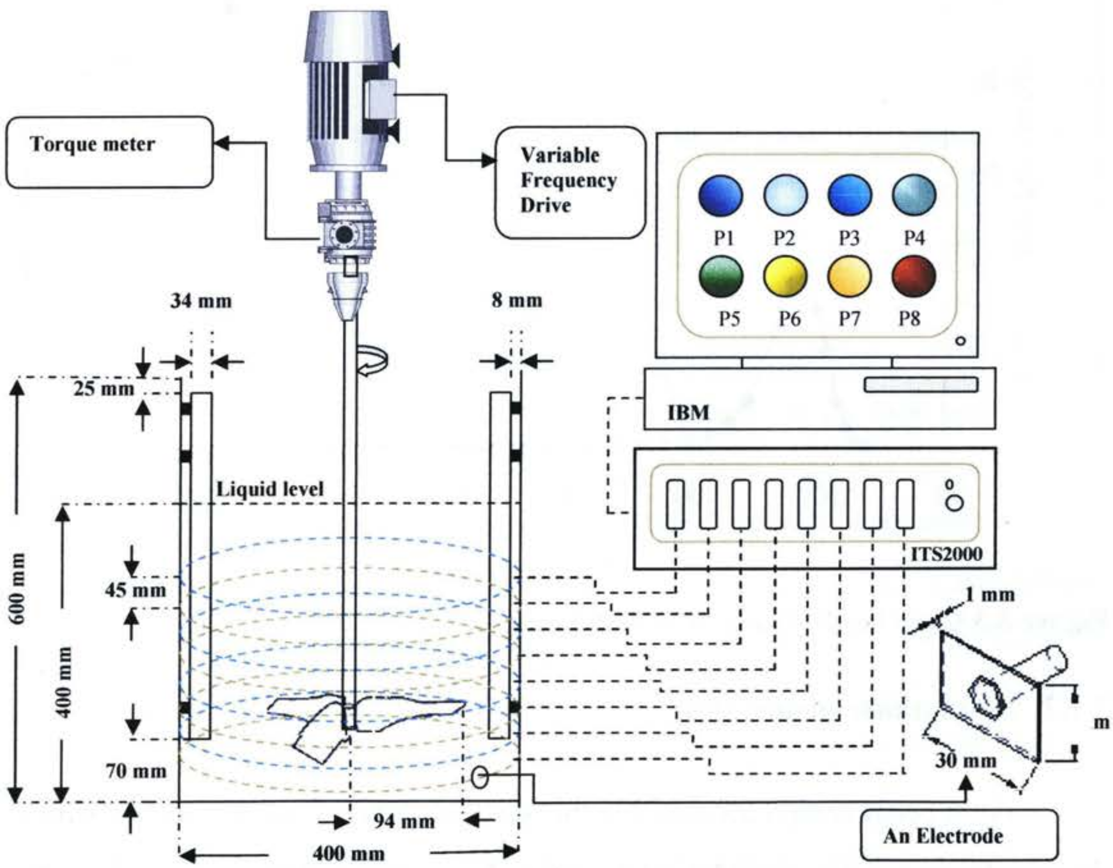

Figure 3.2 Experimental setup schematic diagram used in this study

In this study, tap water was used as the medium. Glass beads with a nominal average of 210 μm (Potters Industries, USA), 550 μm (FLEX-O-LITE, Canada) as confirmed in Figure 3.3 (Microtrac S3500,BETATEK.INC, Canada) and 1500 μm (Potters Industries, USA) were used as the solid particles. Particle size 1500 μm was out of the range of the particle size analyzer machine and therefore a narrow particle size distribution was assumed based on the manufacturer data sheet. The vessel was filled with tap water to a height (*H*) equivalent of the tank diameter (0.4 m). The conductivity of the water was measured using a conductivity meter (around 330 $\mu S/cm$ measured by OAKTON conductivity meter, EUTECH Instrument, Germany) which was kept constant for the medium during the experiment. The impeller speed was set to the desired rpm using a variable frequency drive.

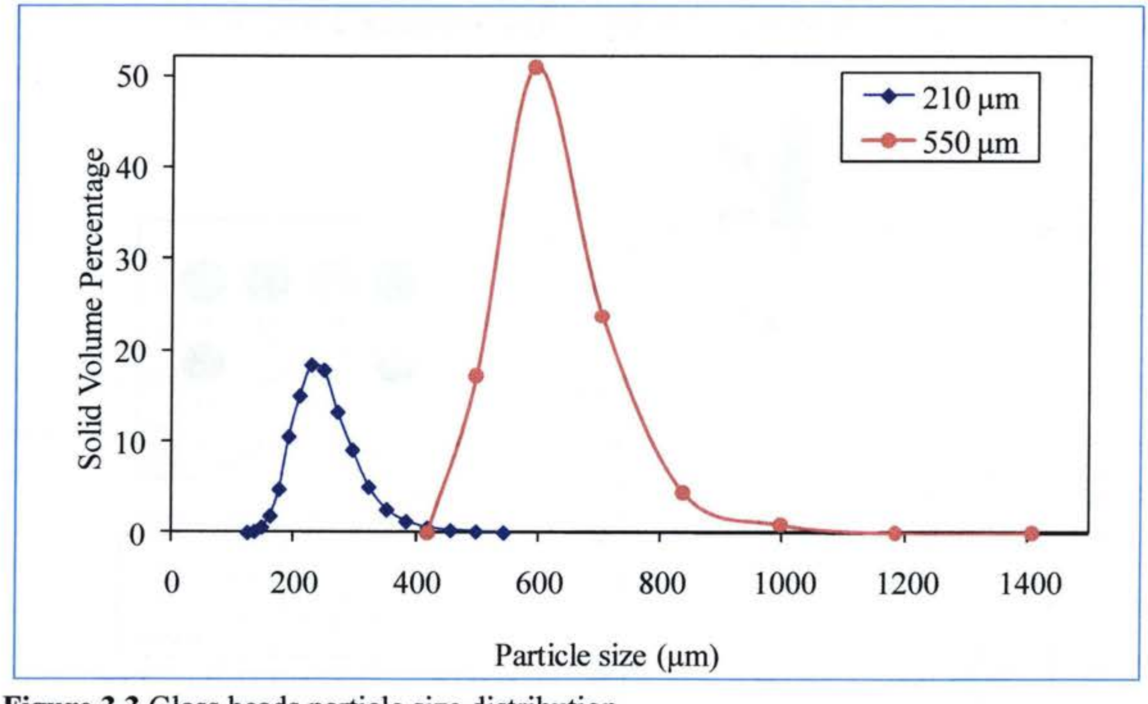

Figure 3.3 Glass beads particle size distribution

3.1.2 Solid phase properties

Glass beads composition used in this study was Soda-Lime Silica glass with a density of 2.5 g/cc. The crush resistance and refractive index of the glass beads were claimed by manufacturer to be 14000-36000 psi and 1.51-1.52 respectively. All three sizes of the glass beads were 90% round and fairly close to spherical shape. The information needed for this study can be found in Table 3.2.

Table 3.2 Particles specifications

Particle type	Shape/nominal average size	Specific gravity	Packing factor	Manufacturer/code
Glass beads	Spherical/210 μm	2.5	0.65	Potters.inc/P-0100
Glass beads	Spherical/550 μm	2.5	0.6	FLEX-O-LITE/BT-4
Glass beads	Spherical/1500 μm	2.5	0.55	Potters.inc/Premium 1.5 mm

3.1.3 Experimental runs and conditions

Based on the literature review a range of experimental conditions were assigned to each variable. The impeller type was limited to those axial flow makers such as propellers which were mounted on the shaft at different clearance depending upon the test condition. Impeller speed was limited between the just-suspended impeller speed and the maximum impeller speed possible at which no air entertainment involved. The just-suspended impeller speed was calculated based on the correlation offered in literature and confirmed visually. The design of the baffles with a clearance to the tank wall and tank bottom caused better circulation of the fluid with no dead zone and predicting just-suspended impeller speed visually would not be tricky. The tests were covering small particle size 210 μm to big particle size such as 1500 μm. A narrow particle size selected for the effect of particle size on solid-liquid mixing behavior and a wide range of particle size distribution was not considered due to the complexity of the results to the particle size. The concentration of solid was chosen from a dilute concentration 2 wt% to a high concentration 30 wt%. Most of the previous researches were conducted within the range of concentration chosen for this study. Details about the experimental runs and condition can be found in Table 3.3.

Table 3.3 Experimental runs and conditions

Effecting variable/fixed conditions **Run**	**1**	**2**	**3**	**4**	**5**	**6**	**7**	**8**	**9**	**10**	**11**
Impeller speed ***N (rpm)***	250	280	300	320	350	400	450	500	600	700	80
Impeller type/all N, $C=T/3, d_p=210\ \mu m, X=10$ *wt%*	A100	A200	A310	A320							
Impeller clearance (*C*)/ A310, all N, $d_p=210\ \mu m$, $X=10$ *wt%*	$T/5$	$T/3$	$T/2$								
Particle size (d_p)/ A310, all N, $C=T/3$, $X=10$ *wt%*	210 μm	550 μm	1500 μm								
Solid concentration (*X*)/ A310, all N, $C=T/3, d_p=210\ \mu m$,	2 wt%	5 wt%	20 wt%	30 wt%							

3.2 Electrical Resistance Tomography

Electrical resistance tomography is based on the conductivity difference between the phases. It is applicable to all systems in which the medium is conductive. Any changes in the conductivity of the continuum phase can be detected by ERT. Industrial Tomography System (ITS) consists of sensing parts, Data Acquisition System (DAS) and a software installed on a computer to process all the commands and protocols. The sensors are made of stainless steel with a size proportional to the setup and are mounted around the periphery of the vessel. Electrodes are connected to an intermediate machine called Data Acquisition System through coaxial cables.

A Data Acquisition System (DAS) is responsible for applying the current and measuring the voltages based on the desired protocol. Four main strategies for voltage measurement can be assigned to DAS: adjacent strategy, opposite strategy, diagonal or cross strategy and conducting boundary strategy. Among these four strategies, adjacent strategy demands less hardware and provides fast image reconstruction which can be achieved through 104 voltage measurements for a plane with 16 electrodes according to Equation (3.1). Hence, adjacent strategy was assigned to DAS as the measurement protocol. Adjacent strategy applies current through two adjacent electrode and measures the voltages of the subsequent neighboring pair of electrodes along the circumference and then it will be switched to the next pair of electrodes and repeated until all independent measurement have been completed as in Equation **(3.1)** (Dobaie, 1995; Dickin, 1996; Hua et al., 1993; Loh et al., 1998):

$$M_e = \frac{n_e\left(n_e - 3\right)}{2} \tag{3.1}$$

where M_e is the number of ERT measurements and n_e is the number of electrodes.

The next step subsequent to voltage measurement would be image reconstruction. In order to obtain the conductivity distribution, the area of the interest is usually gridded spatially to equal squares (20 × 20) which only 316 of them will fit in the boundary of a cylindrical tank. The Poisson's equation can be defined to find the conductivity of each individual pixel (Madupu et al., 2005):

$$\nabla . R^{-1} \nabla V = 0 \tag{3.2}$$

with boundary conditions of: V=V_o and $R^{-1}\dfrac{\partial V}{\partial n} = J_0$ on ΔA where A is the region of interest ,R is the resistivity in ohm and V_o and J_0 are the voltage in volt and current densities at the boundary region (applied or measured by ERT). To solve Poisson's equation over the entire area, a numerical method would be essential as the exact solution is not possible. Sensitivity conjugate gradient, SCG, as an iterative method (Wang, 2002) and linear back projection algorithm as a non-iterative method (Madupu et al., 2005) are applicable to approach the approximate solution. Linear back projection was employed in this study for its simplicity and low computational CPU time. The calculated cell conductivity was then converted to solid concentration through Maxwell's equation (1873) (ITS, 2005):

$$X_V = \frac{2\sigma_l + \sigma_s - 2\sigma_{mc} - \left(\frac{\sigma_{mc}\sigma_s}{\sigma_l}\right)}{\sigma_{mc} - \left(\frac{\sigma_s}{\sigma_l}\right)\sigma_{mc} + 2(\sigma_l - \sigma_s)} \tag{3.3}$$

where X_V, σ_l, σ_s and σ_{mc} are the volume fraction of the dispersed materials, the conductivity of the continuous phase (*μS/cm*), the conductivity of the dispersed phase (*μS/cm*) and the reconstructed measured conductivity (*μS/cm*) respectively. σ_l was measured by conductivity meter and was varied between 300-335 μS/cm and σ_s was considered zero during the experiments.

3.2.1 Material preparation

Tap water with the conductivity between 300-335 μS/cm was used as medium. This conductivity was measured and recorded for further reference and also to eliminate any factor which might affect the initial conductivity such as temperature. Physical quantity of electrical conductivity gets affected by temperature difference linearly with a slop of about two if the temperature unit is encountered in Centigrade (Grellier et al. 2006). Since all the experiments were conducted in room temperature, the vessel was filled up with tap water and left over night to minimize temperature influence. Glass beads, as the solid phase, were washed thoroughly with de-ionized water after each experiment to ensure their conductivity did not get affected by tap water. Subsequently, they were dried out either in room temperature or in a pilot tray dryer. Glass beads were kept in room temperature at least over one night to ensure that the temperature would not be a factor when conducting an experiment. As precaution, the conductivity and temperature were measured before starting the experiment, after adding glass beads and at the end of the experiment. In the case of any conductivity changes after solid addition, the conductivity was adjusted either by de-ionized water or brine. All experiments were replicated three times. In other words, each case was tested four times, twice with online references and twice with saved references. Identical results were obtained virtually in online reference results and the relevant saved reference results. The error involved with two online reference results was less than one percent in most of the cases since all the measurements were time averaged over a time period as shown in Figure 3.4.

3.2.2 Tomography measuring steps

Tomography measurement requires a reference to compare the measurement with, since it is based on the conductivity reference. Taking the reference is the trickiest part of experiment since the geometry effect on conductivity is taken into consideration. In other words, baffles, tank bottom, impeller and shaft are fixed during the operation. Any change in the geometry during the course of an experiment renders the measurement inapplicable. Tank bottom and liquid level are usually subjected to change when second phase is introduced to the continuum. In cases, such as adding solid particles, the liquid level has to be adjusted to the initial point. The solid particles should not be left idle either at the bottom if they are sinking particles or at the level if they are buoyant particles.

The injection current and gain map of the tomography machine were calibrated by Industrial Tomography System (ITS) software. An online reference for the conductivity was taken (and saved for future usage) accordingly to eliminate any geometrical effect on the electrical field. The solid was meticulously weighed as the desired weight fraction. In this study, the level was adjusted by scooping the excess water out. The excess water was measured to the equivalent of the solid volume. The ERT measurement and the impeller speed had started before water was scooped out; subsequently the solid was added.

3.2.3 ERT data post processing

Figure 3.4 shows a raw data sample taken by ERT. In this figure the first 50 frames refer to the reference and clearly showed same conductivity for all the planes. The distraction of the conductivity from frame 50 to 175 was caused by scooping the water out of the tank. Glass beads were added at or about frame 175. The resulting data were then time-averaged before any other calculations (frames 225-325).

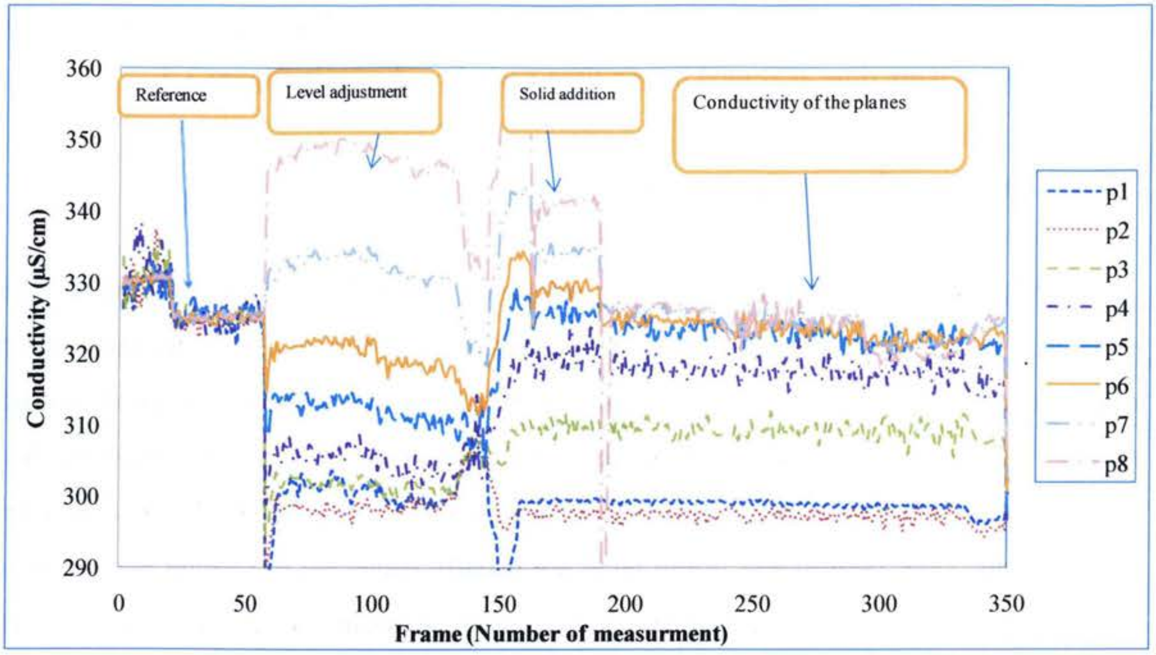

Figure 3.4 A sample of raw data by ERT for all planes (p1 was the bottom plane), A310, $C = T/2, N = 350rpm, X = 30wt\%, d_p = 210\mu m$

Once the ERT data are reconstructed, it is possible to obtain the tomograms as well. Tomograms are typically used in online process monitoring. They are basically a two dimensional scan of the system. Figure 3.5 shows a sample of tomogram of solid suspension with low impeller speed $(N = 250rpm)$, below N_{js}, in which there is a portion of blue color. Glass beads are virtually non-conductive and wherever their concentration is high tomogram's color is pushed towards the low conductivity color. As the impeller speed increases more solid particles are suspended in the upper part of the tank and at some point it reaches its maximum homogeneity (Figure 3.6). It is worthwhile to mention that tomograms are generated immediately after each measurement and could be used for qualitative comparison.

The error incorporated with ERT results laid between 0.1% to 3%, based on the ITS software analysis. ITS software calculates the standard deviation of the conductivity measurements in each plane and reports them simultaneously with tomograms.

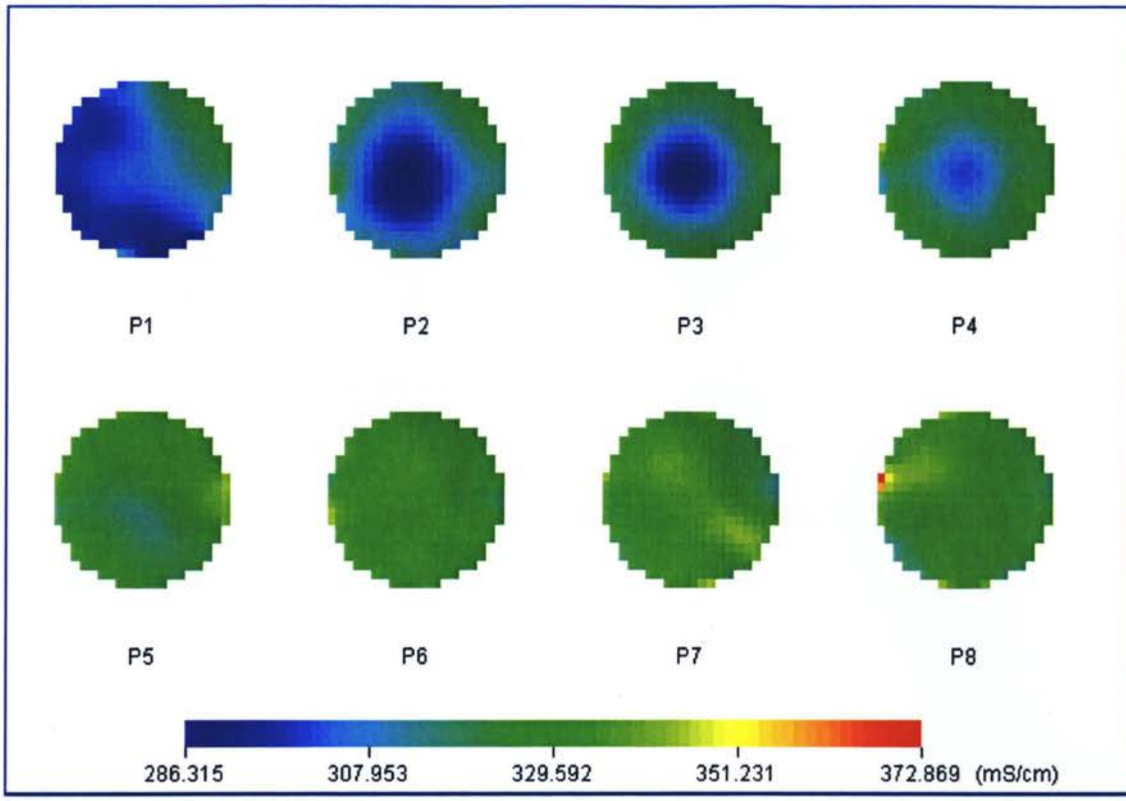

Figure 3.5 Conductivity tomograms throughout the vessel, PBT impeller and glass beads as the solid phase, $C = T / 2, N = 250\text{rpm}, X = 10\text{wt\%}, \text{d}_\text{p} = 210\mu\text{m}$

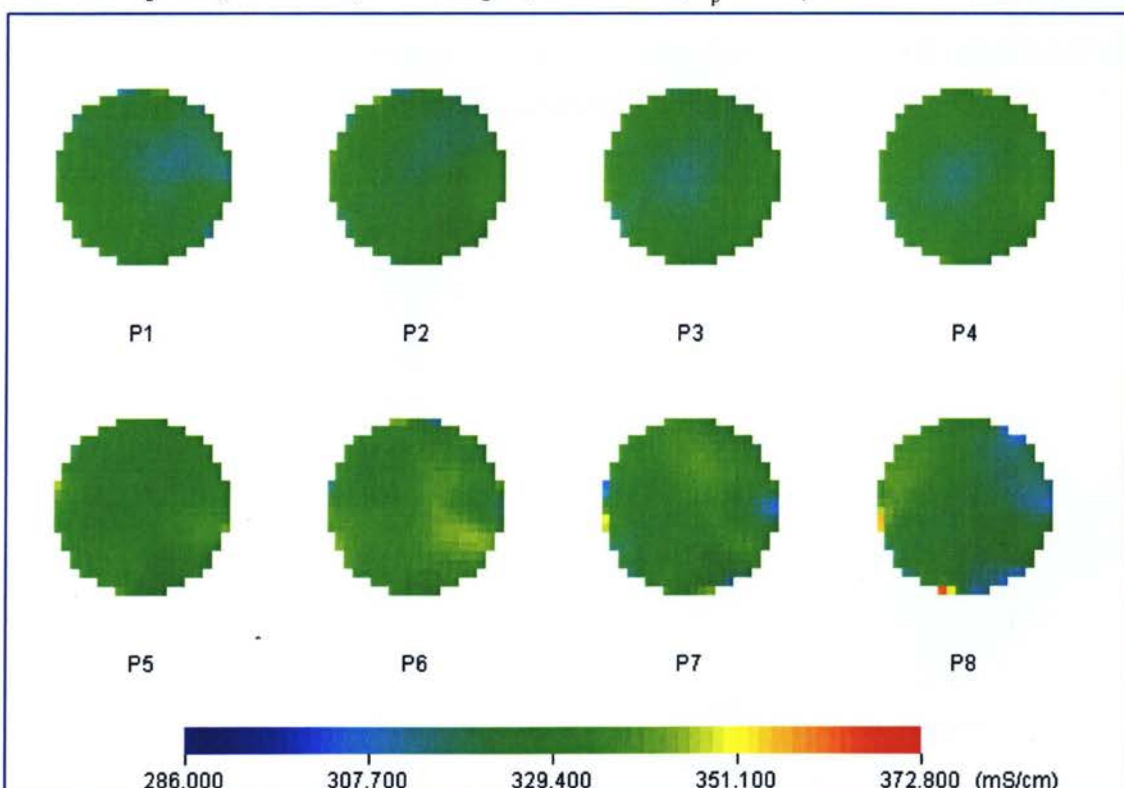

Figure 3.6 Conductivity tomograms throughout the vessel, PBT impeller and glass beads as the solid phase, $C = T / 2, N = 500\text{rpm}, X = 10\text{wt\%}, \text{d}_\text{p} = 210\mu\text{m}$

4 Computational fluid dynamics

4.1 Governing equations

Applying conservation of laws for mass and momentum in this study , for two phase flow, results in:

Continuity equation (Fluent Inc., 2006):

$$\frac{\partial(a_k\rho_k)}{\partial t}+\nabla.\left(a_k\rho_k\overrightarrow{u_k}\right)=0 \tag{4.1}$$

and since the drag force is dominant compared to other forces present, all other forces are negligible and therefore the momentum equation is as follows (Fluent Inc., 2006):

$$\begin{aligned}&\frac{\partial}{\partial t}\left(a_k\rho_k\overrightarrow{u_k}\right)+\nabla.\left(a_k\rho_k\overrightarrow{u_k}\overrightarrow{u_k}\right)=\\&-a_k\nabla p+\nabla.\left(\overline{\overline{\tau_k}}\right)+a_k\rho_k g+(\vec{F}_D)\end{aligned} \tag{4.2}$$

where $\overline{\overline{\tau_k}}$ is the kth phase stress-strain tensor:

$$\overline{\overline{\tau_k}}=\alpha_k\left(\mu_k+\mu_{kt}\right)\left(\nabla\overrightarrow{u_k}+\nabla\overrightarrow{u_k}^T\right)-\frac{2}{3}\alpha_k\rho_k k_k\overline{\overline{I}} \tag{4.3}$$

here subscript k symbolizes phase k, and μ_k, μ_{kt} , K_k $\vec{F}_D$, are the shear viscosity, turbulent viscosity, turbulent kinetic energy, and drag force respectively. Drag force can be defined for two phases as $\vec{F}_D=\vec{F}_{lp}$ and Equation (2.47) is applicable for drag force in conjunction with Equation (2.54) and Equation (2.55) for the drag coefficient which was used in this study. Equations (2.63), (2.64), (2.65), and (2.66) have been employed in this study to model the turbulent flow.

4.2 Specifying mixing vessel in CFD

The computational model requires the domain of interest to be specified. In other words, the computational domain is bounded to the geometry. Subsequently the domain is divided to small sub-domain cells. Geometry specifies the entire components which are involved within the volume of interest such as baffles, spargers, impeller, shaft, coils and draft tubes. No matter how complex the geometry and all internals, are the computational grid must fit the contours of the vessel and internals (Fluent, 2006). For simplicity, some internals can be set as zero thickness if their effect to the system is not dramatized. This action reduces the number of sub-domain and consequently less computational time is required. Baffles and impeller blade thickness are some examples of zero-thickness. The system geometry in computational domain was defined by employing Gambit softwar version 2.4 and Mixsim software version 2.6 commercial software.

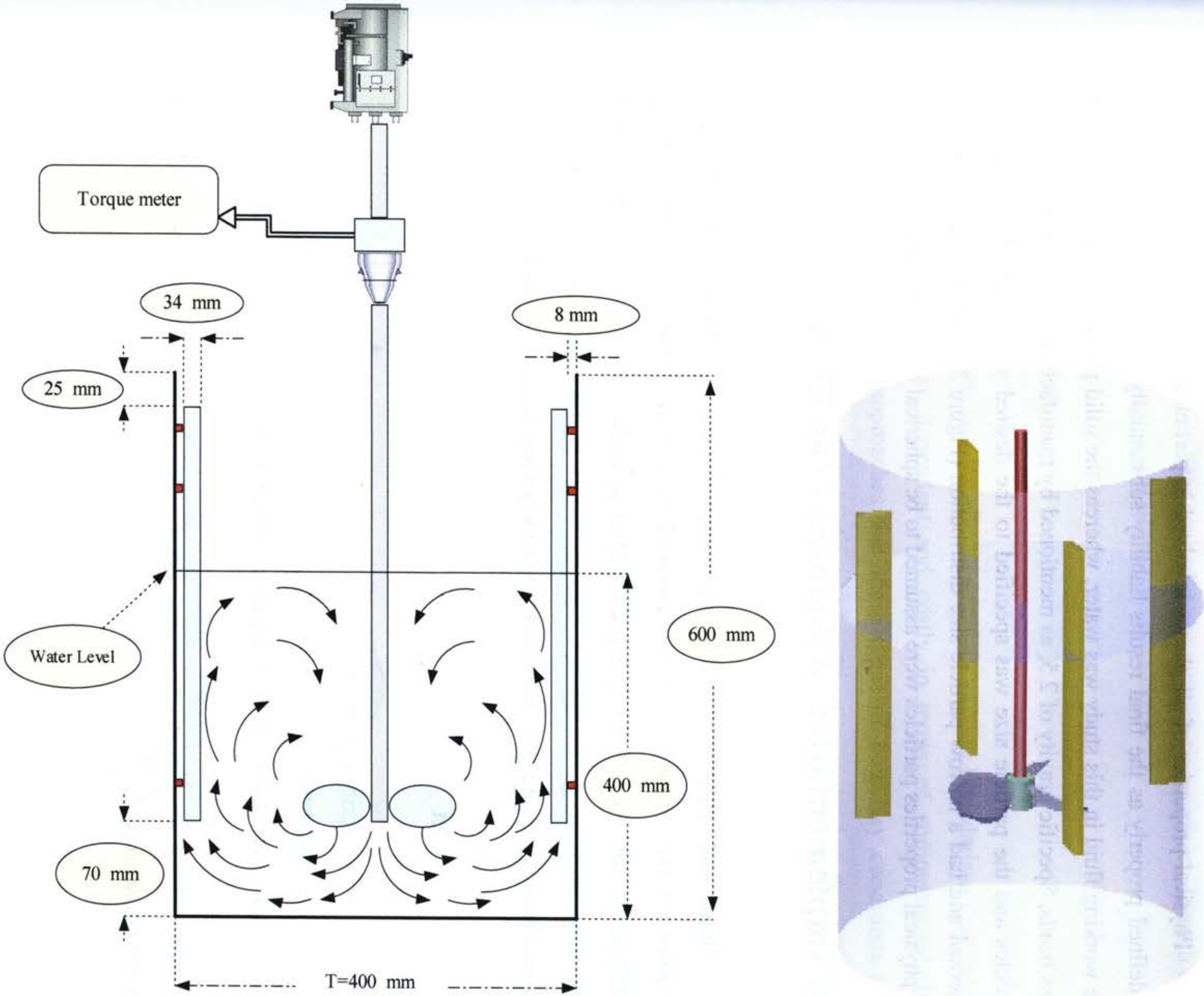

Figure 4.1 Schematic diagram of the tank with the flow pattern of an axial impeller

4.3 Specifying material physical properties

Physical properties of all phases involved in partial differential equations should be defined properly as the final results liability substantially relies on these properties. The working fluid in this study was water, whereas the solid phase had the properties of glass beads. Specific gravity of 2.5, as mentioned by manufacturer, was applied for solid particles and the particle size was specified to the desired value. Particles were 90% spherical and had a narrow particle size distribution (Figure 3.3). However, in applying the physical properties particles were assumed to be spherical and mono-size.

4.4 Implementation of boundary conditions

Initial and boundary conditions are incorporated with all CFD problems. The flow variables on the boundaries of the physical model are known as CFD boundary conditions (Fluent Inc, 2006). It is important to understand and specify them correctly since they force the governing equations to follow problem specifications. The most common boundary conditions are listed below (Versteeg, & Malalasekera, 2007):

- inlet
- outlet
- wall
- prescribed pressure
- symmetry
- periodicity (or cyclic boundary condition)

Geometry related boundaries can be also classified to two main categories: stationary and moving boundaries.

4.4.1 Stationary boundaries

Typical stationary boundaries are such as wall and baffles in mixing tanks on which no-slip boundary conditions are applied to the representing surfaces. In such cases, all components of velocity are equated to zero.

4.4.2 Moving boundaries

Reciprocating pistons and impellers exemplify moving boundaries. This type of boundary condition is time dependent and costly in terms of computational time. However, there are some approaches that these types of boundary conditions (with certain restrictions) are applied in a steady state condition in contrast to those that treat them literally in the time dependent manner.

4.4.3 Rotating reference frame model

In this approach, the momentum equations are solved in a rotating frame for the entire domain. In other words, the frame is considered stationary but inertial. Therefore, additional acceleration terms incorporate the equations of motion due to transformation of stationary frame to rotating reference frame. Hence, the equations of motion turn to:

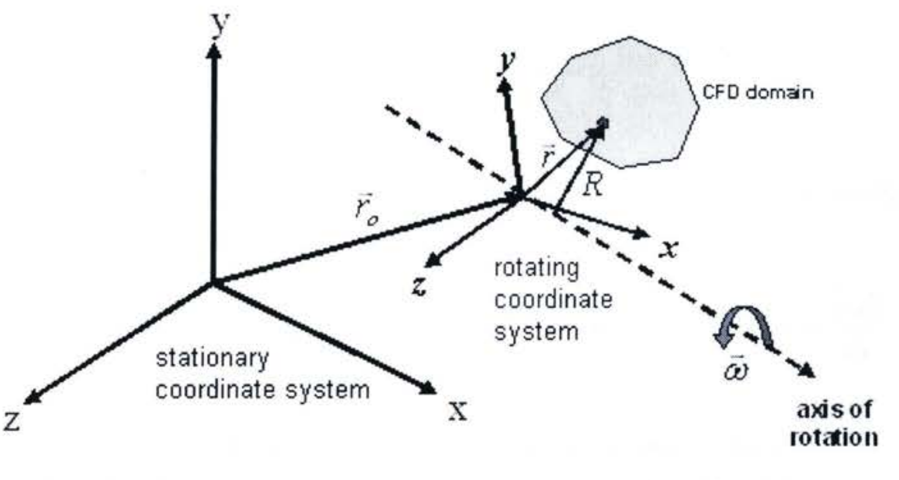

Figure 4.2 Rotating frame reference with an angular velocity of ω (Fluent Inc, 2006)

Considering the CFD domain is rotating around an axis with unit vector of $\vec{a}$ and an angular velocity magnitude of ω , the rotation vector is defined as:

$$\vec{\omega}=\omega\vec{a} \tag{4.4}$$

Arbitrary points in CFD domain are located by $\vec{r}$ and the augmented governing equations based on the absolute velocities can be reconstructed using the following fluid velocities:

$$\vec{u_r}=\vec{u}-\vec{u_{wr}} \tag{4.5}$$

where

$$\vec{u_{wr}}=\vec{\omega}\times\vec{r} \tag{4.6}$$

In the above, $\vec{u_r}$ is the relative velocity (the velocity viewed from the rotating frame), $\vec{u}$ is the absolute velocity (the velocity viewed from the stationary frame), and $\vec{u_{wr}}$ is the "whirl" velocity (the velocity due to the moving frame).

Continuity equation for the rotating frame:

$$\frac{\partial\rho}{\partial t}=-\left(\nabla.\rho\vec{u_r}\right) \tag{4.7}$$

Momentum equation for the rotating frame:

$$\frac{\partial\rho\vec{u}}{\partial t}=-\left(\nabla.\rho\vec{u_r}\vec{u}\right)-\rho\left(\vec{\omega}\times\vec{u}\right)-\nabla p-\left(\nabla\bar{\bar{\tau}}\right)+\rho\vec{g}+\vec{F} \tag{4.8}$$

where the Coriolis and centripetal accelerations are considered in $\left(\vec{\omega}\times\vec{u}\right)$ term. This approach well performs for mixing tanks with no baffles (Fluent, 2006).

4.4.3.1 Multiple reference frames

Multiple reference frame model is an approach of rendering unsteady state problem in which there are multiple moving parts or stationary surfaces which are not surfaces of revolution a steady state manner (Fluent Inc, 2006). In such cases, the domain may be broken to multiple fluid/solid cell zones with interface boundaries separating the zones. Zones with moving parts are treated with moving reference frame equations, whereas stationary zones are supported with stationary equations. Figure 4.3 shows how a pitched blade turbine motion is modeled through MRF in a mixing tank while due to the symmetrical geometry; periodic boundary condition is applied to the sides of the slice. At the interface of zones, the velocities are forced to match. If the absolute velocity formulation is used, sub-domains are treated with the corresponding sub-domain reference frame; however the velocities are stored in the absolute frame. Thereby, no special transformation for velocities at the interface is required and scalar quantities can be obtained from the adjacent cells.

MRF model is applicable to all the cases in which the rotor-stator interaction is relatively weak. In other word, the model cannot predict mixing vessels with large impeller diameter compared to the vessel diameter such helical ribbon or anchor impellers. MRF has also uniform flow assumption at the boundaries. In the case of high non-uniformity MRF may not predict a reasonable solution. In such circumstances, the flow field data at the passing boundaries are spatially averaged (mixing plane) to achieve physically meaningful results (Fluent Inc, 2006). In this study MRF with absolute velocity was applied to all cases.

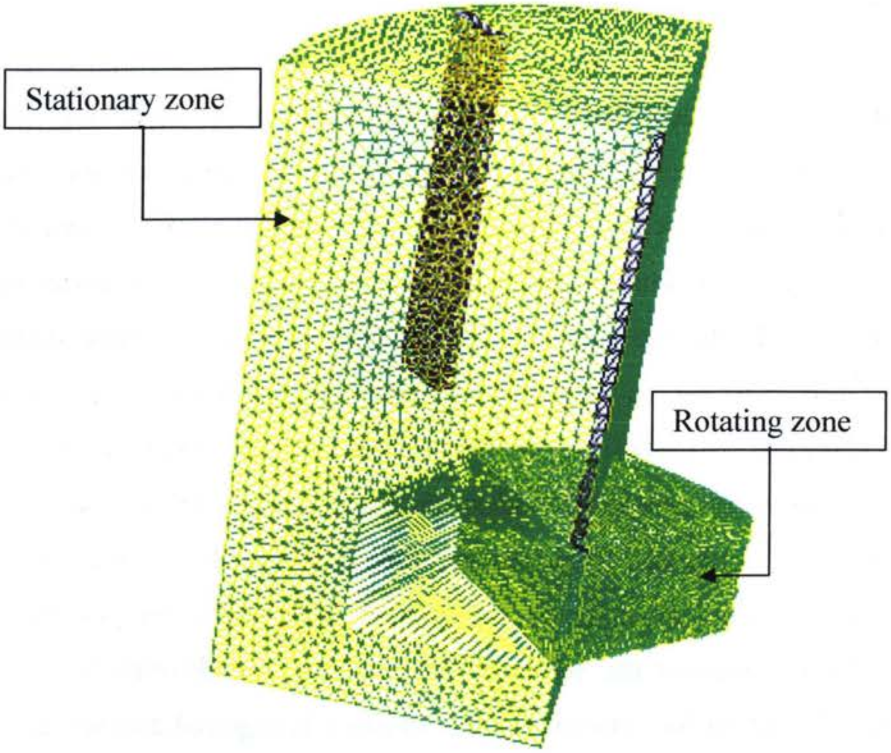

Figure 4.3 Multiple cell zones to mimic the impeller motion in a quarter of baffled mixing tank

4.4.3.2 Sliding mesh model

When rotor-stator interaction is strong, the better alternative to MRF would be sliding mesh. The model allows each frame zone cell to slide and adjust to the relative adjacent zone cell. Obviously, a cell interface is needed for each cell zone where it meets the opposing cell zone. In each time step, the cell zone slides relative to one another along the cell interface and the calculations is carried out based on the new position and a stationary frame. This model is a perfect match wherever the time-accurate solution is desired (Fluent Inc, 2006).

4.5 Grid generation

In order to break the computational domain to sub-domains, grids or meshes can be used. A mesh can be generated with different shapes and sizes. Shape matters when it comes to separating the domain to sub-domains for parallel processing and size pops up when it comes to sharp gradient of an entity. Shapes such as triangle and quad can be used for 2D analysis and tetrahedron, hexahedron, prism/wedge and pyramid are employed for 3D analysis.

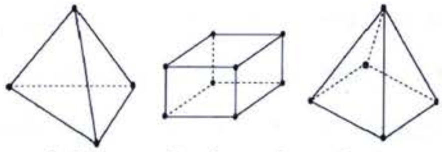

Figure 4.4 3D cell types, left to right: tetrahedron, hexahedron and pyramid (Paul et al. 2004)

The factor of skewness indicates how much error can be involved with calculation for a single cell. The limits of skewness are zero as no-skewness to one as the maximum.

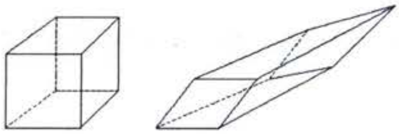

Figure 4.5 Elements with different skewness, left to right: low and high skew (Fluent, 2006)

The resulting computational error with skewness factor above 0.6 is drastic and should be avoided. A combination of number of grids and skewness factor is the indication of the computational error. In other words, smaller grid size can compensate some error caused by skewness; however it is at the expense of more computational time (Fluent Inc., 2006).

In this study, tetrahedron grid type was used because of the compatibility of this type with parallel CPU and the skewness of the grid was kept below 0.6. Grid generation was done by Gambit. It generates different types of grids depending upon the system geometry. The size of the grids is the most important key in computational error involved with the result.

4.5.1 Grid dependency

Mesh independency was conducted to optimize the effect of the grid size. The finer the mesh, the better results will be achieved. However, it has to be compromised with regards to CPU time and error tolerance. The discrepancy between with 307,757 numbers of cells and 819,677 number of cells was less than 2.3% both in velocity and kinetic energy profiles. Whereas the error involve with other cases with less cell number compared to 819,677 was more than 4%. The CPU time to run a case with 307,757 cells and a CPU speed of 3 GHz was five days if the time step had been set to 0.01 seconds. Since the CPU time was almost half of the time required to run the case with 819,677 cells number as a compromise this mesh density was chosen to be applied for all the cases. The effect of the fine and coarse mesh is depicted in Figure 4.6 and Figure 4.7 which are the axial velocity profiles with different mesh in half a tank (R is the tank radious).

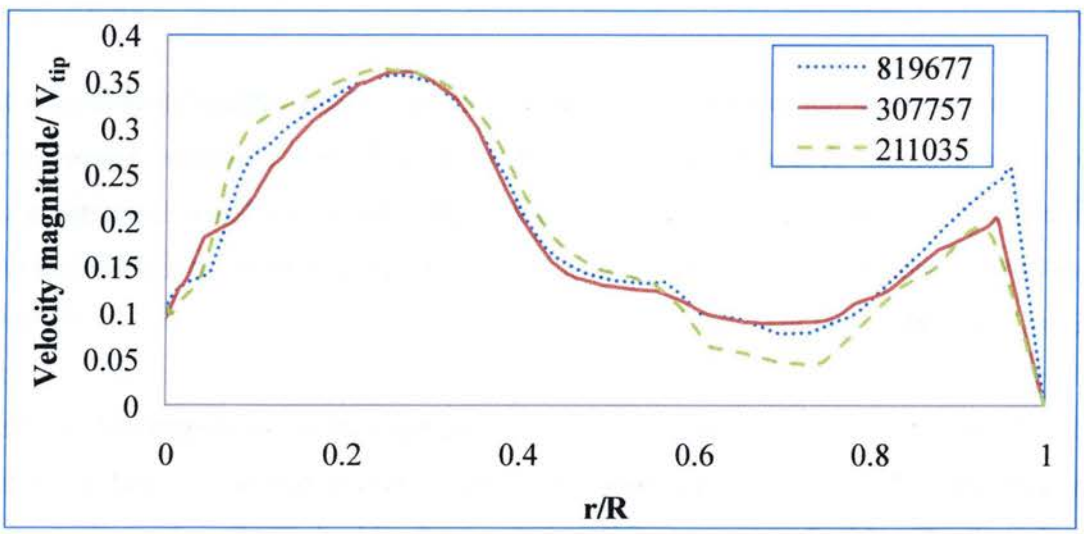

Figure 4.6: Mesh independency: Axial velocity profile at 1 *cm* below the impeller, A310, $N = 400rpm, C = T/3, X = 10\ wt\%, d_p = 210\mu m,\ SG = 2.5$

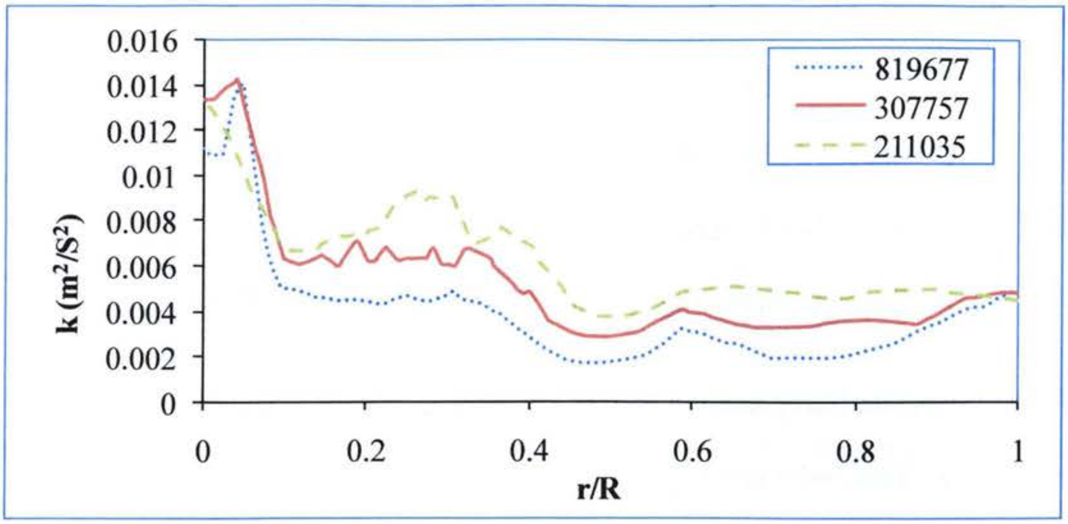

Figure 4.7: Mesh independency: Kinetic energy profile at 1 *cm* below the impeller, A310, $N = 400rpm, C = T/3, X = 10\ wt\%, d_p = 210\mu m,\ SG = 2.5$

4.6 Discretization of partial differential equations

Once the cells are generated, an approximation of transport equations should be applied to the discrete sub-domains to calculate the change of an entity within the entire domain of interest. In other words, the differential equations are approximated both spatially and temporally. Finite volume method discretizes the differential equations based on truncated Taylor series spatially. Discretization scheme in CFD specifies the order of truncation in Taylor series (Leonard & Mokhtari, 1990 ;Patankar, 1980 ;Versteeg & Malalasekera, 2007). Other alternative methods for solving Navier-stokes equations could be finite difference and finite element methods (Paul et al., 2004).

Temporal discretization follows two major methods: explicit and implicit approach.

- Explicit approach evaluates the field in current time and is cheap numerically; however, it is instable and more likely to diverge.

- Implicit approach, on contrary, evaluates the field at different time level, but more robust in convergence (Blazek, 2005).

Pressure gradient may be predicted by different scheme:

- Linear scheme
- Standard (first order)
- Second order scheme
- Pressure staggering option, PRESTO ((Harlow & Welch, 1965)

Momentum interpolation schemes are divided to:

- First order upwind scheme
- Second order upwind scheme (Ranade, 2002)
- Quadratic upwind scheme (QUICK) (Leonard & Mokhtari, 1990)
- Power law (Patankar, 1980)

In this study, first order discretization scheme was initially chosen for spatial discretization to insure convergence; subsequently was switched to second order discretization scheme. Implicit scheme was also chosen to discretize the differential equations temporally.

4.7 Solution method of discretized equation

The result of discretization process is a set of non-linear algebraic equations which can be solved with two different approaches:

- Segregated solution approach in which each entity has to be solved for the entire domain at a time. For instance, the x-component of the velocity should be solved for the whole domain and subsequently, y-component and z-component

- Coupled solution approach, on the other hand, solves simultaneously all the variables in each cell.

The coupled solution approach, in comparison to segregated solution approach is more robust, but requires more computational memory (Paul et al., 2004). This study utilized coupled solution approach in order to minimize discrepancies and quicker convergence.

4.7.1 Pressure velocity coupling

For incompressible fluids which their solution are pressure based, in contrast to the density based, pressure-velocity is tricky. There are several algorithm offered in this regards which are named as:

- Semi-implicit method for pressure-linked equations (SIMPLE) (Patankar, 1980 ; Versteeg & Malalasekera, 2007)
- Semi-implicit method for pressure-linked equations consistent (SIMPLEC)
- Pressure implicit with splitting of operators (PSIO)

SIMPLE algorithm (Patankar, 1980) comes up in the absence of any explicit equation for pressure and works based a first guess for the pressure field. Subsequently the equations of motion are solved and checked the continuity equation satisfaction. The pressure field is corrected based on the continuity equation residual and it will be iterated until it satisfies the specified tolerance of residuals. In this study the SIMPLE algorithm was applied to all the cases of interest.

4.7.2 Residuals

If possibly the algebraic form of conservation equations were solvable exactly, there would be no residuals. Since the numerical solution starts with a guess, there is always residual and that is why it is solved in an iterative manner. The iteration process will stop once the residual tolerance is achieved. The residual tolerance depends on the application sensitivity and users desire. In this study, the tolerance criterion for all normalized residuals was set to drop below 1×10^{-3} with respect to the starting point.

Figure 4.8 shows a typical residual monitoring of this study that all parameters solution scaled residuals have been decreased by three digits.

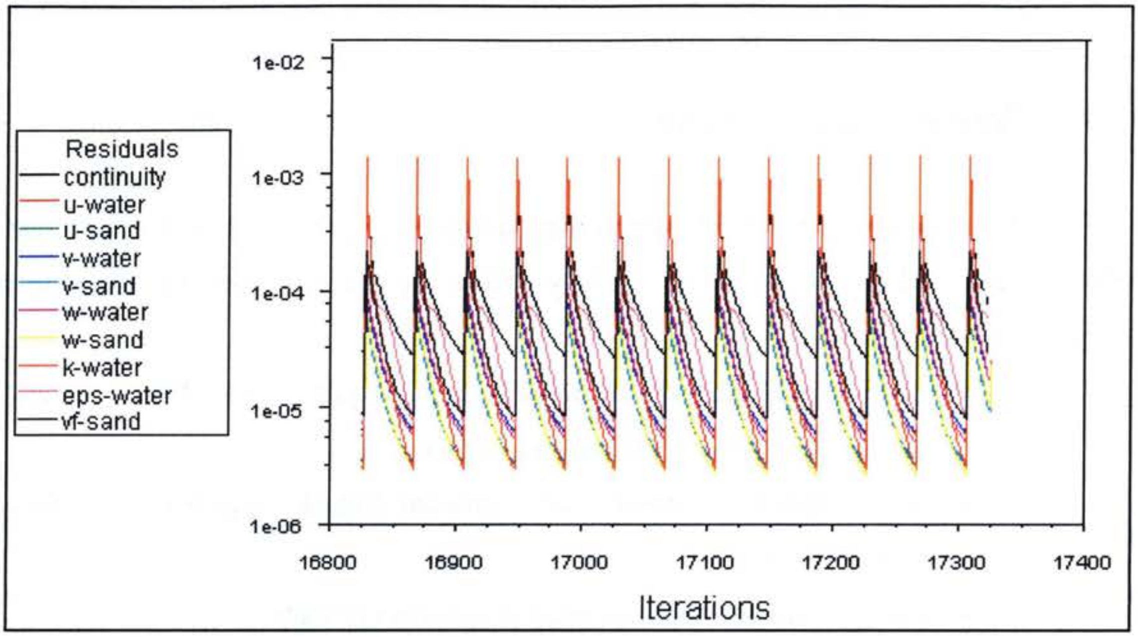

Figure 4.8 Typical scaled residuals for off-bottom glass bead suspension

4.7.3 Convergence criteria

Generally scaled residuals are used to judge the convergence. However, in cases such as multi-phase mixing other criteria such as local concentrations should be taken into consideration. This will ensure that convergence, specifically in unsteady state conditions, is not limited to some time steps and encountered for the whole time period of a process. Time step size can be also a factor in causing error and convergence. In Figure 4.9, time step size was set to one second while the time step in Figure 4.10 was chosen one mili-second. Convergence history of the cases shows smaller time step provided smoother results, but at the expense of triple computational time. In order to compromise the CPU time and accuracy of the results, step size of 0.001 second was assigned to all cases initially; subsequently switched to 0.01 second. It is worthwhile to mention that the time involved for convergence of the time step of 0.01 second was double than 1 second (compared to 0.001time step which was double than 0.01 second). It is simply because all assigned iterations in on time step have to be done in the early stages of solution due to the high residuals. Once the flow is solved and convergence is achieved in each time step and most of iteration (maximum iteration number per time step = 40) are skipped.

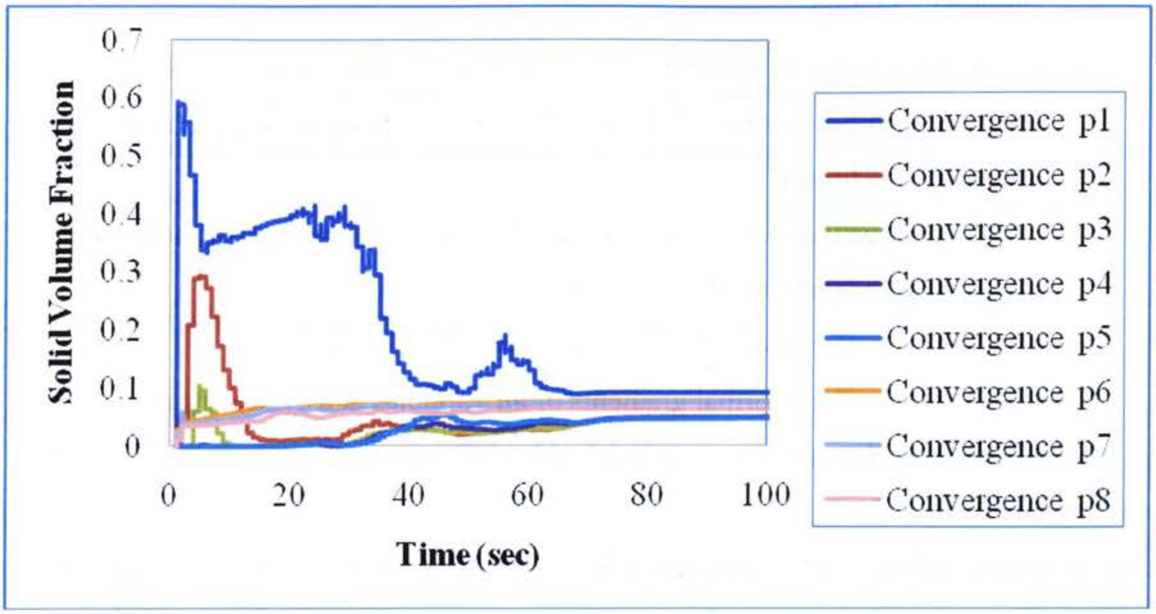

Figure 4.9 Convergence of different planes with time step of 1 second

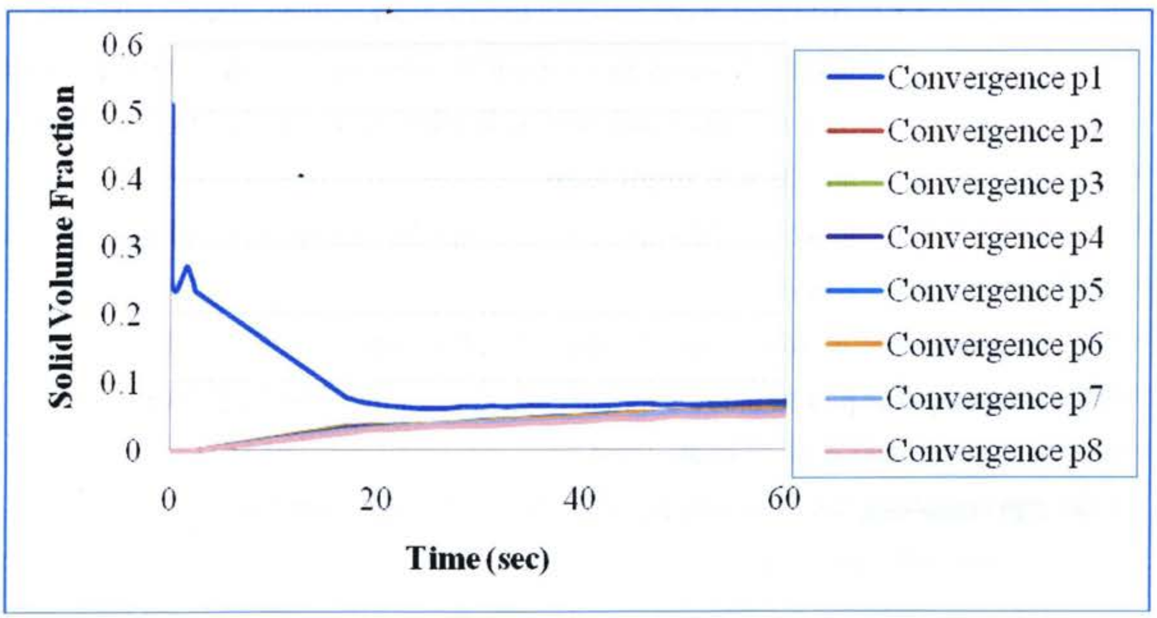

Figure 4.10 Convergence of different planes with time step of 0.001 second

4.8 CFD summary

- Model and grid were generated in Mixsim 2.1 and Gambit 2.4 (number of grids =300000 - 345000)
- Water was chosen as medium and properties of glass bead were applied as the solid phase, subsequently solid concentration was specified using Fluent 6.3
- Boundary conditions
    - Tank wall & baffles were assigned to no slip boundary for momentum
    - Liquid level was treated with:
        - Zero normal velocity at a symmetry plane
        - Zero normal gradients of all variables at a symmetry plane
    - Impeller motion was mimicked by MRF approach
- Solution method
    - Eulerian-Eulerian approach was chosen to derive conservation equations for both solid and liquid phases
    - Discretization
        - All cases were assigned to first order upwind scheme with low under-relaxation factor initially, subsequently (after 100 time step) the momentum and volume fraction were switched to second order and QUICK respectively
        - kinetic and dissipation were kept the same as first order due to hard convergence
- Pressure-velocity were coupled using SIMPLE algorithm
- Time step was picked 0.001 S initially and afterwards switched to 0.01 S and number of time steps = 4000 - 8000
- CPU time was 3-5 days with Pentium IV, 3.0 GH and 2 GB Memory

5 Results and discussion

In this chapter, both experimental and CFD results are presented comparatively where appropriate. It starts with validation of CFD model qualitatively and quantitatively and will be followed by a discussion on the results of experimental part.

5.1 CFD model qualitative validation

In an attempt to study the ability of the CFD model to predict flow behavior, a low impeller speed (below N_{js}) was applied to a stirred tank agitated by a pitched blade turbine (PBT) impeller. Figure 5.1 shows the contours of solid concentration in the tank computed using CFD. This figure shows a high concentration of solids accumulating in the center of the tank with somewhat lower concentrations at the periphery. These results are in good agreement with the experimental results obtained from ERT seen in Figure 5.2.

The accumulation of solids below the impeller is expected for radial impellers, or for axial impellers with upward-pumping flow behavior. In contrast, axial impellers with downward-pumping begin to dig a cavity in the solid particles idle on the tank bottom when the impeller speed is low due to the flow pattern generation. Kresta and Wood (1993) observed the same phenomenon for solid-liquid mixing using laser doppler anemometry (LDA) and concluded that there is a change in the circulation pattern as the clearance increases. The transition starts at $C = T/4$ and a second circulation loop clearly appears at $C = T/2$ which will affect the impeller discharge angle. The new circulation loops push the solid particles towards the center of the tank.

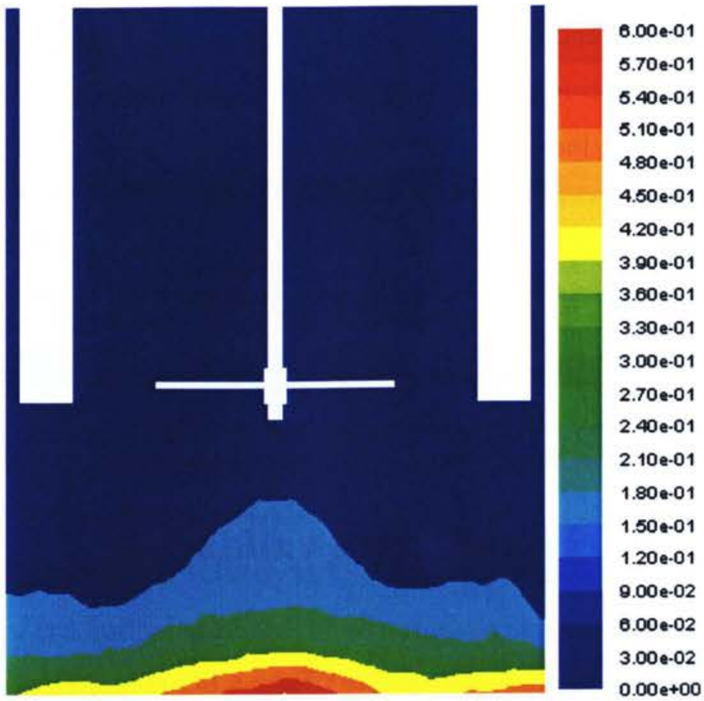

Figure 5.1 CFD solid concentration contour, driven by PBT,
$N = 250\text{rpm}, C = \text{T}/2, \text{X}=10\text{wt\%}, \text{d}_p = 210\mu m, SG = 2.5$

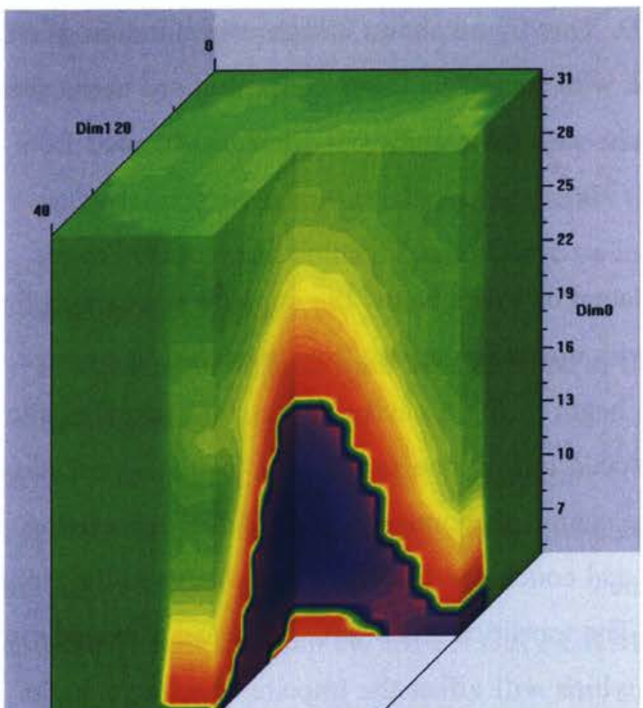

Figure 5.2 3D image by Slicer Dicer of the conductivity tomograms throughout the vessel, PBT impeller $N = 250\text{rpm}, C = \text{T}/2, \text{X}=10\text{wt\%}, \text{d}_p = 210\mu m, SG = 2.5$

As a consequence of the symmetrical flow pattern pushing the solids to the center, there would be a pile-up of solid particles in the middle of the tank as shown in (Figure **5.3**). Figure **5.3** also indicates that the circulation loop forcing the solids to pile-up near the centre of the tank is generated when there is a high impeller clearance $(C = T/2)$; however, this is not the case for low impeller clearances $(C = T/6)$.

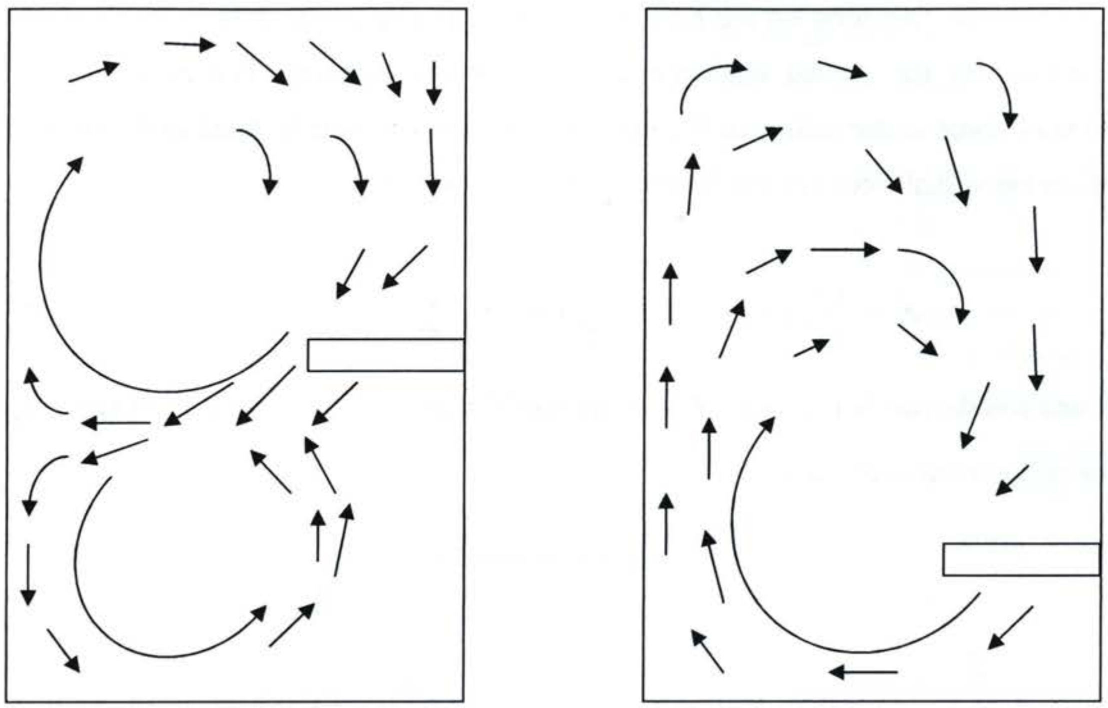

Figure 5.3 Flow circulation patterns in an axial impeller, left: high clearance, right: low clearance

5.2 Quantitative validation

5.2.1 Shaft torque

CFD computes the moment vector about a specified center for the impeller wall zones by summing the cross products of the pressure and viscous force vectors for each face with the moment vector $\vec{r}_{AB}$, which is the vector from the impeller center (A) to the force origin which is the shaft center (B).

$$\overrightarrow{M}_A = \vec{r}_{AB} \times \overrightarrow{F}_p + \vec{r}_{AB} \times \overrightarrow{F}_v \tag{5.1}$$

where A, B are the specified moment center and the force orgin, respectively. $\overrightarrow{M}_A$, $\vec{r}_{AB}$, $\overrightarrow{F}_p$ and $\overrightarrow{F}_v$ are total moment, moment vector, pressure force vector and viscous force vector respectively (Fluent Inc., 2006). The center position in this study was chosen as a point representing the shaft at liquid level intersection (the point coordinates: $x = 0$, $y = 0$, $z = 0.4$). The first term on the right hand side of the Equation (5.1) (5.1is the pressure moment and the second one represents the viscous moment. For example, the net pressure force vector acting on the impeller wall zone can be calculated as the vector sum of the individual force vectors for each cell face as follows:

$$\overrightarrow{F}_p = \sum_{i=1}^{n} \left(p - p_{ref}\right) A\vec{n} = \sum_{i=1}^{n} pA\vec{n} - p_{ref} \sum_{i=1}^{n} A\vec{n} \tag{5.2}$$

where n is the number of faces ,A is the area of the face, p_{ref} is a reference pressure, $\vec{n}$ is the unit normal to the face.

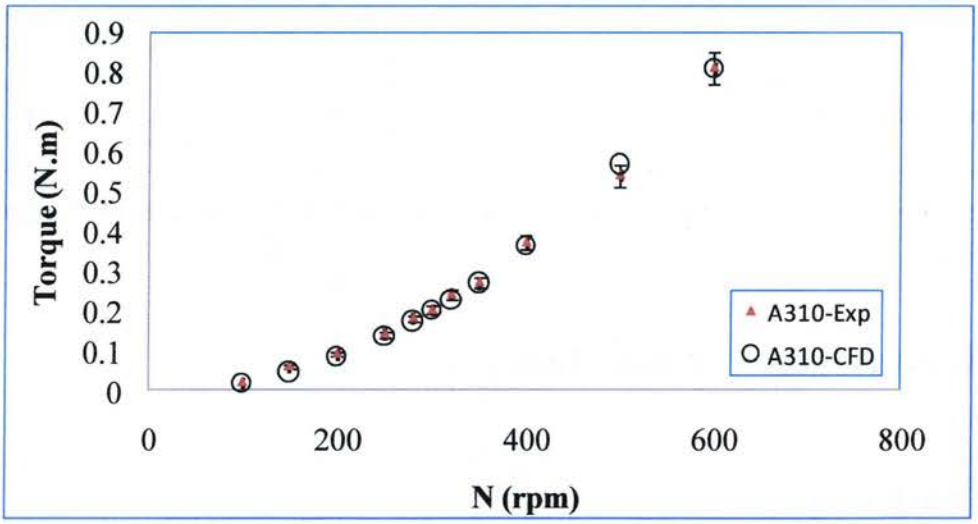

Figure 5.4 CFD and experimental torque comparison of the A310 impeller, $C = T/3, X = 10wt\%, d_p = 210\mu m, SG = 2.5$

Impeller torques at different speeds were measured experimentally using a rotary torque meter (Staiger Mohilo, Germany) and compared with CFD results. It has to be mentioned that the experimental torques were fluctuating at high impeller speeds

$(N = 600rpm)$ due to the turbulent flow. Figure 5.4 shows that the CFD torques are in fairly good agreement with experimental data.

5.2.2 Clouding height

As discussed in the literature review section, clouding height is an indication of homogeneity. Some researchers such as Einenkel (1980) and Kresta and Wood (1993) tried to relate clouding height and homogeneity in order to obtain empirical correlations that could predict the mixing behavior. The most convenient way of measuring clouding height is by visual inspection, and is consequently subjective. In this study, clouding height was measured visually for the experimental part while in the CFD part it was calculated using the solid concentration contours (Figure 5.6, Figure.5.7). Figure 5.5 provides a comparison of clouding height measurements between the experimental and CFD results. In the early stages of suspension, most of the solid particles are at rest; however, as the flow gets stronger more particles get involved with the flow. The more suspended solid particles, the greater interaction between the solid-liquid and solid-solid, therefore less turbulent flow compared with liquid-only situation. Hence, in the early stages of mixing the particles are slightly lifted higher as shown in Figure 5.5. In the experimental part, particle size distribution could be another factor contributing to this phenomenon.

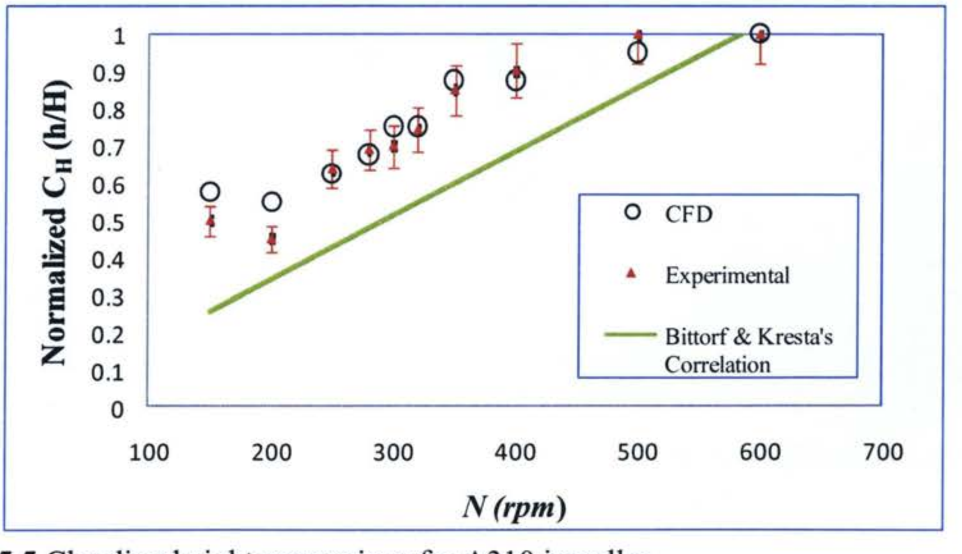

Figure 5.5 Clouding height comparison for A310 impeller,
$X = 10\text{wt}\%, C = T/3, d_p$=210$\mu$m, SG=2.5

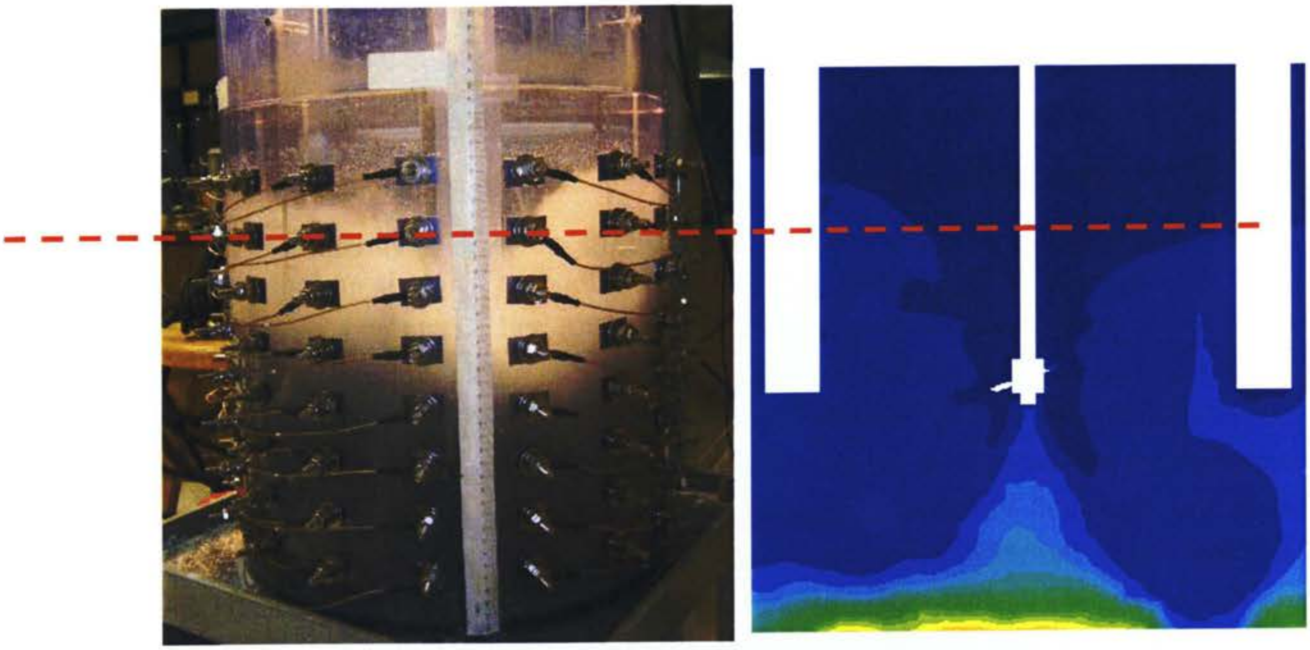

Figure 5.6 Clouding height for A310 impeller, $N = 300\text{rpm}, X = 10\text{wt}\%, C = T/3, d_p$=210$\mu$m, SG=2.5

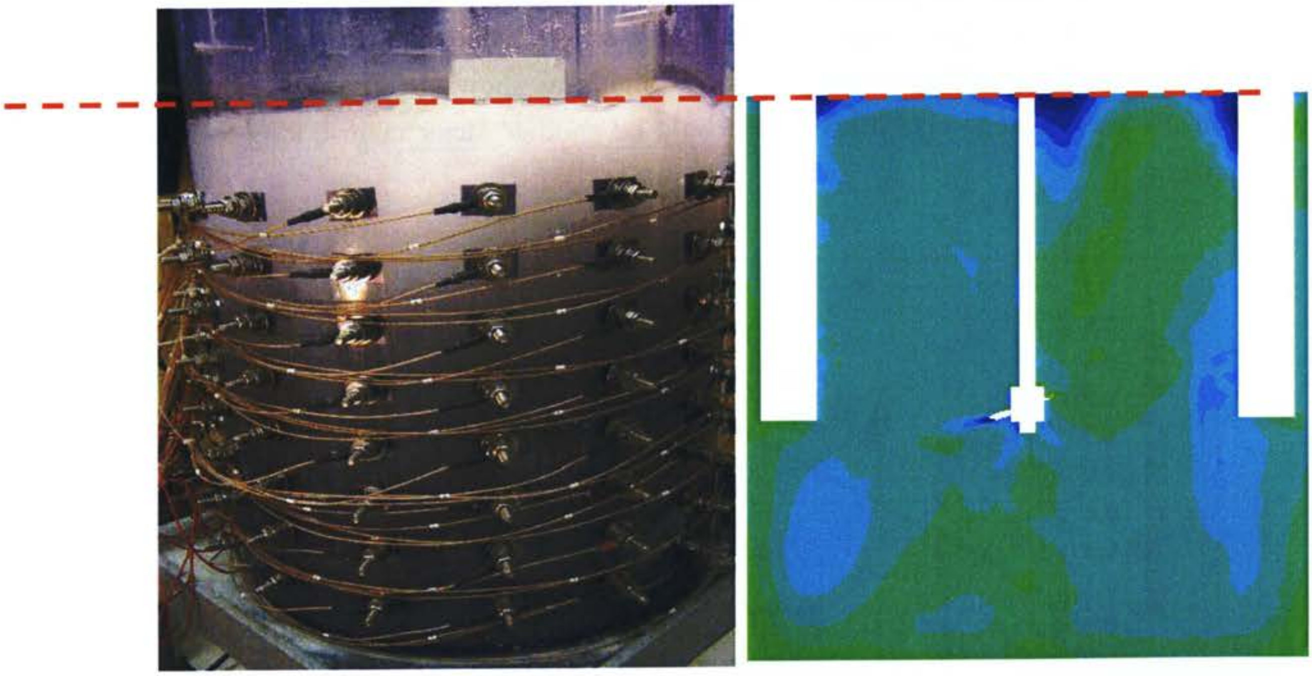

Figure.5.7 Clouding height for A310 impeller, $N = 600\text{rpm}, X = 10\text{wt}\%, C = T/3, d_p$=210$\mu$m, SG=2.5

5.2.3 Just-suspended impeller speed

Just-suspended impeller speed is the speed below which some particles are not suspended in the flow. Below the just-suspended impeller speed maximum concentration gradient occur. Computational fluid dynamics can be used as an alternative to empirical correlations to predict just-suspended impeller speed. Kee and Tan (2002) calculated solid concentrations at different tank levels for several impeller speeds. They considered the inflection point of the solid volume fraction versus impeller speed graph as the just-suspended impeller speed. Therefore, parameter S in the Zwietering (1958) equation could be calculated and compared with the S values reported in the open literature. The CFD result was in reasonable agreement with experiment. Figure 5.8 shows how the just-suspended impeller speed was calculated in this study. In this method, the inflection point of the curve was found from the intersection of tangent lines to curve before and after the inflection point. A similar method was employed by Mak (1992) using the velocity curves to predict N_{js}. The N_{js} values calculated from the Zwietering equation was fairly close to one predicted by CFD in this study.

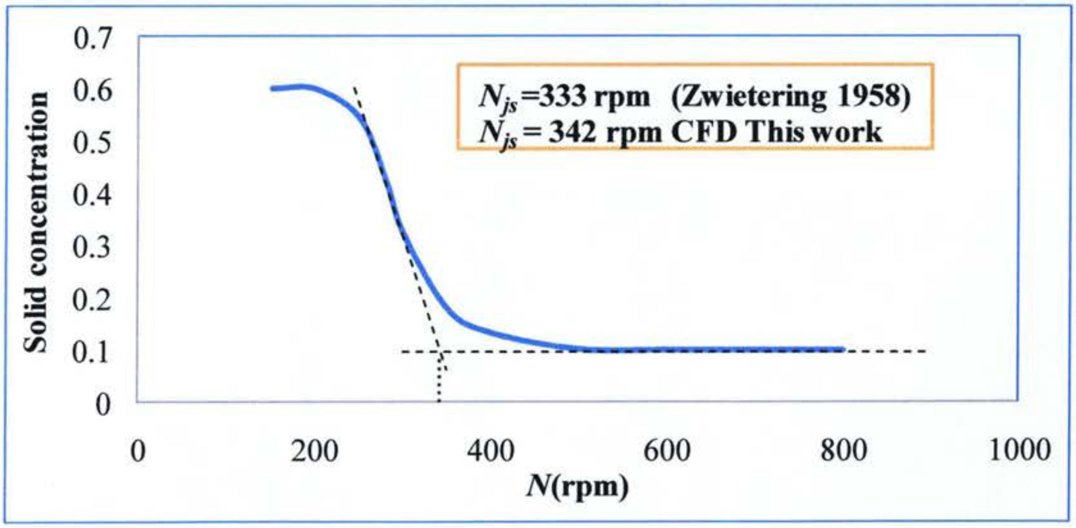

Figure 5.8 Just-suspended impeller speed comparison, A310 solid concentration at 1 mm above the tank bottom $X = 10\text{wt\%}, C = T/3, d_p = 210\mu\text{m}, SG = 2.5$

5.3 Geometry related parameters

Mixing quality is affected by a number of parameters and among them geometry of the vessel and the moving parts have the most. Impellers are a part of moving geometry in which the impeller speed and impeller type can have different effect on mixing behavior.

5.3.1 Impeller speed effect

The effect of impeller speed on mixing performance was also investigated in this study. As expected, the CFD and experimental results showed that stronger flows resulted in higher solid suspension. Figure 5.9 shows the solids concentration contours for impeller speeds from 150–800rpm. It confirms that the system gets homogeneous at an impeller speed (in this case 500 rpm). Similar to experimental setup, eight planes were defined in CFD model at different levels (Figure 5.10, Figure 5.11). Concentration profiles extracted from CFD and tomography are presented in Figure 5.12, Figure 5.13 and Figure 5.14 to analysis system homogeneity.

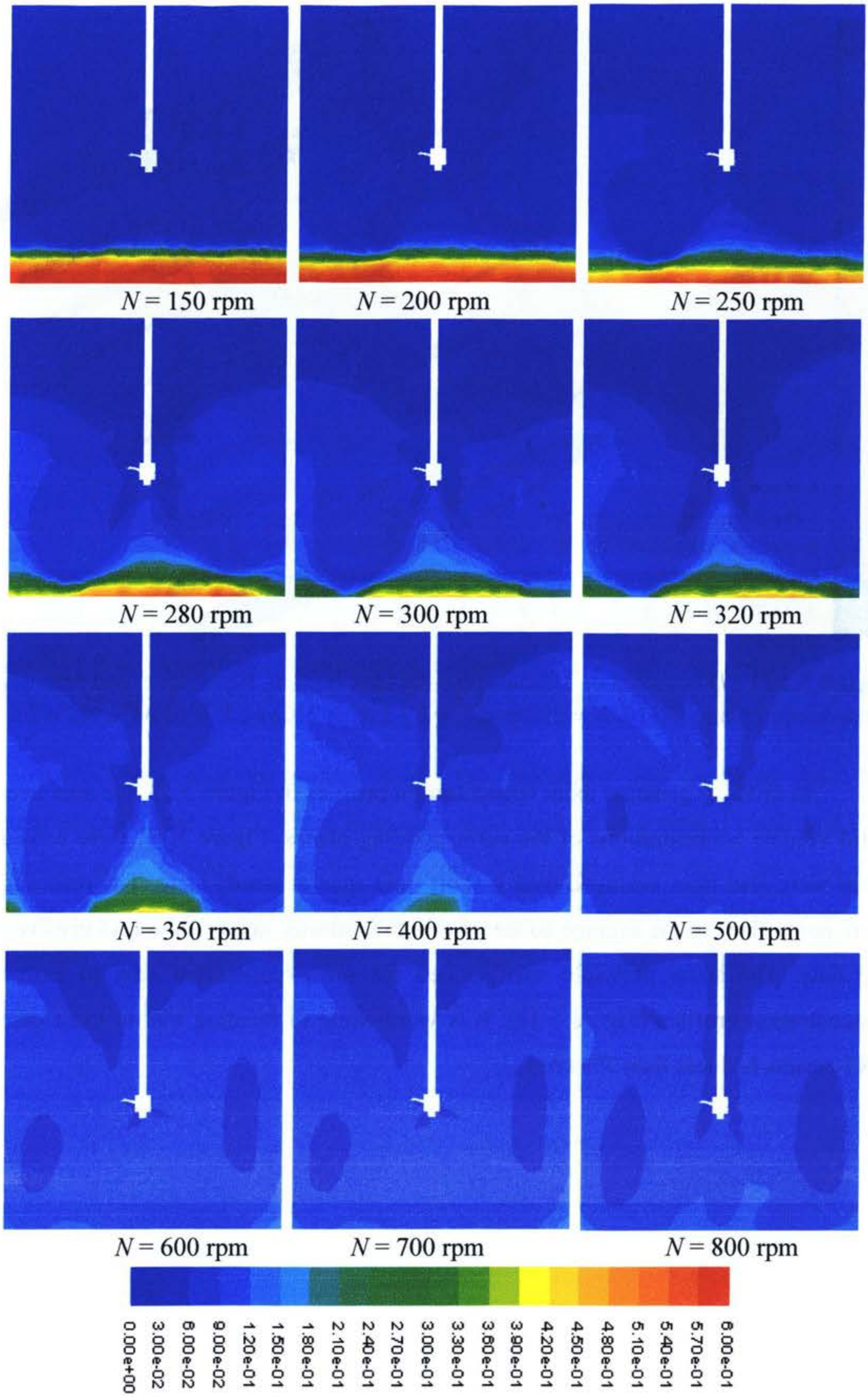

Figure 5.9 CFD solid concentration contours for A310 impeller
$C = T/3, X = 10$ wt%, $d_p = 210\,\mu$m, SG=2.5 at different impeller speed

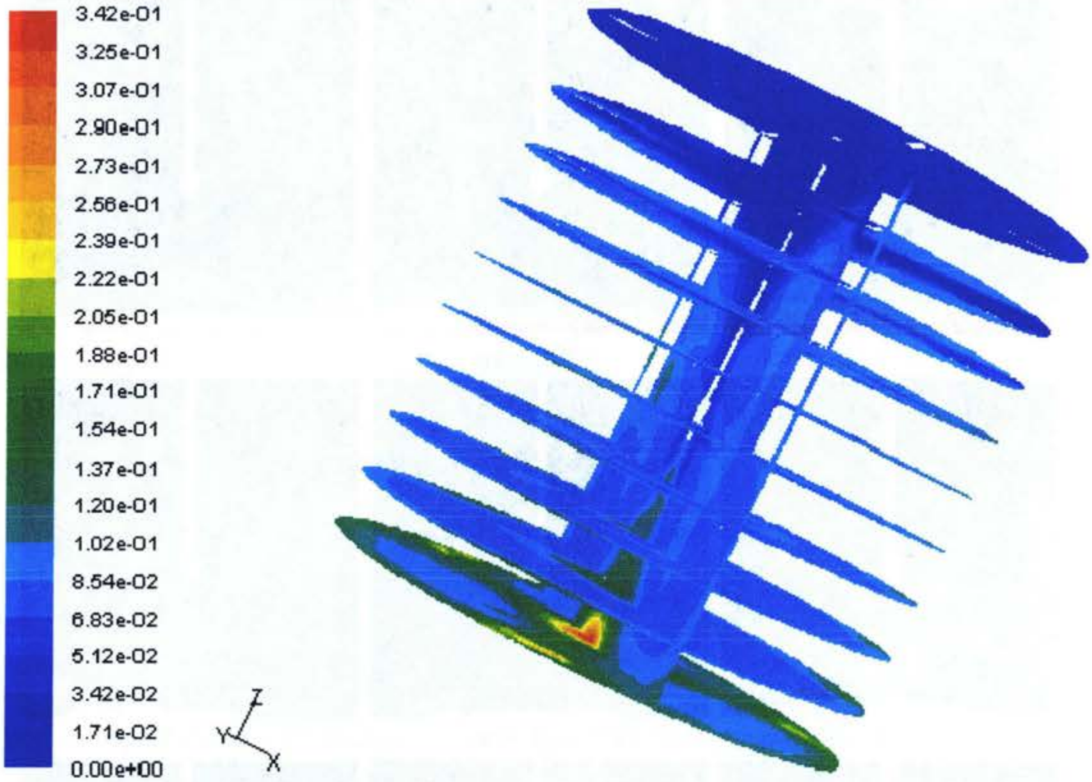

Figure 5.10 CFD contours of 8 planes plus the tank bottom, liquid level and zero degree cross section plane, A310, $N = 300rpm, C = T/3, d_p = 210\mu\text{m}, X = 10$ wt%, $SG = 2.5$

In order to generate axial concentration profiles in Figure 5.13, the area averaged solid volume concentrations of the corresponding planes, Figure 5.11, were considered. They were also time averaged over a short time span at steady state. The resulting data were normalized to the average concentration to minimize numerical errors involved with the data. The same principle was applied for the experimental data to extract the concentration profiles (Figure 5.14). It is worthwhile to mention that in most cases the ERT results had less than 3% error.

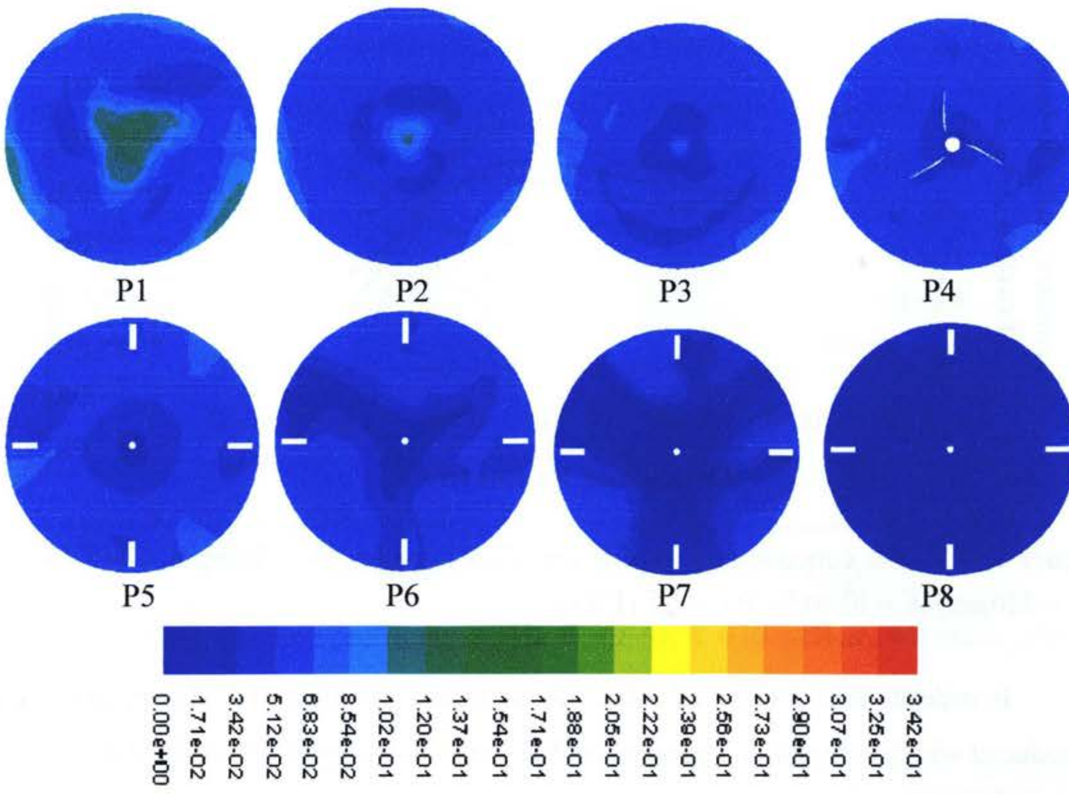

Figure 5.11 Solid concentration contours at different plane, P1 is the bottom plane and P8 is the top plane, A310, $N = 300 rpm, C = T/3, d_p = 210 \mu\text{m}, X = 10$ wt%, $SG = 2.5$

Radial concentration profiles were also calculated and averaged over four different areas (Figure 5.12). These four areas were defined as a central circle and three surrounding areas. In other words, the radius was discretized to four equal distances. Due to the gravity in axial direction, for settling particles, it would be harder to achieve homogeneity in axial direction than radial direction. Therefore, radial concentration profiles were not incorporated for system analysis in this study.

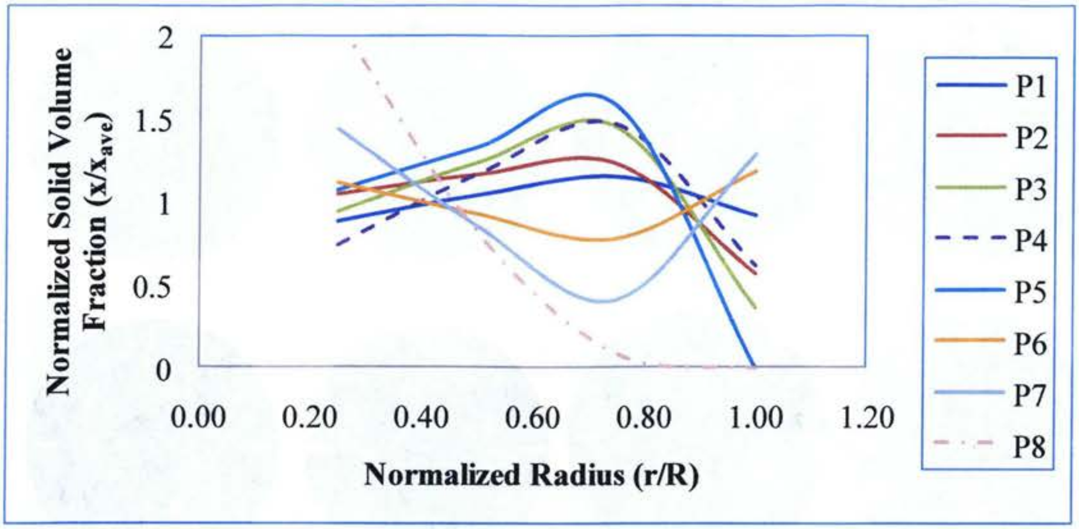

Figure 5.12 Radial concentration profile for A310 impeller, $N = 400rpm$, $C = T/3$, $d_P = 210\mu$m, $X = 10$ wt%, $SG = 2.5$ (ERT)

In order to ease process of data analysis, a new parameter called homogeneity was introduced which is based on variance. In this study, homogeneity is defined as:

$$Homogeneity = 1 - \sqrt{\frac{\sum_{1}^{n}\left(X_V - \overline{X_V}\right)^2}{n}} \tag{5.3}$$

where n, X_V and $\overline{X_V}$ are the number of planes, solid volume concentration and average solid volume concentration respectively.

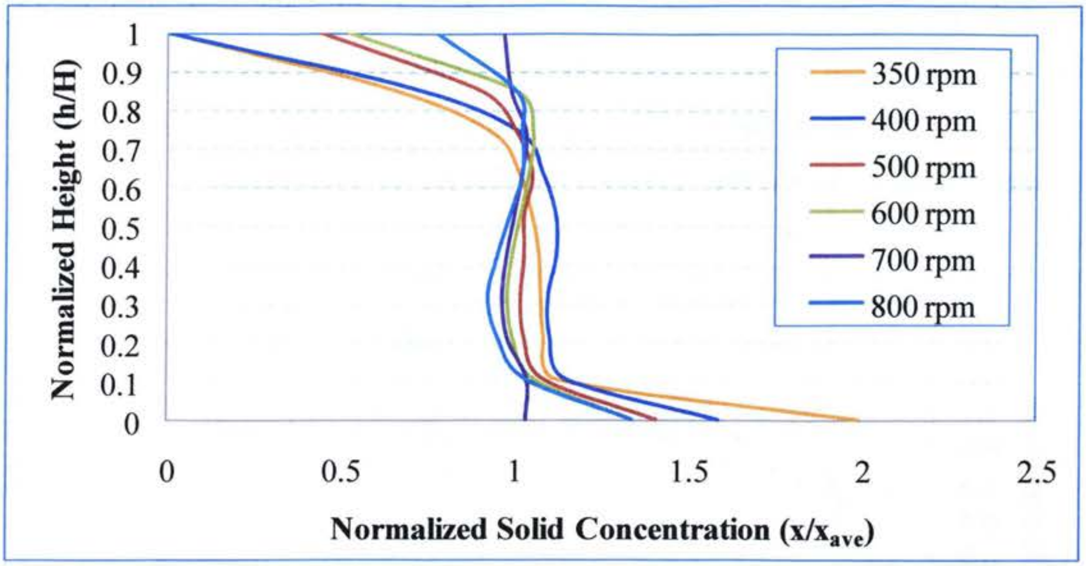

Figure 5.13 Axial concentration profile for A310, $C = T/3, X = 10$ wt%, $d_p = 210\mu$m, SG=2.5 (CFD)

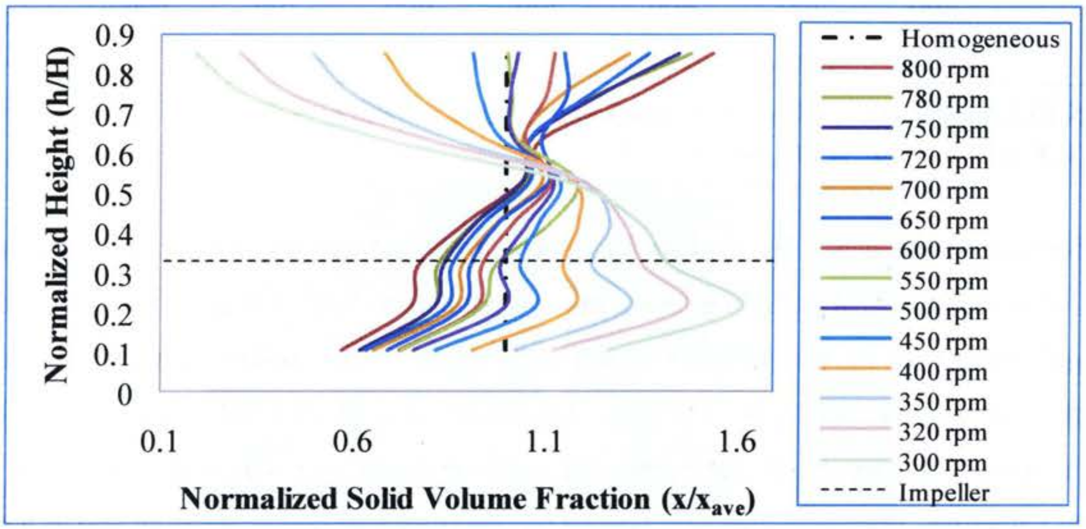

Figure 5.14 Axial concentration profile for A310 impeller, $C = T/3, X = 10$ wt%, $d_p = 210\mu$m, SG=2.5 (ERT)

Equation (5.3) shows that maximum homogeneity occurs when variance is minimum. In other words, homogeneity of one is the goal of all mixing processes since minimum concentration and temperature gradient happens at this state. Figure 5.15 compares the homogeneity predicted by CFD and ERT in mixing flow, driven by A310 impeller at different speed. Both CFD and ERT predicted a maximum impeller speed above which increasing impeller speed is not beneficial to homogeneity, but in fact, detrimental. To ensure that it was not the result of air interference, one experiment was conducted with a lid on the tank liquid level, preventing air to penetrate to the system. The same CFD model was also simulated with a boundary condition change on the liquid surface which was switched from symmetry to wall. Similar results for both CFD and ERT obtained denying the air interference.

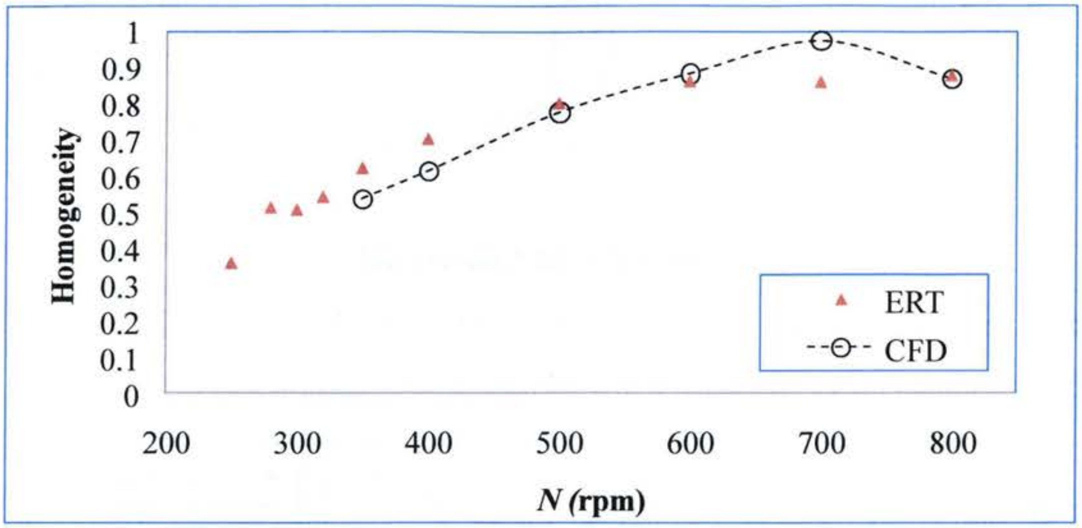

Figure 5.15 Impeller speed effect on homogeneity, A310 impeller,
$C = T/3, X = 10$ wt%, $d_p = 210\mu$m, SG=2.5

Similar results were observed by Einenkel (1980) through analyzing the concentration profiles obtained by local sampling. This phenomenon can be justified by the fact that the centrifugal forces become dominant compared to the other forces present within the circulation loop such as gravity forces (Figure 5.16). The difference between the solid density and the liquid density will keep the solids off the portion of the circulation loop which has high and tense rotational velocities. Therefore, the solid will be mostly forced above the impeller and as a result, homogeneity is decreased (Figure 5.17). Thus, the impeller speed should be always between these two crucial impeller speeds, N_{js} and the maximum homogeneity impeller speed, preferably closer to the latter.

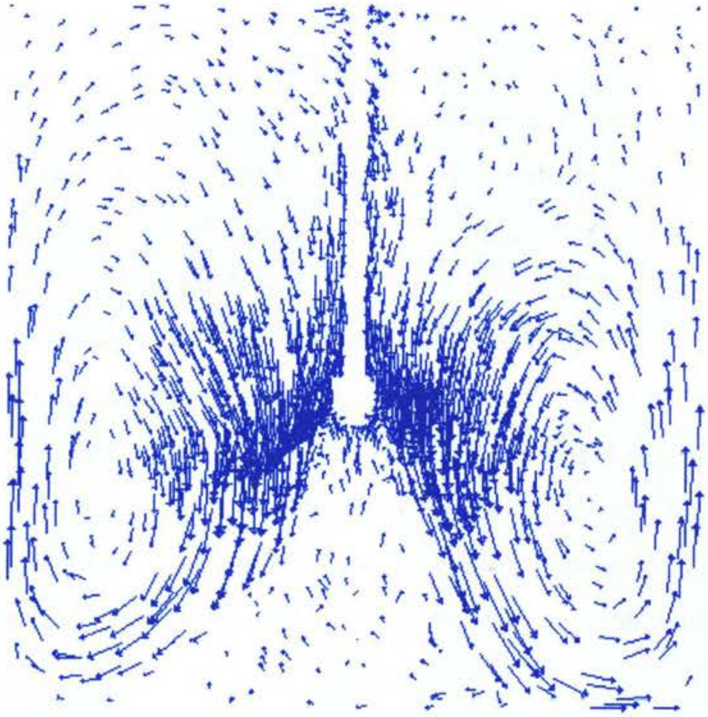

Figure 5.16 CFD velocity vectors of liquid at high impeller speed, A310,
$N = 800rpm, C = T/3, d_p = 210\mu\text{m}, X = 10 \text{ wt\%}, SG = 2.5$

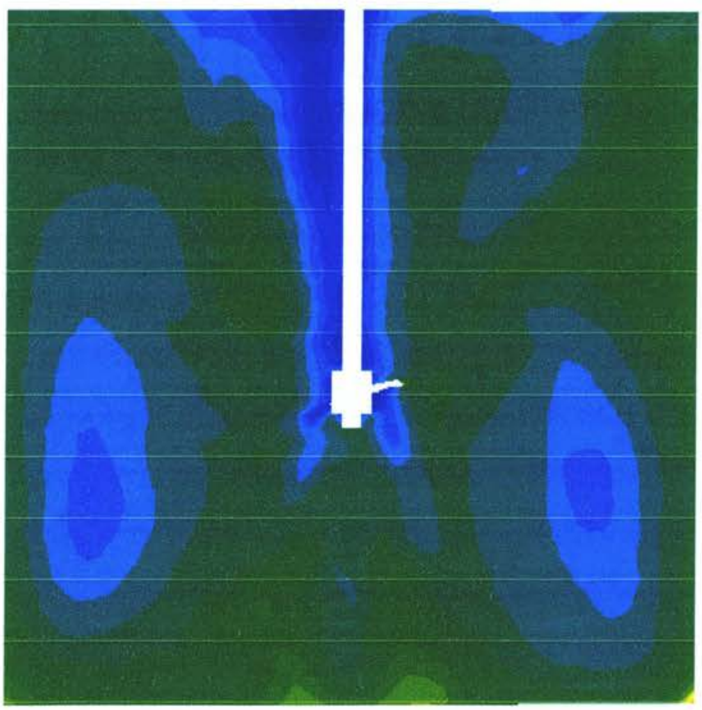

Figure 5.17 CFD solid concentration contours, A310 impeller,
$N = 800rpm, C = T/3, d_p = 210\mu\text{m}, X = 10 \text{ wt\%}, SG = 2.5$

5.3.2 Clearance effect

The next geometrical parameter affecting the flow pattern and homogeneity is the impeller clearance. Figure 5.18 shows the contours of the solid concentration for A310 impeller mounted at different clearances at a given impeller speed. It clearly confirms that the contour of solid concentration at $C = T/3$ has provided the best homogeneity. Three different impeller positions on the shaft were tested for A310 and it was found that the maximum homogeneity and best performance were achieved at $C = T/3$ as illustrated in Figure 5.19. The circulation profile generated at this clearance height best balances the forces within the system resulting in a more homogenous mixture. Figure 5.19 also indicates an interesting result that the impeller speed at which the maximum homogeneity occurs is independent of the impeller position in the range of study. Figure 5.20 illustrate a comparison between the experimental and computational study of clearance effect.

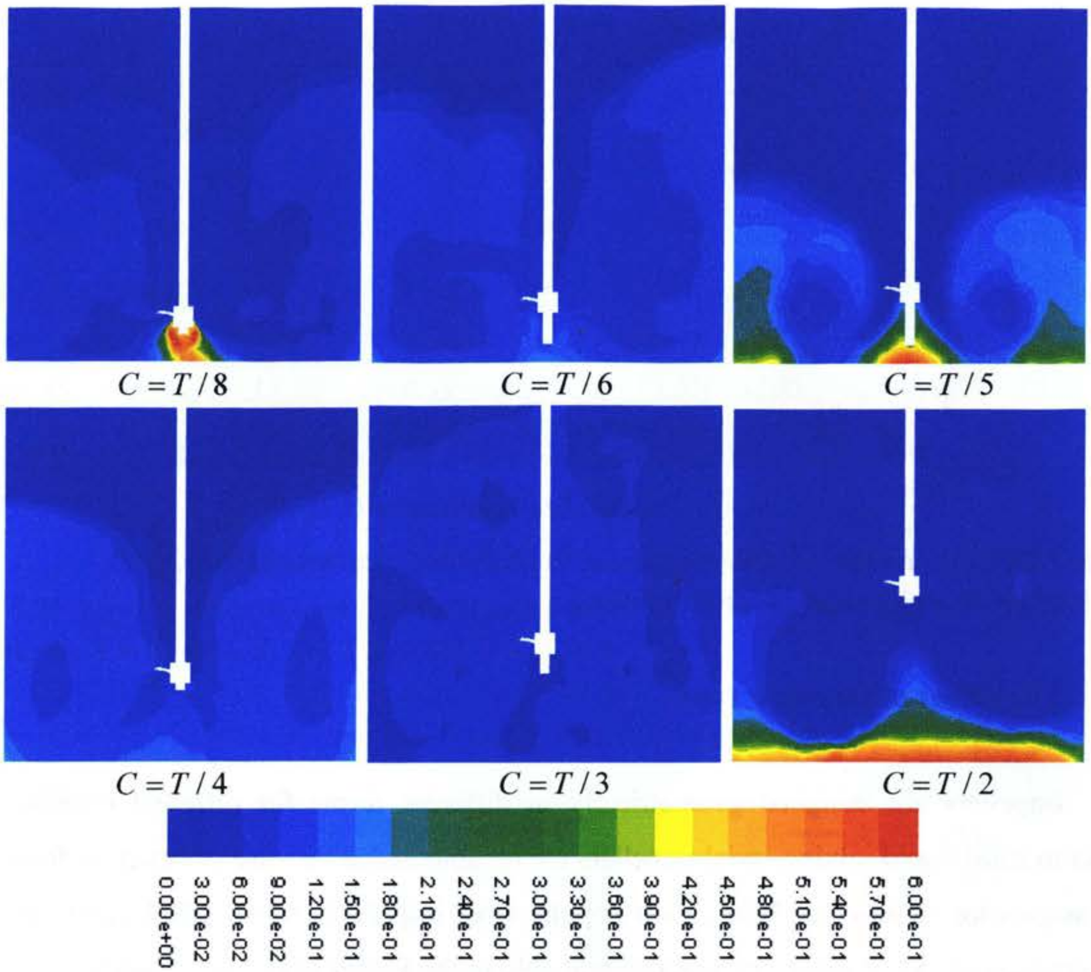

Figure 5.18 Solid concentration contours at different clearance, 45° vertical cross section, A310, $N = 400 rpm, X = 10$ wt%, $d_p = 210 \mu$m, SG=2.5 (CFD)

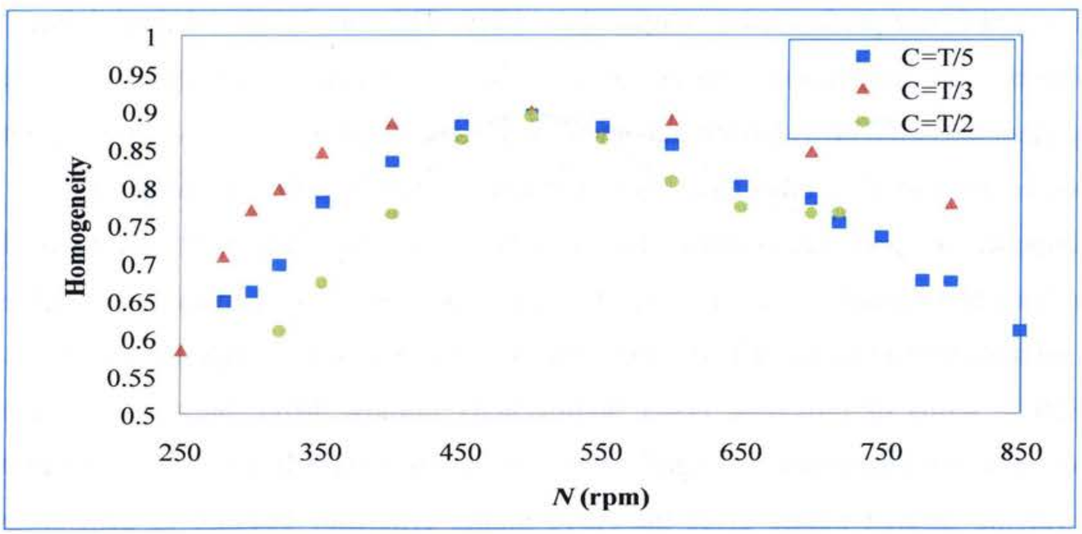

Figure 5.19 Clearance effect, A310, $X = 10$ wt%, $d_p = 210 \mu$m, SG=2.5 (ERT)

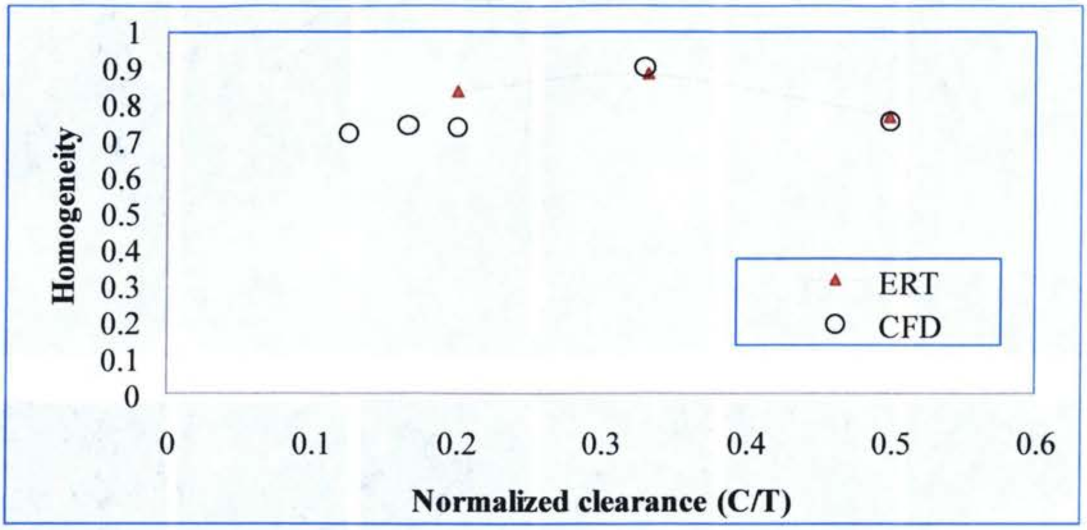

Figure 5.20 CFD and ERT result comparison in predicting clearance effect, A310, $N = 400rpm, X = 10$ wt%, $d_p = 210\mu$m, SG=2.5

5.3.3 The effect of impeller type

Impellers are designed geometrically in different forms for different purposes. With respect to solid-liquid mixing, axial impellers are recommended because of better performance in solid suspension (Paul et al. 2004). Four popular axial impellers, A100, A200, A310 and A320, were considered. A320 geometry was not available in the Fluent library and therefore there is no CFD results for this impeller. Figure 5.21 illustrates the performance of three impellers, A310, A100 and A200. Concentration contours confirm the best performance for A100. Subsequently A310 showed better performance compared to A200. This can be also deducted from Figure 5.22. Figure 5.23 demonstrates the behavior of the four impellers of interest experimentally. Among them the A320 provided the maximum homogeneity, almost 93%, while it consumed the least power. Paul et al. (2004) have also mentioned that in solid-liquid suspension A315 and A320 impellers are preferred because of their higher efficiency. A200 or Pitched Blade Turbine had the least homogeneity (almost 70%). It could be because of the generation of eddies at the end of each blade (Kresta and Wood, 1993). Impeller A100 or marine impeller was the next after the A320 in terms of providing better homogeneity (almost 90%). Subsequently, the A310 provided maximum homogeneity slightly lower (0.5%) than the A100, but much better than the A200. Having tapered blades gives the A310 higher efficiency because of generating fewer eddies at the blade tips.

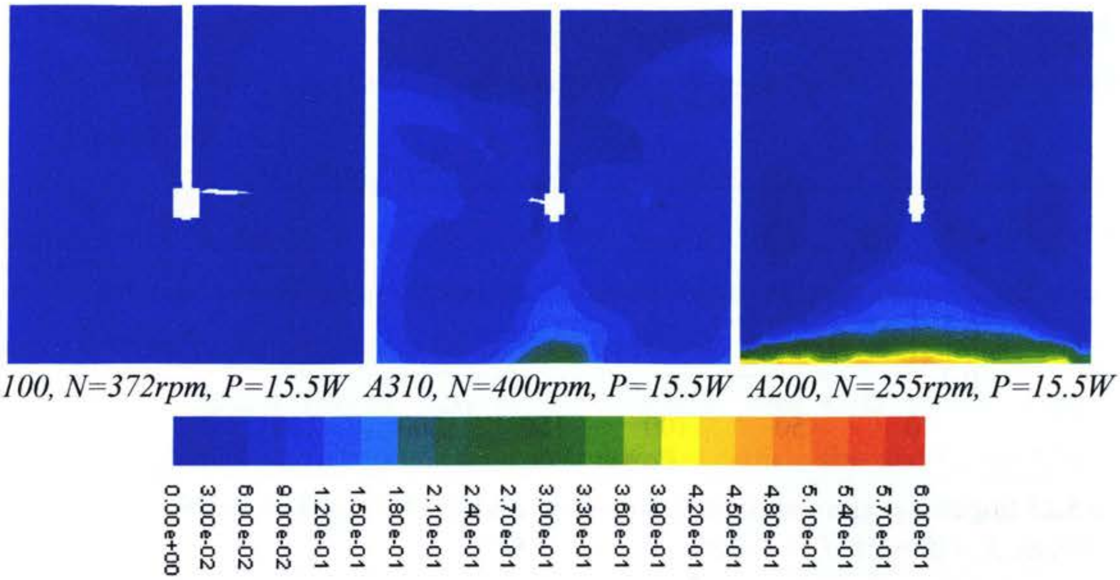

Figure 5.21 Impeller effect on solid concentration contours A310, A100, A200
$N = 400rpm, X = 10$ wt%, $d_p = 210\mu$m, SG=2.5 (CFD)

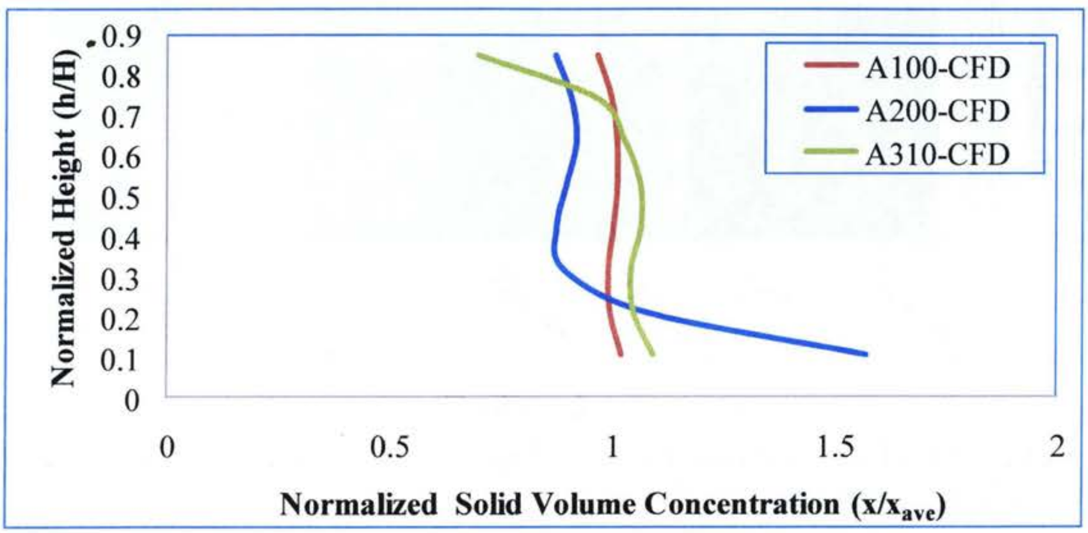

Figure 5.22 Effect of impeller type on axial solid concentration profiles, A100, A200, A310
$N = 400rpm, X = 10$ wt%, $d_p = 210\mu$m, SG=2.5 (CFD)

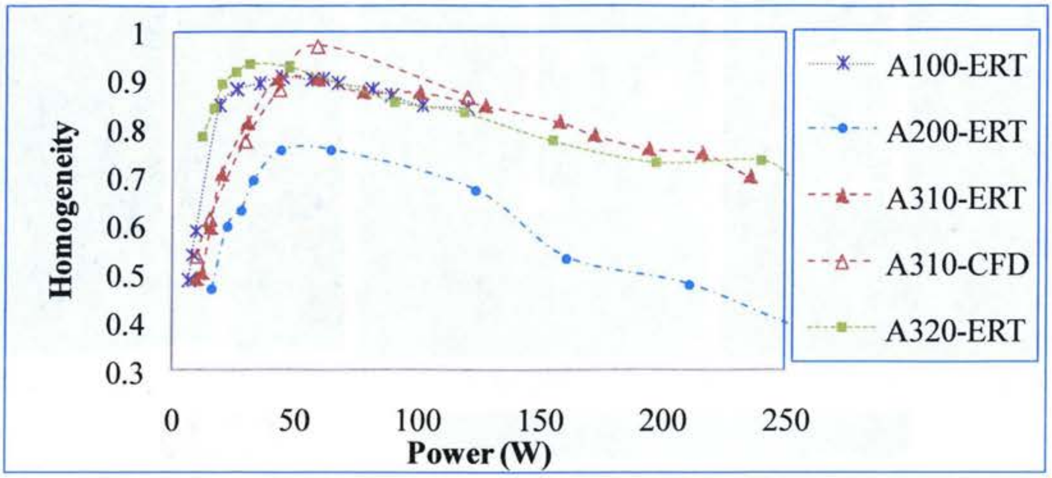

Figure 5.23 Impeller performance on homogeneity, A100, A200, A310, A320
$N = 400rpm, X = 10$ wt%, $d_p = 210\mu$m, SG=2.5 (ERT)

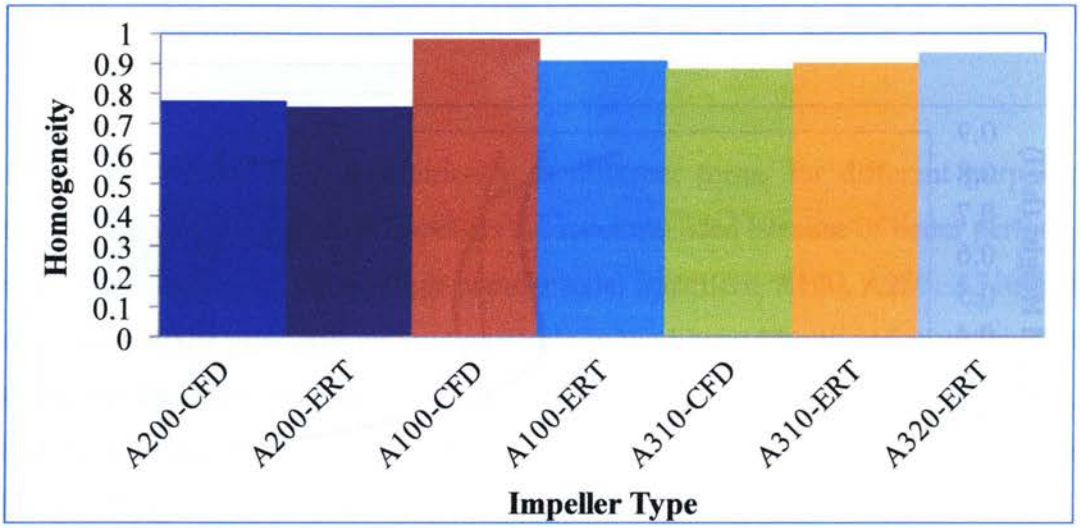

Figure 5.24 CFD and ERT results comparison in impeller performance, A200, A100, A310, A320, $N = 400rpm, X = 10$ wt%, $d_p = 210\mu$m, SG=2.5

5.4 Physical property effects

5.4.1 Particle size effect

One of the most important parameters in solid-liquid suspension is the particle size of the solid. Smaller particle size, results in greater exposure of solid surface area. This exposure lowers the terminal velocity allowing for an easier suspension of the particles. A comprehensive review by Peker and Helvaci (2008) regarding the settling or terminal velocity shows that when the terminal velocity decreases, the mixture approaches a homogeneous mixture or single phase.

For the CFD part of this study, a range of particle sizes between 100-1000μm was considered. However, due to availability only three particle sizes 200μm, 500μm and 1500μm were selected for the experimental section. Mono-particle-size was applied to all CFD cases and no distribution was considered due to the computational cost. Experimental particles had narrow size distribution, enough (Figure **3.3**) to be compared with CFD results. Figure **5.25** demonstrates the solid volume concentration with different particle size and Figure **5.26** depicts the particle size effect on system homogeneity. As expected, the maximum achievable homogeneity decreased as the particle size increased. This was confirmed by both CFD and ERT results as shown in Figure **5.26**. Homogeneity versus particle size graph starts to differ between CFD and tomography results when particle sizes are greater than 300 μm as shown in Figure **5.26**. As explained in Chapter 4, Eulerian-Eulerian inherently assumes particle movement with the flow. This is technically applicable to any multi-phase flow in which this assumption satisfies the flow condition. Figure **5.26** also proves that in this study, CFD results are well in agreement with ERT results up to particle size 300 μm. The discrepancy between the results could be caused by the small drag coefficient used in CFD model $(C_D = 0.44)$ while a higher drag coefficient value would be needed for particles greater than 300 μm . Spilda et al., (2005) studied the effect of the drag coefficient on the CFD model and suggested higher values for the drag coefficient $(C_D = 2)$. In an attempt to find out the relationship between the maximum-homogeneity speed and particle size a logarithmic fitting similar to just-suspended impeller speed was done (Figure **5.27**). The fitting reveals the relationship as follows:

$$N_{max\text{-}homogenity} \propto d_p^{0.166} \tag{5.4}$$

where $N_{max\text{-}homogenity}$ is in the max-homogeneity speed (rps) and d_p is the particle size (m). Equation (5.4) shows that maximum homogeneity speed is proportional to the particle size to the power of 0.166.

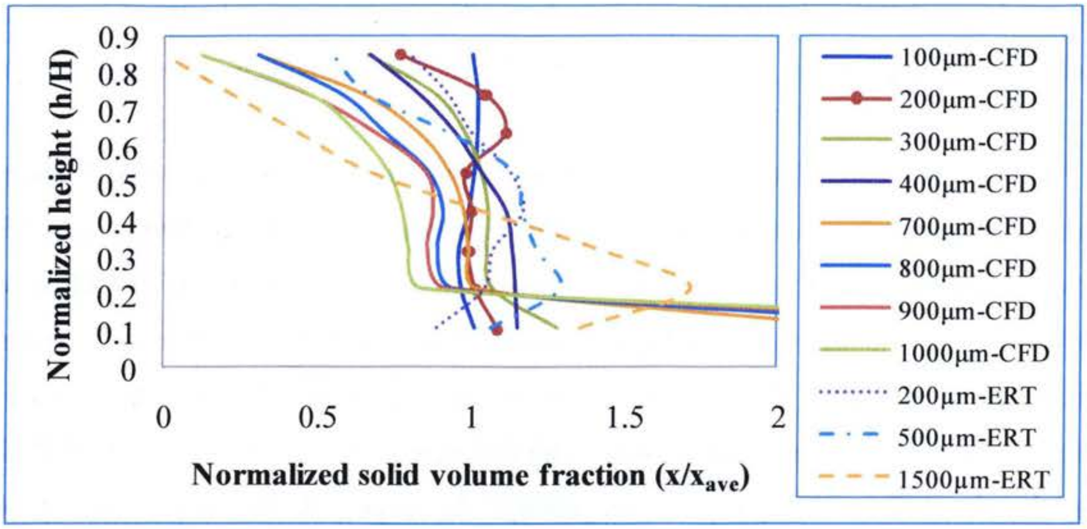

Figure 5.25 CFD and ERT results in particle size effect on concentration profiles, A310 impeller, $C = T/3, X = 10$ wt%, SG=2.5

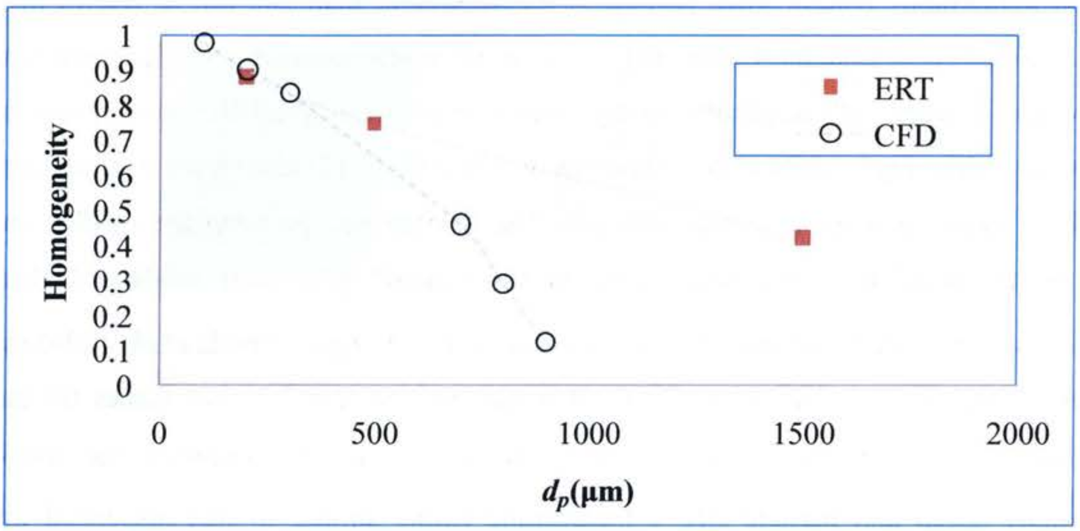

Figure 5.26 CFD and ERT results in particle size effect on homogeneity, A310 impeller, $N = 400rpm, C = T/3, X = 10$ wt%, SG=2.5

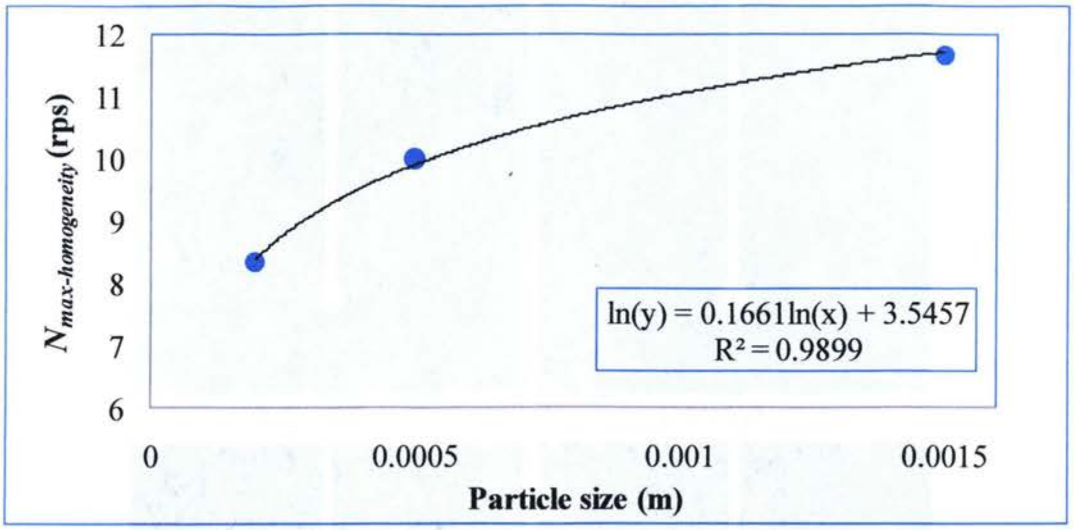

Figure 5.27 Particle size effect on maximum homogeneity impeller speed, A310 impeller, $C = T/3, X = 10$ wt%,SG=2.5

5.4.2 Specific gravity effect

Similar results as those observed with particle size were anticipated for the specific gravity effect. Particles with more density display more resistance to the flow resulting in less homogeneity. Specific gravity affects N_{js} by a power of 0.45 in Zwietering's equation (1958). Figure 5.28 demonstrates the effect of specific gravity on the solid concentration contours. The higher the specific gravity, the lower the homogeneity achieved. Figure 5.29and Figure 5.30 display the same effects of specific gravity in different ways.

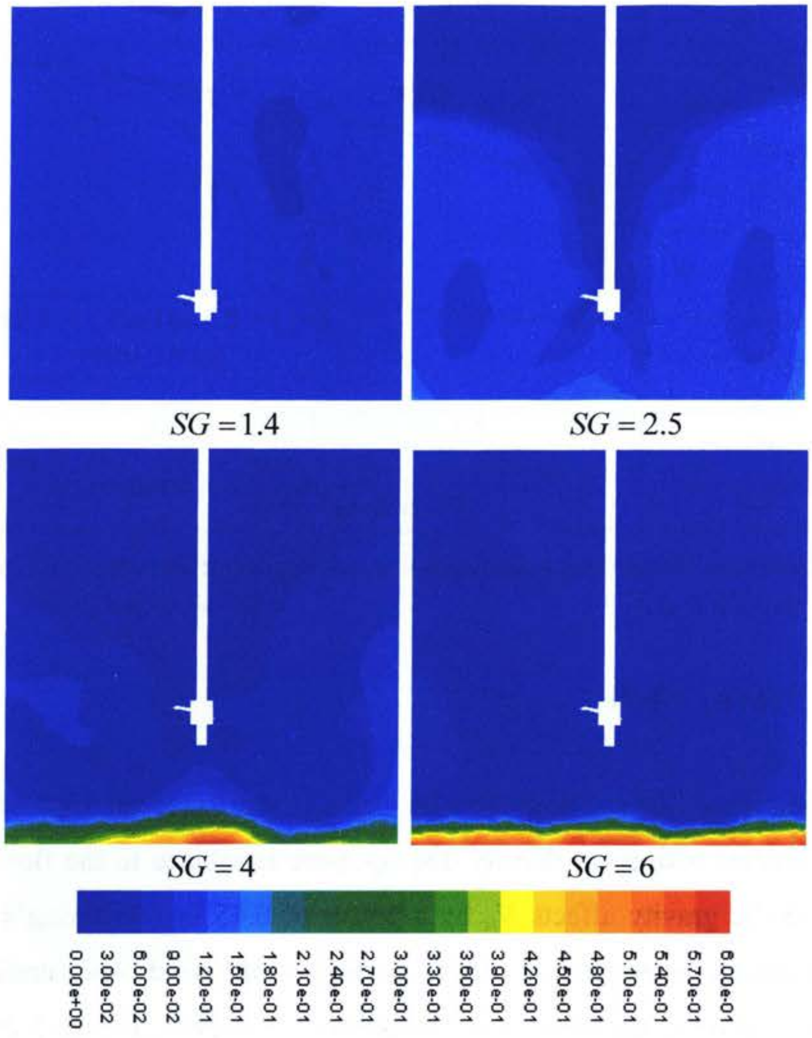

Figure 5.28 CFD contours showing the effect of specific gravity in a flow driven by A310 impeller, $N = 400rpm, C = T/3, X = 10$ wt%, $d_p = 210\mu$m

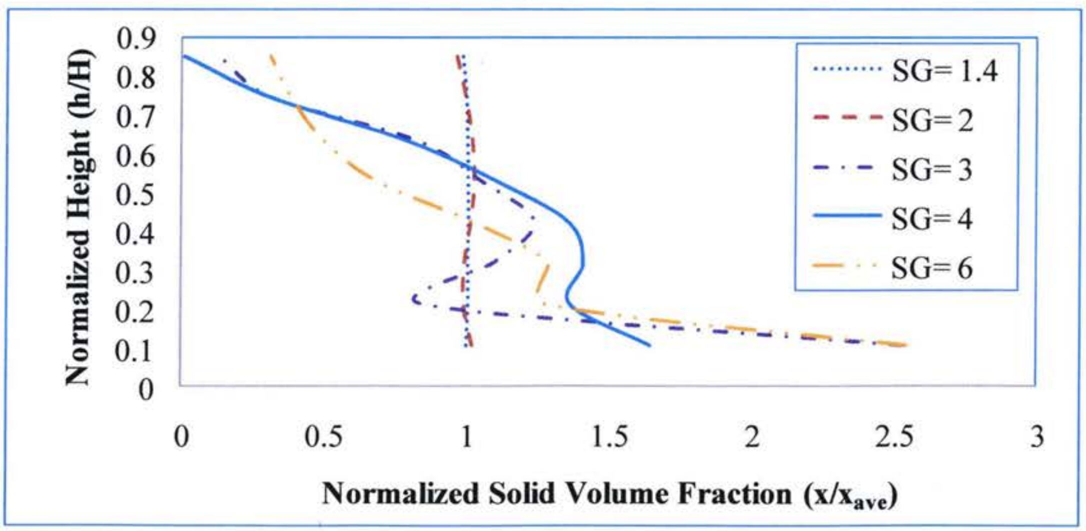

Figure 5.29 Specific gravity effect on axial concentration profile, A310 impeller, $N = 400rpm, C = T/3, X = 10$ wt%, $d_p = 210\mu$m (CFD)

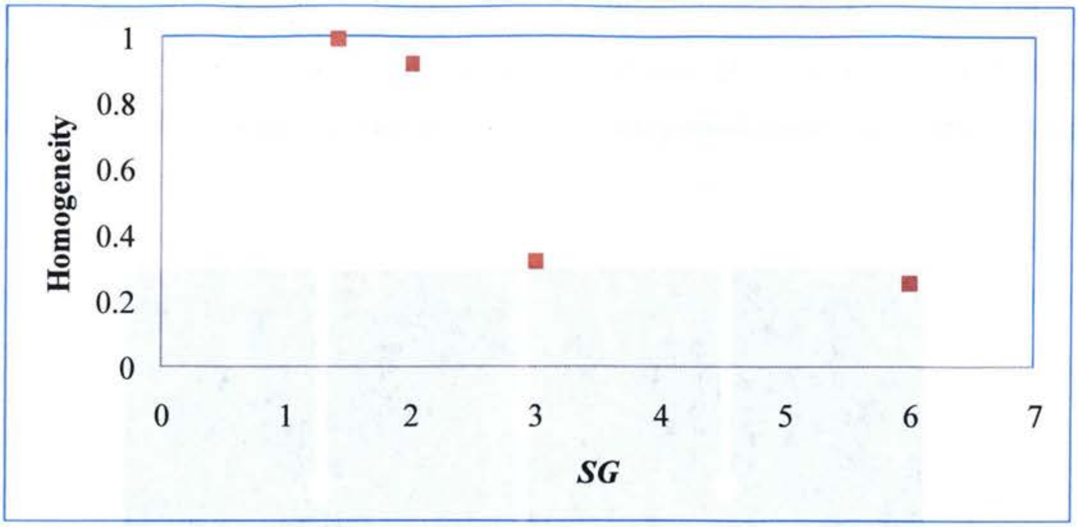

Figure 5.30 Specific gravity effect on homogeneity, A310 impeller, $N = 400rpm, C = T/3, X = 10$ wt%, $d_p = 210\mu$m (CFD)

The only solid particle available with a different density than the glass beads was not similar in size; therefore, no comparison could be made. It is worth mentioning that the specific gravity affects N_{js} with a power between 0.45-0.69 in the empirical correlations (Zwietering, 1958 ; Baldi et al., 1978).

5.4.3 Concentration effect

Concentration effect is another parameter effecting homogeneity due to the increase in the amount of particles which have to be suspended. Consequently, more power is needed for complete suspension. Unfortunately, the effect of this parameter was not observed by CFD due to the omission of some interactions between solid particles such as particle-particle collision as shown in Figure 5.31.

The effect of concentration on mixing behavior was measured by ERT for different concentration (Figure 5.32). Maude (1958) derived the relationship of the concentration and the terminal velocity of the particle. It was called hindered terminal velocity Equation (2.13). It was concluded that increasing the solid phase concentration decreases the particle terminal velocity. Therefore, the suspension of solid particles would be easier. In other words, the axial solid concentration gradient decreases due to the particle hindered terminal velocity Applying

Binomial theorem to Maude equation will give a straight line with a slop of n which is between 2.33-4.64 depending upon the Re number. In an attempt to compare ERT results to Maude's equation the slop of maximum-homogeneity versus solid volume concentration was found 2.6 in Figure 5.33.

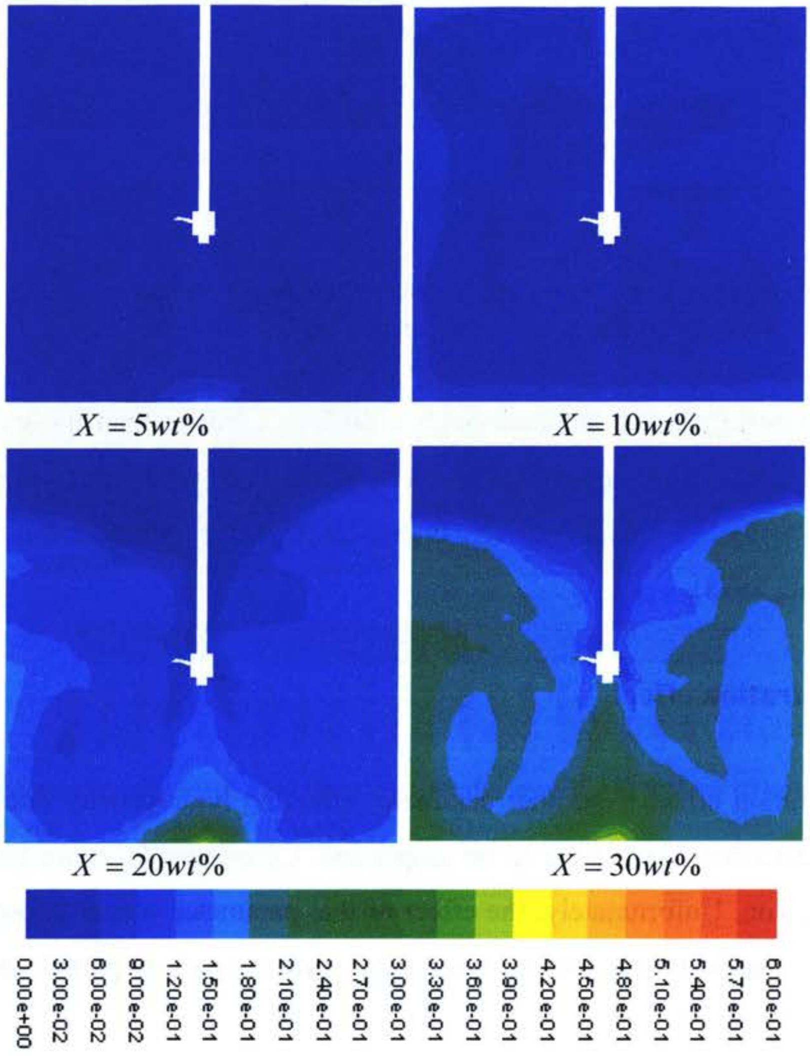

Figure 5.31 Solid concentration contours for the effect of concentration parameter, A310 impeller, $N = 400rpm, C = T/3, d_p = 210\mu m$, $SG = 2.5$ (CFD)

ERT, however, was able to successfully predict the homogenous status of the system. Similar to N_{js} estimation (Zwietering, 1958) correlation, as the solid concentration increases the maximum-homogeneity impeller speed was shifted towards the higher *rpm*'s. This phenomenon can be observed in Figure 5.34 where the relationship between the maximum-homogeneity impeller speed versus concentration is calculated as.:

$$N_{max\text{-}homogenity} \propto x^{0.298} \tag{5.5}$$

Maude (1958) derived the relationship of the concentration and the terminal velocity of the particle. It was called hindered terminal velocity Equation (2.13). It was concluded that increasing the solid phase concentration decreases the particle terminal velocity. Therefore, the suspension of solid particles would be easier. In other words, the axial solid concentration gradient decreases due to the particle hindered terminal velocity (Figure 5.34)

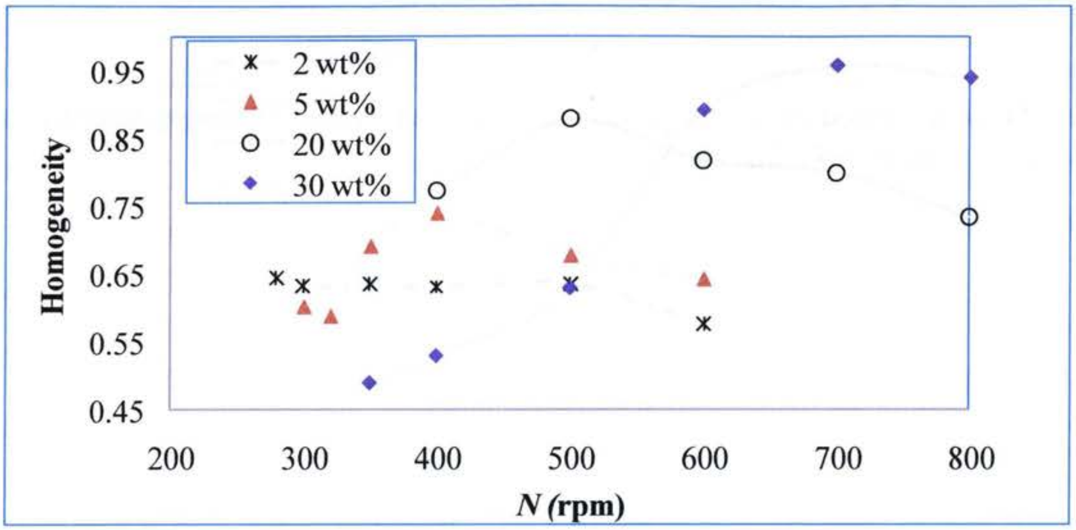

Figure 5.32 Concentration effect on homogeneity at different impeller speed, A310, impeller $C = T/3, d_p = 210\mu m,\ SG = 2.5$ (ERT)

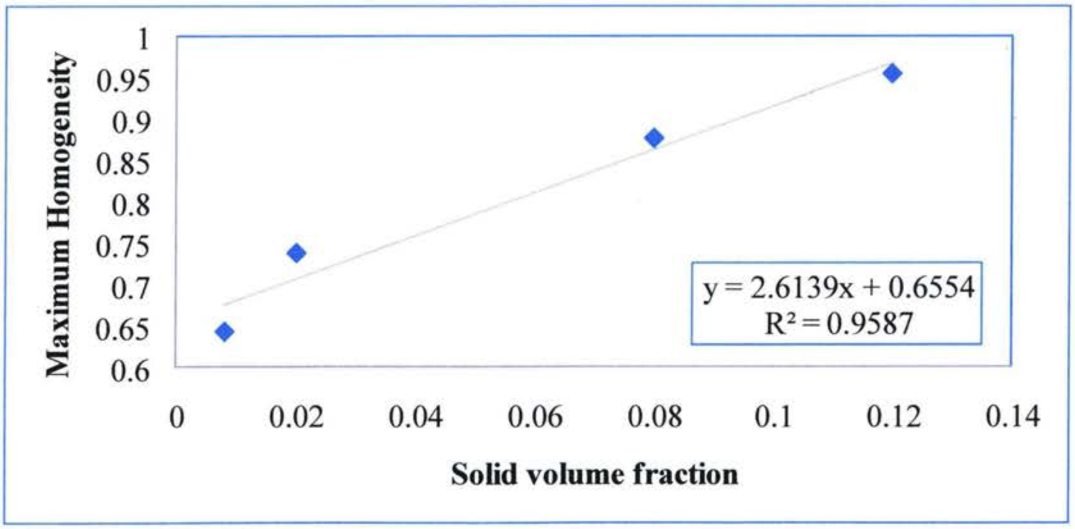

Figure 5.33 Concentration effect on maximum-homogeneity impeller speed, A310 impeller, $C = T/3, d_p = 210\mu m,\ SG = 2.5$ (ERT)

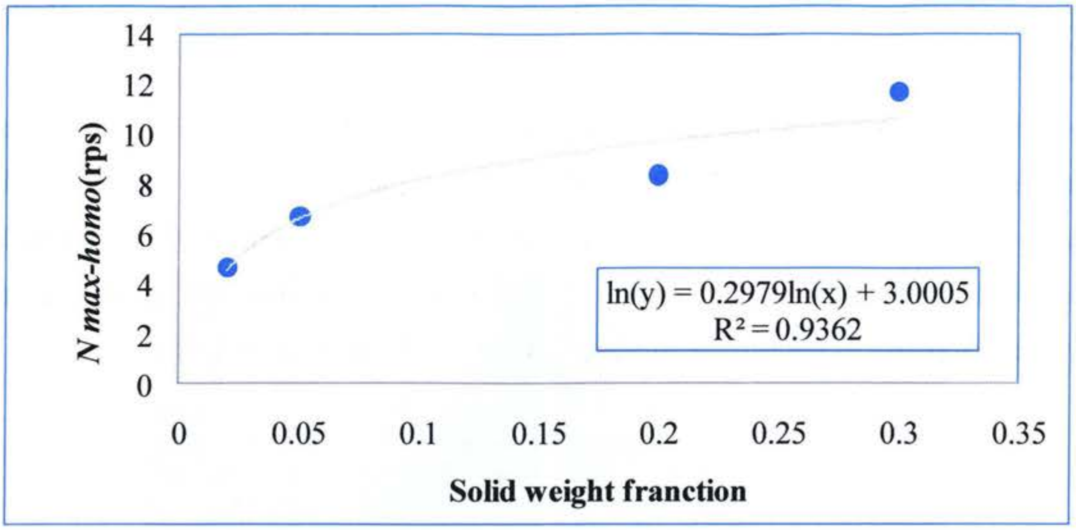

Figure 5.34 concentration effect on impeller speed at which maximum homogeneity occurs $C = T/3, d_p = 210\mu m,\ SG = 2.5$ (ERT)

6 Conclusions and recommendations

6.1 Conclusions

- ✓ Excellent agreement was observed between CFD and experimental torque.

- ✓ Clouding heights estimated using CFD were in good agreement with those obtained through experimental.

- ✓ CFD showed the ability to predict the N_{js} for solid-liquid mixing with a reasonable discrepancy with empirical correlations.

- ✓ Both CFD and ERT showed that there is a critical impeller speed above which any increase to the impeller speed not only will not improve the homogeneity, but also it will be detrimental.

- ✓ Impellers were rated in terms of their performance efficiency to suspend the glass bead particles in water, both computationally and experimentally as follows:

    - A320 > A100 > A310 > A200 which is in agreement with that recommended in literature.

- ✓ An optimum impeller clearance was observed based on CFD and ERT results in terms of achieving homogeneity as C=T/3 which is in the range of recommended clearance in literature (Paul et al., 2004).

- ✓ Particle size effect on mixing homogeneity followed the same trend in both CFD and ERT results up to the particle size 300 μm. From this point high discrepancies were observed due to the deficiency of the CFD model. CFD model needed higher drag coefficient for larger particles. In addition, Eulerian-Eulerian approach which presumes the complete solid particle movement with the flow was employed for modeling and simulation.

- ✓ Specific gravity effect on mixing homogeneity was conducted computationally. A trend as expected was observed; however the criterion was not compared to the experimental data due to lack of denser material with the same size.

- ✓ CFD did not show significant difference in concentration effect due to the lack of interactions between the particles in the model; whereas, ERT showed that the impeller speed at which the maximum homogeneity occurred was proportional to the solid concentration.

6.2 Recommendations for future work

With respect to multi-phase flow and mixing behavior, the following suggestions are offered for further investigation:

- Study of all geometrical effects needed for scaling up such as size and number of impellers, shape, angle and number of impeller blades, shape of the tank bottom, baffles height and clearance and the direction of the impeller pumping both with CFD and ERT.
- Investigating the CFD results when particle-particle interaction is incorporated with the model.
- Conducting experiment with different particles density with ERT to investigate specific gravity effect on homogeneity and also to validate the CFD model.
- Solid-liquid mixing behavior in a continuous process.
- Using ERT to study the mixing behavior in multi-phase flow including gas.
- Considering multi-phase mixing in a non-Newtonian medium to study the effect of fluid rheology.

Nomenclature

Variables and Parameters

A	region of interest in ERT measurement
$\vec{a}$	unit direction vector
b	number of blades
C	impeller clearance (m)
C_H	clouding height (m)
$C_{1\varepsilon}$, $C_{2\varepsilon}$, $C_{3\varepsilon}$	ε momentum equation constants
C_M	Magnus force constant
C_s	Saffman force constant
C_μ	the turbulent (or eddy) viscosity constant
D	impeller diameter (m)
d_i	mean particle diameter of the ith size (m)
d_p, d_s	particle size or diameter (m)
$d_{p(ave)}$	the average particle diameter (m)
$\vec{F}$	external forces vector
$\overrightarrow{F_B}$	Buoyancy force vector
$\vec{F}_{Bk}$	Buoyancy force vector acting on phase k
$\overrightarrow{F_{Br}}$	Brownian force vector
$\overrightarrow{F_D}$	drag force vector
$\overrightarrow{F_g}$	gravity force vector
$\overrightarrow{F_{Int}}$	interaction force vector
$\vec{F_l}$	lift force vector

$\vec{F}_{Lk}$	lift force acting vector on phase k
$\overrightarrow{F_M}$	Mangus force vector
$\vec{F}_p$	pressure force vector
$\overrightarrow{F_S}$	stress force vector
$\vec{F}_v$	viscous forces vector
$\overrightarrow{F_{vm}}$	virtual mass force vector
$\vec{F}_{vmk}$	virtual mass force vector acting on phase k
g_c	gravitational constant (9.81 m/sec^2)
G_k	the generation of turbulence kinetic energy due to the mean velocity gradients
G_b	the generation of turbulence kinetic energy due to buoyancy
l	blade length (m)
H	head of the impeller (m)
K_{lk}	exchange coefficient of phase k
K_{lp}, K_{pl}, K_{SL}	solid-liquid exchange coefficient
M	Torque or moment magnitude (N.m)
$\vec{M}_A$	total moment vector
M_e	number of ERT measurements
m_p	particle mass (kg)
N	impeller speed (rps)
n	number of faces or planes
n_e	number of electrodes
n_i	number of particles in the ith size class
N_{js}	impeller speed for "just suspended" state of particles (rps)
P	impeller power (hp, W)
P_o	power number
p_{ref}	reference pressure (Pa)
Q_p	pumping capacity of an impeller
R	resistance (Ω)

r_p	particle radial distance (m)
$\vec{r}$	arbitrary point location vector
$\vec{r}_{AB}$	moment vector
SG	specific gravity
S_k ,S_ε	User-defined source of k and ε
T	vessel diameter (m)
$\vec{u}$	velocity vector
$\overrightarrow{u_l}$	liquid velocity vector
$\overrightarrow{u_r}$	relative velocity vector
$\vec{u}_p$	particle velocity vector
$\overrightarrow{u_{p,\theta,out}}$	particle tangential velocity after collision
$\overrightarrow{u_{p,\theta,in}}$	particle tangential velocity before collision
$\overrightarrow{u_{wr}}$	whirl velocity
V	voltage (volt)
V_L	fluid velocity (m/s)
V_s	particle settling velocity (m/s)
V_t	particle-free settling velocity (m/s)
V_{ts}	particle-hindered settling velocity (m/s)
$\vec{V}_p$	particle velocity vector
w	blade width (m)
x, X_V	volume fraction of solids in suspension
$\overline{X_V}$	average volume fraction of solids in suspension
x_i	particle coordinates
X	Wt% suspended solids to liquid (kg solid/kg liquid)×100
Y_M	the fluctuating dilatation in compressible turbulence to the overall dissipation rate
Z	liquid depth in vessel (m)

Dimensionless Parameters

C_D	drag coefficient
$Fr = (\frac{\rho_l}{\rho_s - \rho_l})\frac{N_{ts}^{\ 2} D}{g_c}$	Froude number
N_{Fr}	Froude number
N_p	impeller power number
$Re_{imp} = N_{js}D^2/v$	impeller Reynolds number
Re_{MR}	rotational Reynolds number
Re_p	particle Reynolds number
Re_S	particle relative Reynolds number
Re_{SR}	rotational Reynolds number
S	Zwietering constant

Greek Symbols

α_L	liquid phase volume fraction
α_k	phase k volume fraction
μ_k	bulk viscosity (cP or Pa . s)
μ_l	liquid viscosity (cP or Pa . s)
μ_t	the turbulent (or eddy) viscosity
v	kinematic viscosity of the liquid (m^2/sec)
ρ_l	liquid density (lb/ft^3 or kg/m^3)
ρ_p	particle density (kg/m^3)
ρ_s	solid or particle density (lb/ft^3, kg/m^3)
$\sigma_k, \sigma_\varepsilon$	the k and ε turbulent Prandtl numbers

$\sigma_{l,}$	conductivity of the liquid phase (μS/cm)
σ_s	conductivity of the solid phase (μS/cm)
σ_{mc}	conductivity of the mixture (μS/cm)
ψ	particle shape or sphericity
φ	weight fraction of each phases
$\bar{\bar{\tau}}$	stress tensor
ω	angular velocity (rev/Sec)
ω_p	angular velocity of the particle (rev/Sec)
$\vec{\omega}$	angular velocity vector
Ω	tip velocity

Acronyms

CFD	computational fluid dynamics
DAS	data accusation system
ECT	electrical capacitance tomography
EIT	electrical impedance tomography
ERT	electrical resistance tomography
ITS	industrial tomography system
LDA	laser doppler anemometry
LDV	laser doppler velocimetry
LES	large eddy simulation
MRF	multiple reference frame
NMR	nuclear magnetic resonance
PBT	pitched blade turbine
PET	positron emission tomography
PRESTO	pressure staggering option
PSIO	pressure implicit with splitting of operators
QUICK	quadratic upwind scheme

RNG	renormalization group (k-ε turbulent model)
RSM	Reynolds stress model
RT	Rushton turbine
SCG	sensitivity conjugate gradient
SIMPLE	semi-implicit method for pressure-linked equations
SIMPLEC	semi-implicit method for pressure-linked equations consistent
SM	sliding mesh
UST	ultra sound tomography

References

Altway, A., Setyawan, H., Margono, M., & Winardi, S. (2001). Effect of particle size on simulation of three-dimensional solid dispersion in stirred tank. *Chemical Engineering Research and Design, 79*(8), 1011-1016.

Angst, R., & Kraume, M. (2006). Experimental investigations of stirred solid/liquid systems in three different scales: Particle distribution and power consumption. *Chemical Engineering Science, 61*(9), 2864-2870.

Armenante, P. M., & Nagamine, E. U. (1998). Effect of low off-bottom impeller clearance on the minimum agitation speed for complete suspension of solids in stirred tanks. *Chemical Engineering Science, 53*(9), 1757-1775.

Ascanio, G., Foucault, S., & Tanguy, P. A. (2003). Performance of a new mixed down pumping impeller. *Chemical Engineering & Technology, 26*(8), 908-911.

Aubin, J., Fletcher, D. F., & Xuereb, C. (2004). Modeling turbulent flow in stirred tanks with CFD: The influence of the modeling approach, turbulence model and numerical scheme. *Experimental Thermal and Fluid Science, 28*(5), 431-445.

Baldi, G., Conti, R., & Alaria, E. (1978). Complete suspension of particles in mechanically agitated vessels. *Chemical Engineering Science, 33*(1), 21-25.

Baldi, G., Conti, R., & Giannetto, A. (1981). Concentration profiles for solids suspended in a continuous agitated reactor. *AICHE J., 27*(6 , Nov. 1981), 1017-1020.

Barresi, A., & Baldi, G. (1987). Solid dispersion in an agitated vessel: Effect of particle shape and density. *Chemical Engineering Science, 42*(12), 2969-2972.

Barrue, H., Bertrand, J., Cristol, B., & Xuereb, C. (2001). Eulerian simulation of dense solid-liquid suspension in multi-stage stirred vessel. *Journal of Chemical Engineering of Japan, 34*(5), 585-594.

Beck, M. S., & Williams, R. A. (1996). Process tomography: A european innovation and its applications. *Measurement Science and Technology, 7*(3), 215-224.

Becker, H. A. (1959). The effects of shape and Reynolds number on drag in the motion of a freely oriented body in an infinite fluid. *Canadian Journal of Chemical Engineering, 37*, 85-100.

Biswas, P. K., Dev, S. C., Godiwalla, K. M., & Sivaramakrishnan, C. S. (1999). Effect of some design parameters on the suspension characteristics of a mechanically agitated sand–water slurry system. *Materials and Design, 20*(5), 253-265.

Bittorf, K. J., & Kresta, S. M. (2003). Prediction of cloud height for solid suspensions in stirred tanks. *Chemical Engineering Research & Design, 81*(A5), 568-577.

Blazek, J. (2005). *Computational fluid dynamics: Principles and applications* Elsevier Publishers.

Bolton, G. T., & Primrose, K. M. (2005). An overview of electrical tomographic measurements in pharmaceutical and related application areas. *AAPS PharmSciTech, 6*(2), E137-43.

Bujalski, W., Takenaka, K., Paolini, S., Jahoda, M., Paglianti, A., Takahashi, K., et al. (1999). Suspension and liquid homogenization in high solids concentration stirred chemical reactors. *Chemical Engineering Research & Design, 77*(A3), 241-247.

Centric, C., Mignon, D., Bousquet, J., & Tanguy, P. A. (2005). Comparison of mixing in two industrial gas-liquid reactors using CFD simulations. *Chemical Engineering Science, 60*(8-9 SPEC. ISS.), 2253-2272.

Chaouki, J., Larachi, F., & Duduković, M. P. (1997). *Non-invasive monitoring of multiphase flows* Elsevier Science.

Chapman, C. M., Nienow, A. W., Cooke, M., & Middleton, T. C. (1983). Particle-gas-liquid mixing in stirred vessels, part I: Particle-liquid mixing. *TRANS. INST. CHEM. ENGRS., 61*(2 , Mar. 1983), 71-81.

Chen, M., Kontomaris, K., & McLaughlin, J. B. (1998). Direct numerical simulation of droplet collisions in a turbulent channel flow. part I: Collision algorithm. *International Journal of Multiphase Flow, 24*(7), 1079-1103.

Chen, M., Kontomaris, K., & McLaughlin, J. B. (1998). Direct numerical simulation of droplet collisions in a turbulent channel flow. part II: Collision rates. *International Journal of Multiphase Flow, 24*(7), 1105-1138.

Chen, X. Q. &. P.,J.C.F. (2000). Computational modeling of a dilute turbulent liquid-solid flow using a eulerian-lagrangian approach. *International Journal of Numerical Methods for Heat and Fluid Flow, 10*(4), 409-431.

Ciernik, I. F., Dizendorf, E., Baumert, B. G., Reiner, B., Burger, C., Davis, J. B., et al. (2003). Radiation treatment planning with an integrated positron emission and computer tomography (PET/CT): A feasibility study. *International Journal of Radiation Oncology Biology Physics, 57*(3), 853-863.

Cokljat, D., Slack, M., Vasquez, S. A., Bakker, A., & Montante, G. (2006). Reynolds-stress model for eulerian multiphase. *Progress in Computational Fluid Dynamics, 6*(3), 168-178.

Dallavalle, J. M. (1948). Micrometrics. *Pitman, London,*

Decker, S., & Sommerfeld, M. (1996). Calculation of particle suspension in agitated vessels with the euler-lagrange approach. *Proceedings of the 1996 Fluid Mixing 5 Conference,* (140) 71-82.

Dennis, S. C. R., Singh, S. N., & Ingham, D. B. (1980). Steady flow due to a rotating sphere at low and moderate reynolds numbers . *Journal of Fluid Mechanics, 101*(2), 257-279.

Derksen, J. J. (2003). Numerical simulation of solids suspension in a stirred tank. *AIchE Journal, 49*(11), 2700-2714.

Dickey, D. S., & Fenic, J. G. (1976). Dimensional analysis for fluid agitation systems. *Chemical Engineering Journal, 83*(1), 139-145.

Dickin, F., & Wang, M. (1996). Electrical resistance tomography for process applications. *Measurement Science and Technology, 7*(3), 247-260.

Dobaie, A. M. (1995). Dual multiparameter radar observation of rainfall: Application of tomographic technique. (Ph.D., Colorado State University).

Einenkel, W. (1980). Influence of physical properties and equipment design on the homogeneity of suspensions in agitated vessels. *German Chemical Engineering, 3*, 118-124.

Fluent web assistant. (2006). Fluent 6.3 user's guide documentation. *FLUENT Inc.,*

Fradette, L., Tanguy, P. A., Bertrand, F., Thibault, F., Ritz, J. & Giraud, E. (2007). CFD phenomenological model of solid-liquid mixing in stirred vessels. *Computers and Chemical Engineering, 31*(4), 334-345.

Galletti, C., Paglianti, A., Lee, K. C., & Yianneskis, M. (2004). Reynolds number and impeller diameter effects on instabilities in stirred vessels. *AIchE Journal, 50*(9), 2050-2063.

Garside, J., & Al-Dibouni, M. R. (1977). Velocity-voidage relationships for fluidization and sedimentation in solid-liquid systems. *Industrial and Engineering Chemistry Process Design and Development, 16*(2), 206-214.

Ghionzoli, A., Bujalski, W., Grenville, R. K., Nienow, A. W., Sharpe, R. W., & Paglianti, A. (2007). The effect of bottom roughness on the minimum agitator speed required to just fully suspend particles in a stirred vessel. *Chemical Engineering Research & Design, 85*(A5), 685-690.

Gidaspow, D. (1994). *Multiphase flow and fluidization: Continuum and kinetic theory descriptions* Academic Press, Boston, MA.

Gidaspow, D., Bezburuah, R., & Ding, J. (1992). Hydrodynamics of circulating fluidized beds, kinetic theory approach. *In Fluidization VII, Proceedings of the 7th Engineering Foundation Conference on Fluidization,* 75-82.

Giguère, R., Fradette, L., Tanguy, P. A., & Mignon, D. (2008). Characterization of slurry flow regime transitions by ERT. *Chemical Engineering Research and Design, 86*(9), 989-996.

Giguère, R., Fradette, L., Tanguy, P. A., & Mignon, D. (2008). ERT algorithms for quantitative concentration measurement of multiphase flows. *Chemical Engineering Journal, 141*(1-3), 305-317.

Gladden, L. (1994). Nuclear magnetic resonance in chemical engineering: Principles and applications. *Chemical Engineering Science, 49*(20), 3339-3408.

Godfrey, J. C., & Zhu, Z. M. (1994). Measurement of particle-liquid profiles in agitated tanks. *Industrial Mixing Technology: Chemical and Biological Application,* , 181-185.

Grellier, S., Robain, H., Bellier, G., & Skhiri, N. (2006). Influence of temperature on the electrical conductivity of leachate from municipal solid waste. *Journal of Hazardous Materials, 137*(1), 612-617.

Guillard, F., Trägårdh, C., & Fuchs, L. (2000). A study of turbulent mixing in a turbine-agitated tank using a fluorescence technique. *Experiments in Fluids, 28*(3), 225-235.

Guiraud, P., Costes, J., & Bertrand, J. (1997). Local measuremts of fluid and particle velocities in a stirred suspension. *Chemical Engineering Journal, 68*(2-3), 75-86.

Hagenson, L. C., & Doraiswamy, L. (1998). Comparison of the effects of ultrasound and mechanical agitation on a reacting solid-liquid system. *Chemical Engineering Science, 53*(1), 131-148.

Hao, Z. (2005). CFD simulation of segregation in particulate multiphase flows with binary solids. *Proceedings of the American Society of Mechanical Engineers Fluids Engineering Division Summer Conference,* 669-676.

Harlow, F. H., & Welch, J. E. (1965). Numerical calculation of time-dependent viscous incompressible flow of fluid with free surface. *Physics of Fluids, 8*(12), 2182-2189.

Hicks, M. T., Myers, K. J., & Bakker, A. (1997). Cloud height in solids suspension agitation. *Chemical Engineering Communications, 160*, 137-155.

Hiller, D., & Ernest, H. (1982). Tomography using transmission and reflection: Application to medical diagnostics. *Ac. Imag., Vol.12, Proc. 12th Int. Symp*(Plem Press), 557-563.

Holden, P. J., Wang, M., Mann, R., Dickin, F. J., & Edwards, R. B. (1999). On detecting mixing pathologies inside a stirred vessel using electrical resistance tomography. *Chemical Engineering Research and Design/Official Journal of the European Federation of Chemical Engineering: Part A, 77*(A8), 709-712.

Holden, P. J., Wang, M., & Mann, R. (1998). Imaging stirred-vessel macromixing using electrical resistance tomography. *AIchE Journal, 44*(4), 780-790.

Hoomans, B. P. B., Kuipers, J. A. M., Briels, W. J., & Van Swaaij, W. P. M. (1996). Discrete particle simulation of bubble and slug formation in a two-dimensional gas-fluidised bed: A hard-sphere approach. *Chemical Engineering Science, 51*(1), 99-118.

Hua, P., Woo, E. J., Webster, J. G., Tompkins, W. J., Inc, S. G., & Estates, H. (1993). Using compound electrodes in electrical impedance tomography. *Biomedical Engineering, IEEE Transactions, 40*(1), 29-34.

Industrial Tomography System Ltd. (2005). Operating Manual. *Industrial Tomography System Ltd.*

Johansen, S. T. (2002). Multiphase flow modeling of metallurgical flows. *Experimental Thermal and Fluid Science, 26*(6-7), 739-745.

Kasat, G. R., Khopkar, A. R., Ranade, V. V., & Pandit, A. B. (2008). CFD simulation of liquid-phase mixing in solid-liquid stirred reactor. *Chemical Engineering Science, 63*(15), 3877-3885.

Kaufmann, A., Simonin, O., Poinsot, T., & Helie, J. (2002). Dynamics and dispersion in eulerian-eulerian DNS of two-phase flows. *Center for Turbulence Research, Proceedings of the Summer Program,* 381-392.

Kee, N. C. S., & Tan, R. B. H. (2002). CFD simulation of solids suspension in mixing vessels. *Canadian Journal of Chemical Engineering, 80*(4), 721-726.

Khopkar, A. R., Kasat, G. R., Pandit, A. B., & Ranade, V. V. (2006). Computational fluid dynamics simulation of the solid suspension in a stirred slurry reactor. *Industrial and Engineering Chemistry Research, 45*(12), 4416-4428.

Kim, I., Elghobashi, S., & Sirignano, W. A. (1998). On the equation for spherical-particle motion: Effect of reynolds and acceleration numbers. *Journal of Fluid Mechanics, 367*, 221-253.

King, R. L., Hiller, R. A., & Tatterson, G. B. (1988). Power consumption in a mixer. *AIChE Journal, 34*(3), 506-509.

Kleinstreuer, C. (2003). *Two-phase flow: Theory and applications* Taylor & Francis Books,Inc.

Kresta, S. M., & Wood, P. M. (1993). The mean flow field produced by a 45 pitched blade turbine: Changes in the circulation pattern due to off-bottom clearance. *Canadian Journal of Chemical Engineering, 71*, 42-53.

Launder, B. E., & Spalding, D. B. (1972). *Lectures in mathematical models of turbulence.* London, England: Academic Press

Leonard, B. P., & Mokhtari, S. (1990). Beyond first-order upwinding. the ultra-sharp alternative for non-oscillatory steady-state simulation of convection. *International Journal for Numerical Methods in Engineering, 30*(4), 729-766.

Li, A., & Ahmadi, G. (1992). Dispersion and deposition of spherical particles from point sources in a turbulent channel flow. *Aerosol Science and Technology, 16*(4), 209-226.

Ljungqvist, M., & Rasmuson, A. (2001). Numerical simulation of the two-phase flow in an axially stirred vessel. *Chemical Engineering Research & Design, 79*(A5), 533-546.

Loh, W. W., Pinheiro, P. A. T., Dickin, F. J., & Waterfall, R. C. (1998). Low common mode error data collection strategy for electrical resistance tomography. *Electronics Letters, 34*(15), 1489-1490.

Lu, W. M., Wu, H. Z., & Ju, M. Y. (1997). Effects of baffle design on the liquid mixing in an aerated stirred tank with standard rushton turbine impellers. *Chemical Engineering Science, 52*(21-22), 3843-3851.

Luo, J. Y., Issa, R. I., & Gosman, A. D. (1994). Prediction of impeller induced flows in mixing vessels using multiple frames of reference. *8th European Conf. on Mixing, Cambridge, 136,* 549-556.

Madupu, A., Mazumdar, A., Jinsong, Z., Roelant, D., & Srivastava, R. (2005). Electrical resistance tomography for real-time mapping of the solid-liquid interface in tanks containing optically opaque fluids. *Proceedings of the SPIE - the International Society for Optical Engineering, 5674*(1) 36-46.

Mak, A. T. C. (1992). *Solid-liquid mixing in mechanically agitated vessels.* Ph.D. dissertation, University of London.

Mann, R., Williams, R., Dyakowski, T., Dickin, F., & Edwards, R. (1997). Development of mixing models using electrical resistance tomography. *Chemical Engineering Science, 52*(13), 2073-2085.

Mann, R. (2005). Electrical process tomography: Seeing "without eyes" inside stirred vessels. *Journal of Zhejiang University (Science), 6A*(12), 1379-1385.

Mann, R., Stephenson, D. R., & Bolton, G. T. (2008). Recent developments in electrical resistance tomography for the pharmaceutical industries. *Chimica Oggi, 26*(1 SUPPL. PAT), 6-8.

Mao, Z. S., Feng, W., Yuefa, W., & Chao, Y. (2006). Measurement of phase holdups in liquid-liquid-solid three-phase stirred tanks and CFD simulation. *Chemical Engineering Science, 61*(22), 7535-7550.

Maude, A. D., & Whitmore, R. L. (1958). A generalized theory of sedimentation. *British Journal of Applied Physics, 9*, 477-482.

Mavros, P. (2001). Review paper: Flow visualization in stirred vessels: A review of experimental techniques. *Chemical Engineering Research and Design/Official Journal of the European Federation of Chemical Engineering: Part A, 79*(A2), 113-127.

McDonough, R. J. (1992). *Mixing for the process industries* Van Nostrand Reinhold, New York.

McKee, S. L., Williams, R. A., & Boxman, A. (1995). Development of solid-liquid mixing models using tomographic techniques. *Chemical Engineering Journal and the Biochemical Engineering Journal, 56*(3), 101-107.

McKee, S. L., Williams, R. A., Mann, R., Dickin, F. J., Brinkel, J., Ying, P., et al. (1994). Measurement of concentration profiles and mixing kinetics in stirred tanks using a resistance tomographic technique. *Institution of Chemical Engineers Symposium Series, 136*, 9-16.

Micale, G., Grisafi, F., Rizzuti, L., & Brucato, A. (2004). CFD simulation of particle suspension height in stirred vessels. *Chemical Engineering Research & Design, 82*(A9), 1204-1213.

Micale, G., Montante, G., Grisafi, F., Brucato, A., & Godfrey, J. (2000). CFD simulation of particle distribution in stirred vessels. *Chemical Engineering Research and Design, 78*(3), 435-444.

Micheletti, M., & Yianneskis, M. (2004). Study of fluid velocity characteristics in stirred solid-liquid suspensions with a refractive index matching technique. *Proceedings of the Institution of Mechanical Engineers E, Journal of Process Mechanical Engineering, 218*(E4), 191-204.

Montante, G., Micale, G., Magelli, F., & Brucato, A. (2001). Experiments and CFD predictions of solid particle distribution in a vessel agitated with four pitched blade turbines. *Chemical Engineering Research & Design, 79*(A8), 1005-1010.

Myers, K., Bakker, A., & Fasano, J. (1995). Simulation and experimental verification of liquid-solid agitation performance. *AIChE Symp Series, 305*, 139-145.

Ochieng, A., & Lewis, A. E. (2006). CFD simulation of solids off-bottom suspension and cloud height. *Hydrometallurgy, 82*(1-2), 1-12.

Oldshue, J. Y. (1983). Fluid mixing technology. *New York: McGrawHill Pub Co, 468*

Oliveira, L. A., Costa, V. A. F., & Baliga, B. R. (2002). A lagrangian-eulerian model of particle dispersion in a turbulent plane mixing layer. *International Journal for Numerical Methods in Fluids, 40*(5), 639-653.

Oshinowo, L. M., & Bakker, A. (2001). CFD modeling of solids suspensions in stirred tanks. *Symposium on computational modeling of metals, minerals and materials,* 205-215.

Özcan-Taşkin, G., & Wei, H. (2003). The effect of impeller-to-tank diameter ratio on draw down of solids. *Chemical Engineering Science, 58*(10), 2011-2022.

Pakzad, L., Ein-Mozaffari, F., & Chan, P. (2008). Using electrical resistance tomography and computational fluid dynamics modeling to study the formation of cavern in the mixing of pseudoplastic fluids possessing yield stress. *Chemical Engineering Science, 63*(9), 2508-2522.

Parker, D. J., Leadbeater, T. W., Fan, X., Hausard, M. N., Ingram, A., & Yang, Z. (2008). Positron imaging techniques for process engineering: Recent developments at birmingham. *Measurement Science and Technology, 19*(9) 1-10.

Patankar, S. V. (1980). *Numerical heat transfer and fluid flow*. New York, NY: Hemisphere Publishing Co., Taylor & Francis Group.

Paul, E. L., Atiemo-Obeng, V. A., & Kresta, S. M. (2004). *Handbook of industrial mixing: Science and practice* Wiley-Interscience.

Peker, S. M. (2008). In Helvaci S. S., Yener H. B., Ikizler B. and Alparslan A. (Eds.), *Solid-liquid two phase flow* (1st edition). Oxford: Elsevier.

Perry, R. H., & Green, D. (1984). Chemical engineers handbook. *McGraw-Hill, New York,* , 5.63-5.68.

Pettersson, M., & Rasmuson, A. C. (1998). Hydrodynamics of suspensions agitated by pitched-blade turbine. *AIChE Journal, 44*(3), 513-527.

Pinheiro, P. A. T., Loh, W. W., Waterfall, R. C., Wang, M., & Mann, R. (1999). Three-dimensional electrical resistance tomography in a stirred mixing vessel. *Chemical Engineering Communications, 175*(1), 25-38.

Prakash, M., Cleary, P. W., Ha, J., Noui-Mehidi, M. N., Blackburn, H. M., & Brooks, G. (2007). Simulation of suspension of solids in a liquid in a mixing tank using SPH and comparison with physical modeling experiments. *Progress in Computational Fluid Dynamics, 7*(2-4), 91-100.

Prat, O. P., & Ducoste, J. J. (2007). Simulation of flocculation in stirred vessels - lagrangian versus eulerian. *Chemical Engineering Research & Design, 85*(A2), 207-219.

Ranade, V. V. (2002). *Computational flow modeling for chemical reactor engineering* Academic Press.

Ranade, V. V., Tayalia, Y., & Krishnan, H. (2002). CFD predictions of flow near impeller blades in baffled stirred vessels: Assessment of computational snapshot approach. *Chemical Engineering Communications, 189*(7), 895-922.

Reinecke, N., Petritsch, G., Schmitz, D., & Mewes, D. (1998). Tomographic measurement techniques – visualization of multiphase flows. *Chemical Engineering & Technology, 21*(1), 7-18.

Ricard, F., Brechtelsbauer, C., Xu, X. Y., & Lawrence, C. J. (2005). Monitoring of multiphase pharmaceutical processes using electrical resistance tomography. *Chemical Engineering Research & Design,Vol.83,no.A7,Pp.794-805,July 2005; 7th World Congress of Chemical Engineering, 10-14 July 2005, Glasgow, UK. , 83*(A7) 794-805.

Roberts, R. M., Gray, M. R., Thompson, B., & Kresta, S. M. (1995). The effect of impeller and tank geometry on circulation time distributions in stirred tanks. *Chemical Engineering Research & Design, 73*(A1), 78-86.

Saffman, P. G. (1965). The lift on a small sphere in a slow shear flow. *Journal of Fluid Mechanics, 22*, 385-400.

Scott, D.M., & Williams, R.A. (1995). *Frontiers in industrial process tomography*. New York, NY: Engineering Foundation.

Sessiecq, P., Mier, P., Gruy, F., & Cournil, M. (1999). Solid particles concentration profiles in an agitated vessel. *Chemical Engineering Research and Design, 77*(8), 741-746.

Sha, Z. L., Palosaari, S., Oinas, P., & Ogawa, K. (2001). CFD simulation of solid suspension in a stirred tank. *Journal of Chemical Engineering of Japan, 34*(5), 621-626.

Shamlou, P. A., & koutsakos, E. (1989). Solids suspension and distribution in liquids under turbulent agitation. *Chemical Engineering Science, 44*(3), 529-542.

Siddiqui, H. (1993). Mixing technology for buoyant solids in a nonstandard vessel. *AICHE Journal, 39*, 505-509.

Sommerfeld, M. (2001). Validation of a stochastic lagrangian modeling approach for inter-particle collisions in homogeneous isotropic turbulence. *International Journal of Multiphase Flow, 27*(10), 1829-1858.

Sommerfeld, M., & Decker, S. (2004). State of the art and future trends in CFD simulation of stirred vessel hydrodynamics. *Chemical Engineering and Technology, 27*(3), 215-224.

Špidla, M., Sinevič, V., Jahoda, M., & MacHoň, V. (2005). Solid particle distribution of moderately concentrated suspensions in a pilot plant stirred vessel. *Chemical Engineering Journal, 113*(1), 73-82.

Špidla, M., Sinevič, V., Jahoda, M., & MacHoň, (2005). Effect of baffle design on the off-bottom suspension characteristics of axial-flow impellers in a pilot-scale mixing vessel. *Chemical and Biochemical Engineering Quarterly, 19*(4), 333-340.

Stanley, S. J., Mann, R., & Primrose, K. (2002). Tomographic imaging of fluid mixing in 3-D for single-feed semi-batch operation of a stirred vessel. *Chemical Engineering Research and Design/Official Journal of the European Federation of Chemical Engineering: Part A, 80*(A8), 903-909.

Stanley, S. J. (2006). Tomographic imaging during reactive precipitation in a stirred vessel: Mixing with chemical reaction. *Chemical Engineering Science, 61*(24), 7850-7863.

Stanley, S. J., & Bolton, G. T. (2008). A review of recent electrical resistance tomography (ERT) applications for wet particulate processing. *Particle and Particle Systems Characterization, 25*(3), 207-215.

Stokes, J. A., Alvar, K. R., Corey, R. L., Costello, D. G., John, J., Kocimski, S., et al. (1982). Some new applications of collimated photon scattering for nondestructive examination. *Nuclear Instruments and Methods, 193*(1-2), 261-267.

Syamlal, M., & O'Brien, T. J. (1989). Computer simulation of bubbles in a fluidized bed. *AIChE Symposium Series, 85*(270) 22-31.

Takenaka, N., Fujii, T., Ono, A., Motomura, Y., & Toruno, A. (1994). Visualization and measurement of multi-phase and liquid metal flow by realtime neutron radiography. *Proc. German-Japanise Symp. on Multi- Phase Flow,Karlsruhe, Germany,* , 147-161.

Takenaka, K., Takahashi, K., Bujalski, W., Nienow, A. W., Paolini, S., Paglianti, A., et al. (2005). Mixing time for different diameters of impeller at a high solid concentration in an agitated vessel. *Journal of Chemical Engineering of Japan, 38*(5), 309-315.

Tapp, H., Peyton, A., Kemsley, E., & Wilson, R. (2003). Chemical engineering applications of electrical process tomography. *Sensors & Actuators: B.Chemical, 92*(1-2), 17-24.

Tatterson, G. B. (1991). *Fluid mixing and gas dispersion in agitated tanks* Mc Graw-Hill Inc., New York.

Tatterson, G. B. (1994). *Scale-up and design of industrial mixing processes* McGraw-Hill Inc., New York.

Tyagi, M., Roy, S., Harvey III, A. D., & Acharya, S. (2007). Simulation of laminar and turbulent impeller stirred tanks using immersed boundary method and large eddy simulation technique in multi-block curvilinear geometries. *Chemical Engineering Science, 62*(5), 1351-1363.

Uhl, V. W., & Gray, J. B. (1966). Mixing: Theory and practice. *Academic Press,* (New York)

Versteeg, H. K., & Malalasekera, W. (2007). *An introduction to computational fluid dynamics: The finite volume method* (Pearson Education Limited, Second Edition ed.) Prentice Hall.

Wang, M., Dorward, A., Vlaev, D., & Mann, R. (2000). Measurements of gas–liquid mixing in a stirred vessel using electrical resistance tomography (ERT). *Chemical Engineering Journal, 77*(1-2), 93-98.

Wang, F., Mao, Z. -., Wang, Y., & Yang, C. (2006). Measurement of phase holdups in liquid-liquid-solid three-phase stirred tanks and CFD simulation. *Chemical Engineering Science, 61*(22), 7535-7550.

Wang, M., Jones, T. F., & Williams, R. A. (2003). Visualization of asymmetric solids distribution in horizontal swirling flows using electrical resistance tomography. *Chemical Engineering Research & Design, 81*(A8), 854-861.

Wen, C. Y., & Yu, Y. H. (1966). Mechanics of fluidization. *Chem. Eng. Prog. Symp. Ser, , 62*(62) 100-111.

West, R. M., Jia, X., & Williams, R. A. (1999). Quantification of solid-liquid mixing using electrical resistance and positron emission tomography. *Chemical Engineering Communications, 175*, 71-97.

White, R. B., & Doblin, C. (2003). An investigation of sparged mixing tanks using electrical impedance tomography and computational fluid dynamics. *Third International Conference on CFD in the Minerals and Process Industries CSIRO,Melborne, Australia, December*, 10-12.

Williams, R. A., & Beck, M. S. (1995). *Process tomography: Principles, techniques and applications.* Butterworth-Heinemann.

Williams, R. A., Jia, X., West, R. M., & Roberts, K. J. (1998). On line measurement of solids distributors in stirred tanks and crystallizers using electrical computed tomography. *International Conference on Mixing and Crystallization. April,* 22-25.

Williams, R., Jia, X., & McKee, S. (1996). Development of slurry mixing models using resistance tomography. *Powder Technology, 87*(1), 21-27.

Wu, J., Zhu, Y., & Pullum, L. (2001). Impeller geometry effect on velocity and solids suspension. *Chemical Engineering Research and Design, 79*(8), 989-997.

Yamazaki, H., Tojo, K., & Miyanami, K. (1986). Concentration profiles of solids suspended in a stirred tank. *Powder Technology, 48*(3), 205-216.

Yamazaki, H., Tojo, K., & Miyanami, K. (1991). Effect of power consumption on solids concentration profiles in a slurry mixing tank. *Powder Technology, 64*(3), 199-206.

Zhang, X., & Ahmadi, G. (2005). Eulerian-lagrangian simulations of liquid-gas-solid flows in three-phase slurry reactors. *Chemical Engineering Science, 60*(18), 5089-5104.

Zhao, Z. F., Mehrvar, M., & Ein-Mozaffari, F. (2008). Mixing time in an agitated multi-lamp cylindrical photoreactor using electrical resistance tomography. *Journal of Chemical Technology & Biotechnology, 83*(12), 1676-1688.

Zwietering, T. N. (1958). Suspending of solid particles in liquid by agitators. *Chemical Engineering Science, 8*(3-4), 244-253.